Analytical and experimental studies of instability of an axial compression

Lu Zhang

To cite this version:

Lu Zhang. Analytical and experimental studies of instability of an axial compression. Other. Université de Lyon, 2016. English. NNT : 2016LYSEC046 . tel-02373142

HAL Id: tel-02373142
https://theses.hal.science/tel-02373142
Submitted on 20 Nov 2019

THÈSE de DOCTORAT DE L'UNIVERSITÉ DE LYON
opérée au sein de l'École centrale de Lyon

École Doctorale N°162
Mécanique, Énergétique, Génie Civil et Acoustique
Spécialité : Mécanique

Soutenance prévue le 29 novembre 2016, par

Lu ZHANG

Analytical and experimental studies of instability of an axial compression system

---

Devant le jury composé de

Pr. José Galindo	Universidad Politécnica de Valencia	-*Rapporteur*
Dr. Xavier Ottavy	LMFA	-*Examinateur*
Pr. Julian Scott	LMFA	-*Directeur de thèse*
Pr. Xiaofeng Sun	Beihang University	-*Rapporteur*
Pr. Isabelle Trébinjac	LMFA	-*Examinatrice*
Dr. Anna Young	University of Cambridge	-*Examinatrice*

Abstract

This thesis presents an analytical and experimental study of an axial compression system consisting of a compressor, plenum and throttle. The analysis is based on the Moore-Greitzer model, the results being later employed to interpret the experimental ones. Linear and weakly nonlinear analyses are presented, as are some results obtained by numerical integration of the fully nonlinear model equations. A simple theoretical model of the experimentally observed acoustic modes is also presented. In the experiments, pressure measurements were carried out for different rotation rates and throttle settings. This allowed the determination of the pressure rise across the compressor and the flow rate using a Venturi, yielding the compressor characteristic function. Pressure fluctuations were measured using four microphones placed upstream of the compressor. We did not observe surge, but rotating stall occurred when the system was sufficiently throttled. Prior to stall, fluctuations corresponding to acoustic duct modes were found. At stall onset, a rotating stall cell of growing amplitude was observed. However, the cell rapidly broke down and gave way to random fluctuations. Thus, for the given compression system, developed stall is perhaps better described as random, rather than rotating. Signal processing (frequency spectra, as well as auto- and cross-correlations) was used to analyse the pressure fluctuations of the acoustic modes and developed stall. The acoustic modes give spectral peaks located close to the expected theoretical values. In the presence of stall, the spectrum is broadband, having a low frequency ($\sim$20 Hz) peak followed by a tail which extends up to $\sim$1 kHz, well above the rotation frequency ($\sim$150 Hz) of the rotor. There appears to be a frequency range between the low-frequency peak and the high-frequency fall-off in which the spectrum approximates a power law. The auto-correlations and cross-correlations between different microphones show $\sim$20 Hz oscillations. Low pass filtering the data, the cross-correlation functions of the filtered signals of different microphones suggest a rotating cell which takes $\sim$0.05 s for a complete rotation. This could explain the $\sim$20 Hz spectral peak and oscillations of the correlation functions. Thus, the pressure fluctuations appear to consist of a strong high-frequency, random component and a rotating cell. Decorrelation of the filtered signal as separation time increases indicates that, rather than maintaining form and rotational velocity like a classical stall cell, the cell itself exhibits randomness.

Résumé

Cette thèse présente l'étude analytique et expérimentale d'un système de compression axial constitué d'un compresseur, d'un plénum et d'une vanne de régulation du débit. Fondée sur le modèle de Moore-Greitzer, une approche analytique est utilisée par la suite pour interpréter les données expérimentales. Les analyses linéaires et non linéaires sont présentées, ainsi que les résultats obtenus par intégration numérique des équations du modèle non linéaire complet. Un modèle théorique simple pour les modes acoustiques observés est aussi présenté. Dans les expériences, les mesures de pression ont été réalisées pour différents taux de rotation et différents vannages. Ceci a permis la détermination de l'augmentation de pression au travers du compresseur et du débit en utilisant un Venturi, ceux qui fournissent la courbe de fonctionnement du compresseur. Les fluctuations de pression sont mesurées par quatre microphones placés en amont du compresseur. Nous n'avons pas observé de pompage, mais un décrochage tournant s'est produit quand le système était suffisamment vanné. Avant ceci, des fluctuations correspondant aux modes acoustiques de la conduite ont été trouvées. Au début du décrochage, une cellule de décrochage tournante d'amplitude croissante a été observée. Cependant, la cellule a rapidement éclaté, remplacée par des fluctuations aléatoires. Ainsi, pour le système de compression considéré, la situation de décrochage est mieux décrite comme étant aléatoire plutôt que rotative.

Le traitement du signal (spectres en fréquence ainsi que les auto-corrélations et corrélations croisées) a permis d'analyser les fluctuations de pression des modes acoustiques et du décrochage développé. Les modes acoustiques montrent des pics spectraux proches des valeurs prédites par la théorie. En présence de décrochage, le spectre est à large bande, et contient un pic de fréquence basse ($\sim$20 Hz) suivi d'une queue s'étendant jusqu'à 1 kHz, bien au-dessus de la fréquence de rotation du rotor ($\sim$150 Hz). Il apparaît une gamme fréquentielle située entre le pic à basse fréquence et la chute à haute fréquence, dans laquelle le spectre évolue en loi de puissance. Les auto-corrélations et corrélations croisées entre les différents microphones montrent des oscillations à $\sim$20 Hz. En appliquant un filtre passe-bas aux données, les fonctions de corrélations croisées des signaux filtrés des différents microphones suggèrent l'existence d'une cellule rotative qui effectue une rotation complète en $\sim$0.05 s. Ceci pourrait expliquer le pic spectral à $\sim$20 Hz et les oscillations des fonctions

de corrélation. De ce fait, les fluctuations de pression apparaissent comme contenant une forte composante aléatoire à haute fréquence, et une cellule rotative. La décorrélation du signal filtré quand la séparation en temps augmente indique que la cellule elle-même a un caractère aléatoire, plutôt qu'une forme et une vitesse rotative fixes comme dans une cellule de décrochage classique.

Table of contents

List of figures

Chapter 1

Introduction

In this chapter, we briefly present the context and scope of the work, which consists of an analytical and experimental study of instability in a low-speed axial compressor. Section 1.1 describes the context, while section 1.2 summarises the work. The final section 1.3 gives the plan of this thesis.

1.1 Context

1.1.1 Compressor instabilities

Turbomachinery is used in many industrial applications, an important one being aircraft engines. The history of the jet engine goes back a long way and technological progress continues to this day. The core components of a jet engine are the compressor, combustion chamber and turbine. Gas turbines using the same principles are employed for energy production. Here we focus on the compressor, which is a source of instabilities in certain operating ranges. Such instabilities can significantly reduce performance and may even lead to structural damage. Since these instabilities occur in a parameter range where pressure rise and efficiency are near to optimal, they have considerable practical importance.

There are two main kinds of turbo-compressor: centrifugal and axial. Both types are subject to instabilities, which limits their operating range. Here, we will focus on axial compressors. There are two principal types of instability: surge and rotating stall. Surge is axisymmetric and results from interactions between the compressor and a chamber, known as the plenum and usually situated downstream of the compressor (the combustion chamber of a jet engine provides an example). In certain cases, the usual (and desired) steady flow becomes unstable and undergoes cyclic oscillations which are referred to as surge. During part of the surge cycle, the compressor supplies more air to the plenum than can escape downstream. Thus, the plenum pressure rises, making it harder for the compressor to drive the flow. At some point the compressor is no longer capable of maintaining a higher flow rate into than out of the plenum. This leads to the second part of the surge cycle, in which the plenum pressure falls. The compressor subsequently recovers and the plenum pressure rises again. The result is cyclic oscillations of the plenum pressure and flow rate. The flow rate may even become negative during part of the cycle, a condition known as deep surge. Note that surge involves the entire compression system: both compressor and plenum. Typically, surge has a period much less than the rotational period of the compressor. Surge was not observed in our experiment.

Rotating stall is non-axisymmetric and localised at the compressor. As its name implies, it arises from stalling of the blades over part of the compressor. The result is a reduction in the flow rate and pressure rise across the compressor, thus degrading performance. Classical rotating stall involves a stall cell which rotates with constant angular velocity, less than that of the rotor, but in the same sense. This leads to periodic fluctuations near the compressor, whose frequency is lower, but of the same order as the rotor rotation frequency. We say "classical", because, for the compression system used in our experiment, stall results in random, rather than periodic, fluctuations. Furthermore, these fluctuations have broadband spectra which extend to frequencies which are much higher than the rotor rotational frequency. As far as we know, this is the first time that random stall has been observed.

1.1.2 Some previous studies of compressor instabilities

Since the mid 1970s, research has focused on prediction and avoidance of instabilities (Paduano et al. [31], Day [8]). Analytical models have been developed, among these the Moore-Greitzer model (Moore and Greitzer [28]) is perhaps the best known. This model is capable of handling both surge and rotating stall. It is a "mass-spring" type model of a compression system consisting of a compressor, inlet and outlet ducts, a plenum and a throttle. The plenum acts as "spring", while the "mass" arises from fluid inertia in the ducts and compressor. The compressor is represented by a characteristic function, which expresses the difference between downstream static pressure and upstream total pressure as a function of flow rate, and a parameter a, which represents inertia. Modelling of the plenum introduces the Greitzer parameter, B, which is nondimensional and depends, among things, on the plenum volume. Everything else being fixed, the larger the plenum volume, the larger the value of B. A large value of B is found to encourage surge, whereas a small value promotes rotating stall. The model has been validated by experimental studies (Gysling and Greitzer [18], Schalkwyk et al. [34], D'Andrea et al. [6], Freeman et al. [11]). Active control strategies based on the model (Paduano et al. [29], Paduano et al. [30], Feulner et al. [10], Haynes et al. [19], Gravdahl and Egeland [16], Wang et al. [42]) have also been developed. Three-dimensional models were later proposed (Sun [38], Gong et al. [15]).

Experimental studies of compressor instabilities have suggested different scenarios for onset of rotating stall. Garnier et al. [13] observed a pre-stall wave travelling around the rotor face at a frequency similar to that of rotating stall (Chen et al. [2]). On the other hand, other authors (Camp and Day [1], Day [7]) have reported a "spike" precursor to stall onset. A definitive explanation of the mechanisms of stall inception remains elusive.

The increasing power of computers have opened the way to increasingly sophisticated numerical simulations of flow in compressors. The ideal would be to use direct numerical simulation (DNS) of the Navier-Stokes equations, but this is currently not feasible due to the extravagant computation times and memory requirements of such simulations. Practical calculations use turbulence models, such as RANS (Reynolds-averaged Navier-Stokes) or LES (Large eddy simulation). Such methods are only approximate and represent a compromise between accuracy and feasibility. They are used in industry to reduce the time scale and cost of designing turbomachinery, among other applications (such as aircraft wings). They have also been applied in more fundamental studies, including compressor instabilities (He [20], Hendricks et al. [21], Saxer-Felici et al. [33], Crevel et al. [4], Crevel et al. [5]). The unsteady flow around the compressor blades is simulated in detail (Inoue et al. [23],Gbadebo et al. [14], Choi et al. [3], Gao et al. [12]). The results allow the identification of instabilities. Spike precursors of stall have been a particular focus of interest (Hoying et al. [22],Vo [40], Vo et al. [41],Pullan et al. [32]). As noted above, the use of turbulence modelling means that the results are only approximations to reality and they often disagree with experiments. There can also be disagreements between different simulations of the same system. For instance, Yamada et al. [43], Pullan et al. [32] and Ju and Ning [25] simulated stall inception, but came to different conclusions. Until such a time as the simulations are more dependable, experiments will continue to play an important role.

1.1.3 Stability analysis

Instabilities are not confined to turbomachinery applications: they occur in most flows beyond a certain threshold boundary in flow-parameter space. The study of flow instabilities has a very long history and is a well-established branch of fluid mechanics (Drazin and Reid [9], Schmid and Henningson [35]). Consider a flow (known as the basic flow), which is theoretically possible because it satisfies the governing (Navier-Stokes) equations and boundary conditions. This flow is subjected to a small perturbation and the time evolution of the perturbation examined. If the perturbation grows, the basic flow is unstable, while decay means stability. Flows can be unstable to some perturbations and stable to others. A flow is deemed globally stable if it is stable to all perturbations, no matter how large. In that case, the flow is always approached at large times. Local stability refers to infinitesimal perturbations. A flow which is locally unstable cannot be realised in practice (there is always some level of perturbation). On the other hand, a locally stable flow is realised for sufficiently small perturbations. Note that, in the presence of unstable growth of the perturbation, the basic flow is not approached and is replaced by another one. This leads to changes in flow regime as the flow parameters are varied. For instance, a steady flow may be replaced by an unsteady one, a two-dimensional flow by a three-dimensional one, or a laminar flow by a turbulent one.

Various well-established techniques are available for studying flow stability. Amongst these, the earliest to be developed and by far the most commonly used deals with local stability. Thus, the perturbation is supposed infinitesimal. This allows terms of order higher than the first to be neglected in the evolution equations of the perturbation, a process known as linearization and whose result is linear theory. Linearization opens up an armoury of mathematical techniques, the most important of which is normal mode decomposition. Normal modes are particular solutions of the equations, from which the general solution can be obtained by superposition. The modes can be studied separately: if just one of them grows, the flow is deemed locally (or linearly) unstable. As noted above, this means it is unrealisable in practice. On varying the flow parameters, the flow may be stable in some parameter ranges and unstable in others. The boundary between stable and unstable regions of flow-parameter space is referred to as the instability threshold.

Another technique, known as weakly nonlinear theory, treats small, but finite, perturbations and flow-parameter values close to the instability threshold. It allows the distinction to be made between two types of instability: supercritical and subcritical. In the supercritical case, the basic flow is replaced by another nearby one when the instability threshold is crossed. The transition between the two stable flows occurs continuously at the threshold. On the other hand, a subcritical instability can occur in the parameter range predicted to be stable by linear theory. This requires that the perturbation amplitude exceed a certain value, which goes to zero as the linear instability threshold is approached. Thus, it becomes harder and harder to maintain stability near the threshold. When subcritical instability occurs, the theory predicts that the perturbation amplitude goes to infinity in a finite time. Of course, in reality, the perturbation remains finite: the flow leaves the regime of small perturbations supposed by the theory, which means that it no longer applies and is incapable of predicting the new flow resulting from the instability. However, it is clear that the result of subcritical instability is a flow quite different from the basic one. There is thus a jump in flow properties at the instability threshold. This jump, and the occurrence of instability in the linearly stable region of parameter space, is symptomatic of subcritical instability.

1.2 Scope of the work

As noted earlier, the work has an analytical modelling part and an experimental part.

In the former, we used the Moore-Greitzer model of compressor instabilities and obtained results which were later employed to interpret the experimental ones. Linear and weakly nonlinear theories were developed to elucidate the consequences of the model. A numerical scheme for integration of the model equations was also developed and used to obtain results in the fully nonlinear regime. Finally, a simple model of the experimentally observed acoustic modes was developed.

The experimental part of the study used a test rig consisting of a compressor (a Technofan LP3), a plenum and a throttle. Pressure measurements were carried out at various rotational speeds and throttle settings. A Venturi located in the duct between the compressor and the plenum allowed determination of the flow rate in the stable regime. This, together with pressure-difference measurements across the compressor, yielded the compressor characteristic function. Four microphones placed upstream of the compressor allowed measurement of the unsteady pressure fluctuations. As noted earlier, we did not observe surge, but random stall occurred when the system was throttled sufficiently. Prior to the appearance of stall, we found pressure fluctuations corresponding to acoustic duct modes. Different stages were observed during stall inception: acoustic modes, then stall onset, in which a rotating stall cell of growing amplitude is found. However, this cell rapidly breaks down and there are random fluctuations thereafter. Signal processing (spectra, as well as auto- and cross-correlations) was used to investigate the pressure fluctuations due to the acoustic modes and fully developed random stall.

1.3 Thesis outline

Chapter 2 concerns the analytical part of the study. We first describe and discuss the Moore-Greitzer model. Linear and weakly nonlinear analyses of the model are then presented. Some results of numerical integration of the model equations using a compressor characteristic function obtained by cubic fitting to the experimental one are given. Modelling of the acoustic modes is also described.

Chapters 3 and 4 concern the experiment and its results. Chapter 3 describes the test rig and sensors used, while chapter 4 gives results and describes their analysis and interpretation.

Chapter 2

Modelling of axial compression systems

This chapter concerns theoretical modelling. The Moore-Greitzer model and its consequences for instability are described in sections 2.1 and 2.2, while section 2.3 develops a simple model of the acoustic modes which were observed in our experiments.

2.1 The Moore-Greitzer model

In 1976, Greitzer [17] proposed a one-dimensional, theoretical model of unsteady flow in an axial compression system which is capable of reproducing many of the characteristics of surge. The model allows for an axial compressor, inlet and outlet ducts, a plenum and a throttle. It contains a parameter, B , whose value is found to be important in controlling the system dynamics. In particular, a large value tends to promote surge instability. The Greitzer model assumes the flow to be axisymmetric and thus cannot treat rotating stall, a case which was modelled by Moore [27]. The two models were combined in an article by Moore and Greitzer [28], yielding a more complete model which is capable of handling both surge and rotating stall. The combined model is the subject of this section. It should be noted that, although the full model allows for all Fourier components in the azimuthal angle, when performing calculations based on the model, Moore and Greitzer chose to truncate it to just one non-axisymmetric component. Here, we use the full model.

2.1.1 Description of the model

The axial compression system we have in mind is shown schematically in figure 2.1 and consists of four main components: the compressor, modelled as an actuator disk, the duct in which the compressor is situated, a plenum and a throttle which controls the flow rate. The part of the duct containing the compressor is supposed of constant inner and outer radii, R_1

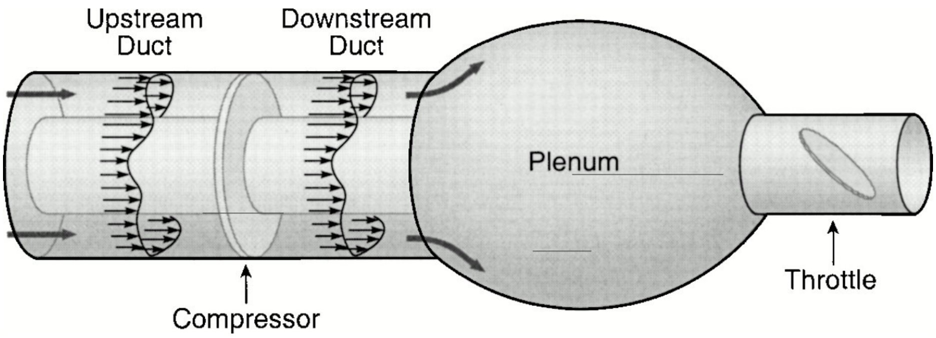

Fig. 2.1 Schematic of a compression system (from Paduano et al. [31]).

and R_2. In what follows, U denotes the rotor velocity at the mid-duct radius, $R = (R_1 + R_2)/2$. Pressure and time are nondimensionalised using ρU^2 and R/U, where ρ denotes the density of the fluid. Thus, the nondimensional time for a single rotation is 2π. The axial velocity at the compressor is nondimensionalised using U and expressed as a Fourier series in the azimuthal angle, θ (defined as increasing in the sense of rotation of the rotor):

$$u(\theta,t) = \Phi(t) + \sum_{n\neq 0} u^{(n)}(t)e^{in\theta}. \tag{2.1}$$

Thus, $\Phi(t)$ is the axisymmetric part of the velocity and represents the instantaneous volume flow rate, while the sum represents the non-axisymmetric part of the flow. Note that, in keeping with actuator-disk modelling, the angular variation, $u(\theta)$, is not intended to take into account individual compressor blades. Because u is a real quantity, the complex coefficients $u^{(n)}$ must satisfy $u^{(-n)} = u^{(n)^*}$, where the $*$ denotes complex conjugation. According to Moore and Greitzer [28], the non-axisymmetric part of the flow decays exponentially away from the compressor disk, with the nth Fourier component behaving like $\exp[-|n||x|]$, $|x|$ being axial distance from the disk, non-dimensionalised using R. Thus, the non-axisymmetric component is localised near the compressor, whereas the axisymmetric one pervades the entire compression system.

Also according to Moore and Greitzer [28], the non-dimensional difference between the static pressure at the exit of the compressor and the total pressure at its entrance is

$$\Psi_c(u) - \frac{1}{a}\left(\frac{\partial u}{\partial t} + \frac{1}{2}\frac{\partial u}{\partial \theta}\right). \tag{2.2}$$

Here, Ψ_c is known as the characteristic function of the compressor and, for steady, axisymmetric flow, $\Psi_c(\Phi)$ gives the pressure difference across the compressor. The second term in (2.2) models unsteadiness and non-axisymmetry and contains the parameter $a > 0$. The equations of the model are

$$l_c \frac{d\Psi}{dt} = \frac{1}{4B^2}(\Phi - \Phi_T(\Psi)), \tag{2.3}$$

$$l_c \frac{d\Phi}{dt} = \Psi_c^{(0)} - \Psi, \tag{2.4}$$

$$|n|^{-1}\left(2 + \frac{|n|}{a}\right)\frac{du^{(n)}}{dt} = \Psi_c^{(n)} - \frac{in}{2a}u^{(n)},\ n \neq 0, \tag{2.5}$$

$$\sum_{n=-\infty}^{\infty} \Psi_c^{(n)} e^{in\theta} = \Psi_c(u). \tag{2.6}$$

The first of these equations models the plenum. The difference between the plenum and atmospheric pressures is denoted by Ψ, which evolves if the flow rate, Φ, into the plenum differs from that, Φ_T, leaving the plenum. The throttle is modelled by $\Phi_T(\Psi)$, which gives the flow rate as a function of pressure difference. The Greitzer B-parameter is defined by

$$B = \frac{U}{2c}\sqrt{\frac{V_p}{A_c l_c R}} \tag{2.7}$$

where c is the sound speed in the plenum, V_p is its volume and $A_c = \pi(R_2^2 - R_1^2)$ is the cross-sectional area of the compressor. Equation (2.4) expresses the axisymmetric part of the dynamics of the flow in the duct and compressor. The term on the left represents mass multiplying acceleration, while the left-hand side corresponds to the force due to pressure differences. The parameter l_c represents fluid inertia in the duct and compressor. Equation (2.5) plays a similar role for the non-axisymmetric part of the flow. Given Φ and $u^{(n)}$, $u(\theta)$ can be calculated using (2.1), hence the left-hand side of (2.6) is determined and Fourier transformed to give the $\Psi_c^{(n)}$, which appear in (2.4) and (2.5). Thus, if the functions Ψ_c and Φ_T, together with the parameters a, l_c and B, are given, the system of equations is closed and can be integrated to follow the time evolution of the compressor system, starting from specified initial conditions.

Note that, if the flow is initially axisymmetric ($u^{(n)} = 0$), it remains so. Equation (2.5) is then unnecessary, (2.1) and (2.6) imply $\Psi_c^{(0)} = \Psi_c(\Phi)$, hence (2.3) and (2.4) become

$$l_c \frac{d\Psi}{dt} = \frac{1}{4B^2}(\Phi - \Phi_T(\Psi)), \tag{2.8}$$

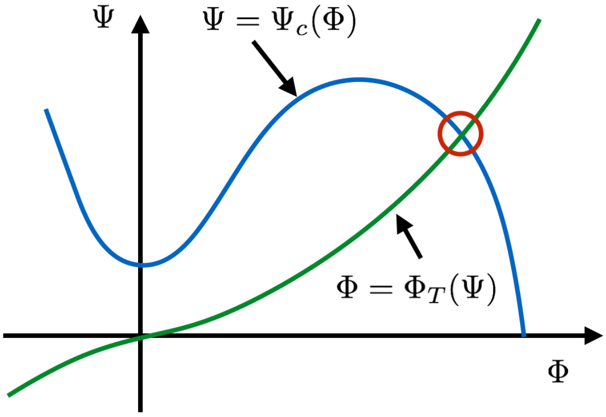

Fig. 2.2 Compressor and throttle characteristics in the Φ-Ψ plane. The axisymmetric steady flow lies at their intersection.

$$l_c \frac{d\Phi}{dt} = \Psi_c(\Phi) - \Psi \tag{2.9}$$

as governing equations for axisymmetric flow. This is the Greitzer model of surge. However, a small non-axisymmetric perturbation may grow, a phenomenon known as rotating stall. This is one of two types of generally recognised turbomachinery instability, the other being surge, which is axisymmetric. Note that changing the parameter l_c in (2.8) and (2.9) merely alters the time scale for evolution. However, changing B has a more profound effect. It is generally found that large B tends to encourage surge, whereas small B is usually associated with rotating stall.

If the flow is both axisymmetric and steady, equations (2.8) and (2.9) lead to

$$\Phi = \Phi_T(\Psi), \Psi = \Psi_c(\Phi). \tag{2.10}$$

These equations are graphically represented in figure 2.2. The curves represent the throttle and compressor characteristics, while their intersection gives the axisymmetric, steady flow. This is usually the desired operating point of the system. However, it may be unstable in the sense that small perturbations grow. In that case, the given flow is not realized and the result can be surge or rotating stall. Note the form of the compressor characteristic, which possesses a minimum and a maximum. Between the two extrema, $\Psi_c(\Phi)$ is increasing. Operating points in this range tend to be unstable, whereas those on the descending branch, above the maximum of the compressor characteristics, tend to be stable. This makes it difficult to determine $\Psi_c(\Phi)$ in the increasing range, either experimentally or using a more sophisticated numerical model (e.g. unsteady RANS or LES). However, Zhang et al. [44] proposed a method, based on (2.2) and results of numerical simulation for a single surge cycle, for obtaining $\Psi_c(\Phi)$ in this range. Numerical simulations which impose steadiness are another possibility.

The usual throttle model is based on a head loss proportional to the square of the flow rate:

$$\Phi = \Theta \operatorname{sgn}(\Psi)|\Psi|^{1/2} \tag{2.11}$$

where Θ is a parameter representing the throttle setting and sgn is the sign function ($\operatorname{sgn}(\Psi) = 1$ if $\Psi > 0$, $\operatorname{sgn}(\Psi) = -1$ if $\Psi < 0$). As the flow is throttled, Θ decreases and the operating point in figure 2.2 moves up the compressor characteristic. When it approaches or crosses the maximum of $\Psi_c(\Phi)$, instability is likely. Moore and Greitzer [28] propose a cubic compressor characteristic model:

$$\Psi_c(\Phi) = \Psi_{c0} + H\left[1 + \frac{3}{2}\left(\frac{\Phi}{W} - 1\right) - \frac{1}{2}\left(\frac{\Phi}{W} - 1\right)^3\right]. \tag{2.12}$$

As noted above, large B favours surge. Examining the large-B limit of (2.8) and (2.9) allows understanding of the surge cycle. Because B is large, equation (2.8) implies that Ψ is slowly varying. Initialising with arbitrary Φ and Ψ, equation (2.9) leads to comparatively rapid evolution of Φ towards the characteristic curve, $\Psi_c(\Phi) = \Psi$. That is, the point representing the system in the Φ-Ψ plane of figure 2.2 moves towards the right or left along a nearly horizontal line. It moves to the right if the initial point lies below the compressor characteristic curve and to the left otherwise. Thus, the point moves towards one of the decreasing branches of the compressor characteristic curve. As it approaches that curve, the right-hand side of (2.9) decreases and the point slows down until Ψ and Φ are evolving on the same (slow) time scale. The point then moves slowly along the characteristic curve until one of two conditions are met: a) it reaches the operating point and settles down to become the steady flow, or b) it reaches either the minimum or the maximum of the curve. In the latter case, the point can no longer follow the curve and must move nearly horizontally (and relatively rapidly) to the other decreasing branch of the curve, along which it continues its slow evolution. If the operating point lies on a decreasing branch (as in figure 2.1), it is the final destination of the flow, meaning that the steady flow is stable. On the other hand, an operating point on the increasing part of the curve is never reached and surge occurs. This is the large-B instability condition for axisymmetric flow. The large-B surge cycle is illustrated by figure 2.3.

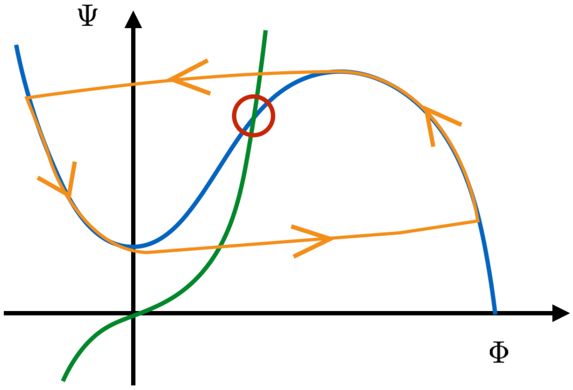

Fig. 2.3 Large-B surge cycle.

2.1.2 Linear stability analysis

Here we examine the stability of steady, axisymmetric flow to infinitesimal perturbations. Thus, the basic flow is $\Psi = \Psi_0$, $\Phi = \Phi_0$, $u^{(n)} = 0$, where Ψ_0 and Φ_0 are a solution of (2.10). This flow is perturbed and we ask the question: does the perturbation grow or not? We write

$$\psi = \psi_0 + \widetilde{\Psi}, \ \Phi = \Phi_0 + \widetilde{\Phi}, \tag{2.13}$$

where $\widetilde{\Psi}$, $\widetilde{\Phi}$ and $u^{(n)}$ represent the perturbation and are infinitesimal. Equation (2.1) gives

$$u(\theta) = \Phi_0 + \widetilde{\Phi} + \sum_{n \neq 0} u^{(n)} e^{in\theta} \tag{2.14}$$

for the perturbed flow. Taylor's expansion of $\Psi_c(u)$ about $u = \Phi_0$ gives

$$\Psi_c(u) = \Psi_0 + \Psi_c' \left(\widetilde{\Phi} + \sum_{n \neq 0} u^{(n)} e^{in\theta} \right), \tag{2.15}$$

where Ψ_c' is the derivative of $\Psi_c(u)$ at $u = \Phi_0$ and second-order and higher terms in the expansion are neglected because the perturbation is infinitesimal. This approximation is referred to as linearization and is commonly used in stability theory. Using (2.15), (2.6) implies

$$\Psi_c^{(0)} = \Psi_0 + \Psi_c' \widetilde{\Phi}, \ \Psi_c^{(n)} = \Psi_c' u^{(n)} \ n \neq 0. \tag{2.16}$$

Employing Taylor's expansion of $\Phi_T(\Psi)$ about $\Psi = \Psi_0$, $\Phi_T(\Psi) = \Phi_0 + \Phi_T' \widetilde{\Psi}$, where Φ_T' is the derivative at $\Phi = \Phi_0$ (note that $\Phi_T' > 0$ because $\Phi_T(\Psi)$ is an increasing function) and, as before, higher-order terms have been neglected. Equations (2.3) and (2.4) yield

$$l_c \frac{d\widetilde{\Psi}}{dt} = \frac{1}{4B^2}(\widetilde{\Phi} - \Phi'_T \widetilde{\Psi}), \tag{2.17}$$

$$l_c \frac{d\widetilde{\Phi}}{dt} = \Psi'_c \widetilde{\Phi} - \widetilde{\Psi} \tag{2.18}$$

for the axisymmetric part of the perturbation, while (2.5) gives

$$|n|^{-1}\left(2 + \frac{|n|}{a}\right)\frac{du^{(n)}}{dt} = \left(\Psi'_c - \frac{in}{2a}\right)u^{(n)} \tag{2.19}$$

for the non-axisymmetric part. Note that the axisymmetric and non-axisymmetric parts are decoupled and can be studied separately. Furthermore, different ns are also decoupled. This is as usual in linear stability analysis of axisymmetric basic flows: the perturbation can be expressed as a sum over decoupled normal modes, each consisting of a single Fourier component in θ.

Let us first consider the axisymmetric modes. Equations (2.17) and (2.18) are linear equations with constant coefficients. Thus, there are exponential solutions of the form $\exp[st]$, where s is a complex number. This is as usual in linear stability analysis of steady basic flows. Writing $\widetilde{\Psi} = \widehat{\Psi}\exp[st]$, $\widetilde{\Phi} = \widehat{\Phi}\exp[st]$, equations (2.17) and (2.18) give

$$(4B^2 l_c s + \Phi'_T)\widehat{\Psi} - \widehat{\Phi} = 0, \tag{2.20}$$

$$\widehat{\Psi} + (l_c s - \Psi'_c)\widehat{\Phi} = 0. \tag{2.21}$$

This is a linear system of equations for $\widehat{\Psi}$ and $\widehat{\Phi}$. The determinantal condition for a nonzero solution is

$$4B^2 l_c^2 s^2 + (\Phi'_T - 4B^2\Psi'_c)l_c s + 1 - \Phi'_T \Psi'_c = 0, \tag{2.22}$$

which is a quadratic equation for s. The two roots of this equation correspond to two axisymmetric modes, the general solution of (2.17), (2.18) being a linear combination of two exponentials. Writing $s = s_r + is_i$, each mode has time dependence

$$\exp[st] = \exp[s_r t]\exp[is_i t] = \exp[s_r t](\cos[s_i t] + i\sin[s_i t]). \tag{2.23}$$

The real exponential leads to either growth or decay of the mode, depending upon the sign of s_r, whereas the sinusoidal term represents oscillations of frequency s_i. If one or other of the roots of equation (2.22) lies in $s_r > 0$, the corresponding mode is growing and the flow is unstable. Thus, linear stability comes down to determining the sign of s_r for the two roots of (2.22).

If $\Phi_T'\Psi_c' > 1$, (2.22) has two real roots of opposite signs. Thus, the flow is unstable for all B. The case $\Phi_T'\Psi_c' < 1$ is treated as follows. In the limit $B \to 0$, the roots of (2.22) are asymptotically described by

$$s \sim -\frac{\Phi_T'}{4l_cB^2}, \; s \sim \frac{\Phi_T'\Psi_c' - 1}{l_c\Phi_T'}. \tag{2.24}$$

Since $\Phi_T' > 0$ and $\Phi_T'\Psi_c' < 1$, both roots are negative. The roots lie to the left of the imaginary axis in the complex s-plane at small B and the flow is stable. As B increases, a root may cross the imaginary axis, leading to instability. At the point of crossing, $s = is_i$, and the real and imaginary parts of (2.22) give

$$s_i^2 = \frac{1 - \Phi_T'\Psi_c'}{4B^2l_c^2}, \; (\Phi_T' - 4B^2\Psi_c')s_i = 0. \tag{2.25}$$

Because $\Phi_T'\Psi_c' \neq 0$, the first of these equations implies that $s_i \neq 0$, so the second yields

$$\Phi_T' - 4B^2\Psi_c' = 0. \tag{2.26}$$

If $\Psi_c' < 0$, both terms on the left-hand side are positive. Thus, when the operating point lies on the decreasing part of the compressor characteristic (and $\Phi_T'\Psi_c' < 1$) root crossing cannot occur and the flow is stable for all B. On the other hand, if $\Psi_c' > 0$, both roots cross the imaginary axis when

$$B = \left(\frac{\Phi_T'}{4\Psi_c'}\right)^{1/2}. \tag{2.27}$$

The flow is stable below this value and unstable at higher B. This illustrates the tendency to axisymmetric instability at large B.

One can summarise the different cases by the condition

$$\Psi_c' > \min\left(\frac{1}{\Phi_T'}, \frac{\Phi_T'}{4B^2}\right) \tag{2.28}$$

for axisymmetric instability according to linear theory. This condition implies that instability can only occur if $\Psi_c' > 0$, i.e. the operating point lies on the increasing part of the compressor characteristic. Provided $\Psi_c' > 0$, (2.28) is always satisfied as $B \to \infty$, thus the flow is unstable to axisymmetric perturbations at large enough B. As B is decreased, axisymmetric stability sets in below the threshold give by (2.27) if $\Phi'_T \Psi'_c < 1$, otherwise instability persist down to $B = 0$. Note that $\Phi'_c \to 0$ as the operating point approaches the maximum of Ψ_c. Thus, close to the maximum, the flow is stable to axisymmetric perturbations according to 2.28.

Analysis of the non-axisymmetric modes is simpler. The solution of (2.19) has the form , where

$$s = |n| \frac{a\Psi'_c - in/2}{|n| + 2a}. \tag{2.29}$$

Since $a > 0$, the sign of s_r is determined by that of Ψ'_c. Thus, if the operating point lies on the increasing part of the compressor characteristic, the flow is unstable to non-axisymmetric perturbations of all n, otherwise it is stable according to linear theory. A non-axisymmetric mode has the form

$$\exp[s_r t] \exp[i(n\theta - \omega^{(n)} t)], \tag{2.30}$$

where

$$\omega^{(n)} = \frac{n|n|}{2(|n| + 2a)} \tag{2.31}$$

is the modal frequency. As discussed earlier, the real exponential in (2.30) describes growth or decay of the mode. The second one can be interpreted as a disturbance which rotates with angular velocity $|n|/2(|n| + 2a)$. Thus, according to linear analysis of the model, different n rotate in the same sense as the rotor at different rates: high-order modes rotate at one half the rotor velocity and lower-order ones more slowly.

Finally, we note that instability occurs if any one of the modes, axisymmetric or non-axisymmetric grows. For operating points outside of the increasing part of the compressor characteristic, the flow is stable to both types of perturbation, whereas instability of non-axisymmetric modes always occurs for $\Psi'_c > 0$. This is the linear instability condition allowing for all modes. The threshold for instability occurs when the operating point lies at the maximum of the compressor characteristic. Note that this threshold is determined by the non-axisymmetric modes, but is also approached by the axisymmetric ones at large B.

2.1.3 Weakly nonlinear theory

The problem with linear theory is that it predicts unbounded exponential growth of the perturbation in the unstable regime. This inevitably means that, after a certain time, the assumption of an infinitesimal perturbation breaks down and linear theory no longer holds. Nonlinearity can, of course, be allowed for by numerical integration of the model equations and results of such calculations are described later in this section. However, an analytical approach is possible close to a linear instability threshold and assuming a small perturbation. This is the subject of this subsection and is referred to as weakly nonlinear theory.

Linear theory predicts stability in some parameter ranges and instability in others, the boundary in parameter space being referred to as the instability threshold. All modes are damped ($s_r < 0$) on the stable side of the threshold, but as it is crossed, one or more of the modal s_r passes through zero and the associated modes (known as critical modes) are growing on the unstable side of the threshold. In our case, all non-axisymmetric modes have the same threshold and are critical. This is a more complicated situation than that treated in classical weakly nonlinear analysis, which assumes a single critical mode. This is the reason for revisiting the analysis with the Moore-Greitzer model in mind.

To explain the basis of weakly nonlinear theory, we suppose a single critical mode. While this is not the case for the Moore-Greitzer model, it is simpler to first consider the classical case. Assuming a small perturbation, nonlinearity is weak and linear theory applies to a first approximation. Weak nonlinearity means that it takes a long time, t_{nl}, to act. In order that it can nonetheless have an effect, the growth or decay predicted by linear theory should be slow, i.e. s_r must be small (of order t_{nl}^{-1}). This occurs close to the instability threshold. Thus, the assumptions of weakly nonlinear theory are that: a) the perturbation is small, b) the parameter values of the system are near to linear instability threshold.

As noted above, assumption (a) means that linear theory gives a first approximation. At the instability threshold, modes other than the critical one are decaying. Given assumption (b), such modes decay on a time scale much shorter than the one, t_{nl}, which interest us here. Thus, following a transient phase, only the critical mode remains. Linear theory does not determine the amplitude, A, of the critical mode (any solution of the linearised equations can be multiplied by an arbitrary constant and remain a solution). Weak nonlinearity and the small departure from the instability threshold influence the evolution of A over times of order t_{nl}. This is expressed by a nonlinear evolution equation, known as the amplitude equation, for $A(t)$. The objective of weakly nonlinear analysis is to obtain this amplitude equation.

Based on physical reasoning, Landau [26] (c.f. Drazin and Reid [9]) proposed the equation

$$\frac{d|A|}{dt} = \sigma|A| - \ell|A|^3, \tag{2.32}$$

in which σ is the value of s_r for the critical mode and measures departure from the instability threshold, while ℓ is known as the Landau constant. The two terms on the right-hand side represent linear and nonlinear effects. In the absence of the nonlinear term, the expected exponential behaviour is recovered. Stuart [37] derived (2.32) using mathematical reasoning.

Figure 2.4 illustrates the consequences of the Landau equation. As indicated by the annotation, the horizontal axis represents σ, which, as noted above, is a parameter expressing departure from the instability threshold, $\sigma = 0$. $\sigma < 0$ (the left-hand side of the figures) corresponds to linear stability, while $\sigma > 0$ gives linear instability. Figure 2.4a concerns the

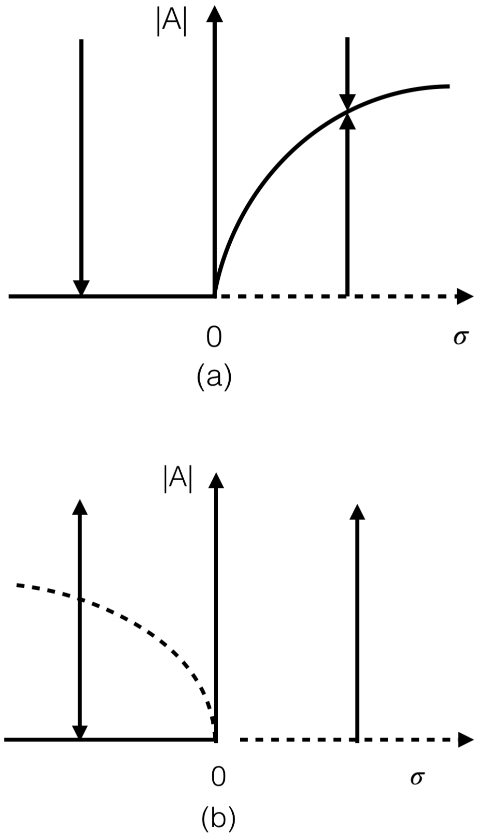

Fig. 2.4 Illustrations of a) supercritical and b) subcritical instability.

case $\ell > 0$, referred to as supercritical, whereas figure 2.4b is for the subcritical case, $\ell < 0$. "Equilibria" are obtained by setting the right-hand side of (2.32) to zero. One such is $|A| = 0$, which represents the basic flow (zero perturbation). Another follows from $|A|^2 = \sigma/\ell$, giving the parabolae of the figures. The latter equilibrium requires positive σ/ℓ, hence the appearance of the parabola to the right in figure 2.4a and to the left in figure 2.4b. The solid lines refer to stable equilibria, the dashed lines to unstable ones. Thus, the basic flow gives a solid line in $\sigma < 0$ and a dashed one in $\sigma > 0$, while the parabola in figure 2.4a is stable, while it is unstable in figure 2.4b. The arrows represent time evolution according to equation (2.32).

Let us first consider the supercritical case shown in figure 2.4a. Here, the basic flow is stable for $\sigma < 0$ and the equilibrium represented by the parabola gives a new stable flow. The arrows indicate evolution towards whichever flow is stable. Thus, crossing the instability threshold replaces one stable flow by another. This happens in a continuous fashion: the amplitude of the critical mode starts at $|A| = 0$ when $\sigma = 0$ and then increases with σ. $\ell > 0$ means that nonlinearity is stabilising, i.e. the nonlinear term in (2.32) always tries to reduce the perturbation. When $\sigma < 0$, linear and nonlinear terms act in concert, so $|A|$ decreases monotonically to zero, as indicated by the arrow. If $\sigma > 0$, linear and nonlinear terms act in opposite directions, leading to the equilibrium represented by the parabola.

The subcritical case shown in figure 2.4b is quite different. The dashed parabola means that the corresponding equilibrium is unstable, and hence unrealisable. As indicated by the arrows, the parabola represents a threshold perturbation amplitude, below which the basic flow is approached. However, above the parabola in $\sigma < 0$, and everywhere in $\sigma > 0$, an equilibrium is never attained and the perturbation continues to grow. In fact, it reaches $|A| = \infty$ in finite time according to weakly nonlinear theory. This means that it rapidly goes beyond the scope of that theory, the perturbation attaining finite amplitude and the nonlinearity becoming strong. Although the theory breaks down, it does indicate that, when subcritical instability occurs, the result will be a flow quite different from the basic one. Note that, unlike the supercritical case, instability can occur in the range $\sigma < 0$, where linear theory predicts stability. This is the reason for the description "subcritical".

The remainder of this subsection develops weakly nonlinear theory for the Moore-Greitzer model using asymptotic analysis and discusses its consequences. The perturbation is expanded in powers of a small parameter, ε, and the method of multiple scales used to cope with the disparate time scales of the problem. The amplitude equations arise as a non-secularity condition at $O(\varepsilon^3)$.

The model is given by equations (2.1) and (2.3)-(2.6). We make the dependence of on the throttle-setting parameter, Θ, explicit by writing $\Phi_T = \Phi_T(\Psi,\Theta)$. The instability threshold is denoted Θ_0, the actual throttle setting being close to Θ_0 in order to comply with requirement (b) of weakly nonlinear theory. Let Ψ_0, Φ_0 and Θ_0 be a solution of

$$\begin{aligned} \Psi_c'(\Phi_0) &= 0, \\ \Psi_0 &= \Psi_c(\Phi_0), \\ \Phi_T(\Psi_0,\Theta_0) &= \Phi_0, \end{aligned} \tag{2.33}$$

in which the first equality determines Φ_0 (an extremum of $\Psi_c(\Phi)$: we have in mind the maximum, corresponding to the linear instability threshold), the second Ψ_0 and the third Θ_0. The last two equalities mean that Ψ_0, Φ_0 give a steady, axisymmetric solution for the particular throttle setting Θ_0. The non-axisymmetric modes of this flow have $u^{(n)} \propto e^{-i\omega^{(n)}t}$ according to the linear theory, where $\omega^{(n)}$, given by (2.31), is the frequency of mode n. It is convenient to remove the modal oscillation by writing $A^{(n)}(t) = u^{(n)}(t)e^{i\omega^{(n)}t}$, thus (2.1) and (2.5) become

$$|n|^{-1}\left(2+\frac{|n|}{a}\right)\frac{dA^{(n)}}{dt} = e^{i\omega^{(n)}t}\Psi_c^{(n)}, \tag{2.34}$$

$$u(\theta,t) = \Phi(t) + \sum_{n\neq 0} A^{(n)}(t)e^{i(n\theta-\omega^{(n)}t)}, \tag{2.35}$$

where $A^{(-n)} = A^{(n)*}$ follows from $u^{(-n)} = u^{(n)*}$ and $\omega^{(-n)} = -\omega^{(n)}$.

We want to investigate the weakly nonlinear stability of the basic flow, Ψ_0, Φ_0. To this end, we adopt the asymptotic expansions

$$\Psi = \Psi_0 + \varepsilon\Psi_1 + \varepsilon^2\Psi_2 + \ldots, \tag{2.36}$$

$$\Phi = \Phi_0 + \varepsilon\Phi_1 + \varepsilon^2\Phi_2 + \ldots, \tag{2.37}$$

$$A^{(n)} = \varepsilon A_1^{(n)} + \varepsilon^2 A_2^{(n)} + \varepsilon^3 A_3^{(n)} + \ldots, \tag{2.38}$$

$$\Theta = \Theta_0 + \sigma\varepsilon^2, \tag{2.39}$$

where ε is a small parameter. The expansions (2.36)-(2.38) show that the perturbation amplitude is $O(\varepsilon)$, while (2.39) indicates an $O(\varepsilon^2)$ departure from the instability threshold. We also adopt the method of multiple scales: apart from Ψ_0, Φ_0, which are constants, the coefficients in (2.36)-(2.38) depend on the fast time, t, and the slow time, $T = \varepsilon^2 t$. Thus,

$$\frac{d}{dt} = \frac{\partial}{\partial t} + \varepsilon^2\frac{\partial}{\partial T}, \tag{2.40}$$

gives the total time derivative in terms of fast- and slow-time partial derivatives.

Using (2.37) and (2.38), (2.35) gives

$$u = \Phi_0 + \varepsilon\left(\Phi_1 + \sum_{n\neq 1} A_1^{(n)}e^{i(n\theta-\omega^{(n)}t)}\right) + \ldots. \tag{2.41}$$

Hence, since $\Psi_c(\Phi_0) = \Psi_0$ and $\Psi_c'(\Phi_0) = 0$, (2.6) and Taylor's expansion of Ψ_c imply

$$\sum_{n=-\infty}^{\infty} \Psi_c^{(n)}e^{in\theta} = \Psi_0 + \frac{1}{2}\varepsilon^2\Psi_c''\left(\Phi_1 + \sum_{n\neq 0} A_1^{(n)}e^{i(n\theta-\omega^{(n)}t)}\right)^2 + \ldots, \tag{2.42}$$

where Ψ_c'' is the second derivative of $\Psi_c(\Phi)$ at Φ_0. It follows, using $A_1^{(-n)} = A_1^{(n)*}$ and $\omega^{(-n)} = -\omega^{(n)}$, that

$$\Psi_c^{(0)} = \Psi_0 + \frac{1}{2}\varepsilon^2\Psi_c''\left(\Phi_1^2 + \sum_{n\neq 0}|A_1^{(n)}|^2\right) + \ldots \tag{2.43}$$

and

$$\Psi_c^{(0)} = O(\varepsilon^2),\ n \neq 0. \tag{2.44}$$

Using (2.36)-(2.40), (2.43), (2.44) and the final equality in (2.33), (2.3), (2.4) and (2.34) give

$$l_c\frac{\partial\Psi_1}{\partial t} = \frac{1}{4B^2}(\Phi_1 - \Phi_{T,\Psi}\Psi_1), \tag{2.45}$$

$$l_c\frac{\partial\Phi_1}{\partial t} = -\Psi_1, \tag{2.46}$$

$$\frac{\partial A_1^{(0)}}{\partial t} = 0 \tag{2.47}$$

at $O(\varepsilon)$, where

$$\Phi_{T,\Psi} = \frac{\partial\Phi_T}{\partial\Psi}(\Psi_0,\Theta_0). \tag{2.48}$$

(2.47) implies that $A_1^{(n)} = A_1^{(n)}(T)$ depends only on the slow time. (2.45) and (2.46) lead to exponential decay of Ψ_1 and Φ_1 as functions of the fast time. That is, Ψ_1 and Φ_1 drop to 0 over a time span of $O(1)$. Since we are interest in what happens after this transient phase, we take $\Psi_1 = \Phi_1 = 0$ in what follows. Thus the axisymmetric component of the flow does not contribute to the perturbation at leading order.

Using (2.36), (2.37), (2.39), (2.40), (2.43) and the final equality in (2.33), (2.3) and (2.4) give

$$l_c\frac{\partial\Psi_2}{\partial t} = \frac{1}{4B^2}(\Phi_2 - \Phi_{T,\Psi}\Psi_2 - \sigma\Phi_{T,\Theta}), \tag{2.49}$$

$$l_c\frac{\partial\Phi_2}{\partial t} = \frac{1}{2}\Psi_c''\sum_{n\neq 0}|A_1^{(n)}|^2 - \Psi_2 \tag{2.50}$$

at $O(\varepsilon^2)$, where

$$\Phi_{T,\Theta} = \frac{\partial\Phi_T}{\partial\Theta}(\Psi_0,\Theta_0). \tag{2.51}$$

(2.49), (2.50) yield fast-time exponential decay towards

$$\Psi_2(T) = \frac{1}{2}\Psi_c'' \sum_{n\neq 0} |A_1^{(n)}|^2, \tag{2.52}$$

$$\Phi_2(T) = \sigma\Phi_{T,\Theta} + \frac{1}{2}\Phi_{T,\Psi}\Psi_c'' \sum_{n\neq 0} |A_1^{(n)}|^2. \tag{2.53}$$

Again, because we are interested in time following the initial transient, we use (2.52) and (2.53) in what follows. These equations show that the axisymmetric part of the flow responds passively to the presence of the non-axisymmetric part, as well as to the throttle setting. Observe that, according to (2.52) and $\Psi_1 = 0$, departures of Ψ from Ψ_0 are purely nonlinear effect.

(2.42) and $\Phi_1 = 0$ give

$$\Psi_c^{(n)} = \frac{1}{2}\varepsilon^2\Psi_c'' \sum_{\substack{n_1,n_2\neq 0\\ n_1+n_2=n}} A_1^{(n_1)}A_1^{(n_2)} \exp[-i(\omega^{(n_1)}+\omega^{(n_2)})t] + \ldots \; n \neq 0, \tag{2.54}$$

where, as indicated by the notation, the sum is over all nonzero n_1 and n_2 such that $n_1+n_2 = n$. Using (2.38), (2.40) and (2.54), (2.34) yields

$$|n|^{-1}\left(2+\frac{|n|}{a}\right)\frac{\partial A_2{}^{(n)}}{\partial t} = \frac{1}{2}\Psi_c'' \sum_{\substack{n_1,n_2\neq 0\\ n_1+n_2=n}} A_1^{(n_1)}A_1^{(n_2)} \exp[i(\omega^{(n)}-\omega^{(n_1)}-\omega^{(n_2)})t] \tag{2.55}$$

at $O(\varepsilon)$. According to (2.55), secular growth of $A_2^{(n)}$ would occur if one of the terms on the right-hand side had zero fast-time frequency, i.e. $\omega^{(n)}-\omega^{(n_1)}-\omega^{(n_2)} = 0$. However, it can be shown that this never happens. The solution of (2.55) is thus

$$A_2^{(n)} = B_2^{(n)}(T) - \frac{1}{2}i\Psi_c''|n|\left(2+\frac{|n|}{a}\right)^{-1} \sum_{\substack{n_1,n_2\neq 0\\ n_1+n_2=n}} \frac{A_1^{(n_1)}A_1^{(n_2)}\exp[i(\omega^{(n)}-\omega^{(n_1)}-\omega^{(n_2)})t]}{\omega^{(n)}-\omega^{(n_1)}-\omega^{(n_2)}}. \tag{2.56}$$

Taking (2.41) to the next order,

$$u = \Phi_0 + \varepsilon\sum_{n\neq 0} A_1^{(n)} e^{i(n\theta-\omega^{(n)}t)} + \varepsilon^2\left(\Phi_2 + \sum_{n\neq 0} A_2^{(n)} e^{i(n\theta-\omega^{(n)}t)}\right) + \ldots, \tag{2.57}$$

hence

$$\sum_{n=-\infty}^{\infty} \Psi_c^{(n)} e^{in\theta} = \Psi_0 + \frac{1}{2}\varepsilon^2 \Psi_c'' \left(\sum_{n\neq 0} A_1^{(n)} e^{i(n\theta - \omega^{(n)} t)} \right)^2 +$$
$$\varepsilon^3 \left(\Psi_c'' \left(\sum_{n\neq 0} A_1^{(n)} e^{i(n\theta - \omega^{(n)} t)} \right) \left(\Phi_2 + \sum_{n\neq 0} A_2^{(n)} e^{i(n\theta - \omega^{(n)} t)} \right) + \frac{1}{6}\Psi_c''' \left(\sum_{n\neq 0} A_1^{(n)} e^{i(n\theta - \omega^{(n)} t)} \right)^3 \right) + \ldots, \tag{2.58}$$

where Ψ_c''' is the third derivative of $\Psi_c(\Phi)$ at Φ_0. It follows that

$$\begin{aligned} \Psi_c^{(n)} &= \frac{1}{2}\varepsilon^2 \Psi_c'' \sum_{\substack{n_1,n_2\neq 0 \\ n_1+n_2=n}} A_1^{(n_1)} A_1^{(n_2)} \exp[-i(\omega^{(n_1)} + \omega^{(n_2)})t] + \\ &\varepsilon^3 \Bigg(\Psi_c'' \Phi_2 A_1^{(n)} e^{-i\omega^{(n)} t} + \Psi_c'' \sum_{\substack{n_1,n_2\neq 0 \\ n_1+n_2=n}} A_1^{(n_1)} A_1^{(n_2)} \exp[-i(\omega^{(n_1)} + \omega^{(n_2)})t] + \\ &\frac{1}{6}\Psi_c''' \sum_{\substack{n_1,n_2,n_3\neq 0 \\ n_1+n_2+n_3=n}} A_1^{(n_1)} A_1^{(n_2)} A_1^{(n_3)} \exp[-i(\omega^{(n_1)} + \omega^{(n_2)} + \omega^{(n_3)})t] \Bigg) + \ldots . \end{aligned} \tag{2.59}$$

Using (2.38), (2.40) and (2.59), (2.34) gives

$$\begin{aligned} &|n|^{-1} \left(2 + \frac{|n|}{a} \right) \frac{\partial A_3^{(n)}}{\partial t} = -|n|^{-1} \left(2 + \frac{|n|}{a} \right) \frac{dA_1^{(n)}}{dT} + \Psi_c'' \Phi_2 A_1^{(n)} + \\ &\Psi_c'' \sum_{\substack{n_1,n_2\neq 0 \\ n_1+n_2=n}} A_1^{(n_1)} A_1^{(n_2)} \exp[i(\omega^{(n)} - \omega^{(n_1)} - \omega^{(n_2)})t] + \\ &\frac{1}{6}\Psi_c''' \sum_{\substack{n_1,n_2,n_3\neq 0 \\ n_1+n_2+n_3=n}} A_1^{(n_1)} A_1^{(n_2)} A_1^{(n_3)} \exp[i(\omega^{(n)} - \omega^{(n_1)} - \omega^{(n_2)} - \omega^{(n_3)})t] \end{aligned} \tag{2.60}$$

at $O(\varepsilon^3)$. Employing (2.56),

$$\begin{aligned} &\sum_{\substack{n_1,n_2\neq 0 \\ n_1+n_2=n}} A_1^{(n_1)} A_1^{(n_2)} \exp[i(\omega^{(n)} - \omega^{(n_1)} - \omega^{(n_2)})t] \\ &= \sum_{\substack{n_1,n_2\neq 0 \\ n_1+n_2=n}} A_1^{(n_1)} B_2^{(n_2)} \exp[i(\omega^{(n)} - \omega^{(n_1)} - \omega^{(n_2)})t] - \\ &\frac{1}{2} i \Psi_c'' \sum_{\substack{n_1,n_2,n_3\neq 0 \\ n_1+n_2+n_3=n \\ n_1\neq n}} \frac{|n-n_1| A_1^{(n_1)} A_1^{(n_2)} A_1^{(n_3)}}{\left(2 + \frac{|n-n_1|}{a} \right) (\omega^{(n-n_1)} - \omega^{(n_2)} - \omega^{(n_3)})} \exp[i(\omega^{(n)} - \omega^{(n_1)} - \omega^{(n_2)} - \omega^{(n_3)})t]. \end{aligned} \tag{2.61}$$

We now want to identify secular forcing terms on the right-hand side of (2.60). These terms are those with zero fast-time frequency. Two are immediately apparent:

$$-|n|^{-1}\left(2+\frac{|n|}{a}\right)\frac{dA_1^{(n)}}{dT}+\Psi_c''\Phi_2 A_1^{(n)}. \tag{2.62}$$

Others arise from the final sum in (2.60) when one of the conditions: a) $n_1 = n$ and $n_2 = -n_3$, b) $n_2 = n$ and $n_1 = -n_3$, or c) $n_3 = n$ and $n_1 = -n_2$ is met. Being careful not to count a secular term more than once, we find

$$\frac{1}{2}\Psi_c'''\left(|A_1^{(n)}|^2+\sum_{\substack{n_1\neq 0\\ |n_1|\neq|n|}}|A_1^{(n_1)}|^2\right)A_1^{(n)} \tag{2.63}$$

for the secular forcing coming from the final sum in (2.60). Secular forcing also arises from the final sum in (2.61) when one of the conditions (b) or (c) is met. This gives the secular forcing contribution

$$-i\Psi_c''^2\left(\frac{|n||A_1^{(n)}|^2}{2\left(1+\frac{|n|}{a}\right)\left(\omega^{(2n)}-2\omega^{(n)}\right)}+\sum_{\substack{n_1\neq 0\\ |n_1|\neq|n|}}\frac{|n-n_1||A_1^{(n_1)}|^2}{\left(2+\frac{|n-n_1|}{a}\right)\left(\omega^{(n-n_1)}+\omega^{(n_1)}-\omega^{(n)}\right)}\right)A_1^{(n)}. \tag{2.64}$$

The non-secularity condition is that the sum of (2.62), (2.63) and (2.64) be zero. Thus

$$\begin{aligned}|n|^{-1}\left(2+\frac{|n|}{a}\right)\frac{dA_1^{(n)}}{dT}&=\Psi_c''\Phi_2A_1^{(n)}+\frac{1}{2}\Psi_c'''\left(|A_1^{(n)}|^2+\sum_{\substack{n_1\neq 0\\ |n_1|\neq|n|}}|A_1^{(n_1)}|^2\right)A_1^{(n)}-\\ i\Psi_c''^2&\left(\frac{|n||A_1^{(n)}|^2}{2\left(1+\frac{|n|}{a}\right)\left(\omega^{(2n)}-2\omega^{(n)}\right)}+\sum_{\substack{n_1\neq 0\\ |n_1|\neq|n|}}\frac{|n-n_1||A_1^{(n_1)}|^2}{\left(2+\frac{|n-n_1|}{a}\right)\left(\omega^{(n-n_1)}+\omega^{(n_1)}-\omega^{(n)}\right)}\right)A_1^{(n)}.\end{aligned} \tag{2.65}$$

(2.53) and (2.65) provide evolution equations for the amplitudes $A_1^{(n)}$. These are the final result of the asymptotic analysis, but we now want to simplify the notation by defining $\alpha_n = \varepsilon(\Phi_{T,\Psi}\Psi_c''^2/2)^{1/2}A_1^{(n)}$ and returning to original time variable t. Thus, we obtain

$$|n|^{-1}\left(2+\frac{|n|}{a}\right)\frac{d\alpha_n}{dt}=(\delta+\Delta_n)\alpha_n, \tag{2.66}$$

where

$$\begin{aligned}\Delta_n = \sum_{n_1\neq 0} |\alpha_{n_1}|^2 + \beta \left(|\alpha_n|^2 + \sum_{\substack{n_1\neq 0\\ |n_1|\neq|n|}} |\alpha_{n_1}|^2 \right) - \\ \frac{2i}{\Phi_{T,\Psi}} \left(\frac{|n||\alpha_n|^2}{2\left(1+\frac{|n|}{a}\right)\left(\omega^{(2n)}-2\omega^{(n)}\right)} + \sum_{\substack{n_1\neq 0\\ |n_1|\neq|n|}} \frac{|n-n_1||\alpha_{n_1}|^2}{\left(2+\frac{|n-n_1|}{a}\right)\left(\omega^{(n-n_1)}+\omega^{(n_1)}-\omega^{(n)}\right)} \right),\end{aligned} \tag{2.67}$$

$$\delta = \Phi_{T,\Theta}\Psi_c''(\Theta-\Theta_0) \tag{2.68}$$

and

$$\beta = \frac{\Psi_c'''}{\Phi_{T,\Psi}\Psi_c''^2}. \tag{2.69}$$

In (2.66), the coefficient δ, defined by (2.68), represents a linear effect due to the departure from neutral throttling, $\Theta = \Theta_0$, whereas Δ_n expresses the effects of weak nonlinearity. Linear theory is obtained by neglecting the nonlinear term. It follows that the linear instability condition is $\delta > 0$.

Writing $\alpha_n = |\alpha_n|e^{-i\zeta_n}$ and $\Delta_n = \Delta_n^r + i\Delta_n^i$, (2.66) yields

$$|n|^{-1}\left(2+\frac{|n|}{a}\right)\frac{d|\alpha_n|}{dt} = (\delta+\Delta_n^r)|\alpha_n|, \tag{2.70}$$

$$\frac{d\zeta_n}{dt} = -|n|\left(2+\frac{|n|}{a}\right)^{-1}\Delta_n^i. \tag{2.71}$$

(2.70) and (2.71) describe the time evolution of the amplitude and phase of Fourier mode n. The right-hand side of (2.71) represents a (small) nonlinear correction to the frequency, $\omega^{(n)}$, of the mode. More importantly, since we are interested in instability (i.e. possible growth of the perturbation), (2.67) gives

$$\Delta_n^r = \sum_{n_1\neq 0} |\alpha_{n_1}|^2 + \beta \left(|\alpha_n|^2 + \sum_{\substack{n_1\neq 0\\ |n_1|\neq|n|}} |\alpha_{n_1}|^2 \right). \tag{2.72}$$

Equations (2.70) and (2.72) describe the growth or decay of the perturbation and hence the weakly nonlinear stability of the flow (according to the Moore-Greitzer model). Thus, we have no need for (2.71) in what follows. (2.70) and (2.72) depend only on β, δ and a, which are thus the parameters controlling the weakly nonlinear stability of the compression system.

To treat the case $\beta > -2$, observe that (2.66) with (2.67) has particular solutions in which only one pair, $\pm n$, of conjugate Fourier components is present (all others having 0 amplitude). In that case, (2.70) takes the form of a Landau equation

$$|n|^{-1}\left(2+\frac{|n|}{a}\right)\frac{d|\alpha_n|}{dt} = (\delta + (\beta+2)|\alpha_n|^2)|\alpha_n|, \tag{2.73}$$

whose consequences for instability are well known. Since $\beta > -2$, the nonlinear term is positive, i.e. it tries to produce growth of $|\alpha_n|$. If $\delta > 0$ (linear instability), both linear and nonlinear terms are positive and the perturbation grows. On the other hand, if $\delta < 0$, it only does so if the initial modal amplitude exceeds $|\alpha_n| > (-\delta/(\beta+2))^{\frac{1}{2}}$. Thus, the model exhibits subcritical instability when $\beta > -2$: initial conditions leading to unstable growth can be found, even in the regime of linear stability, provided the perturbation amplitude is sufficient to provoke the instability. The threshold amplitude goes to 0 as the linear-stability boundary, $\Theta = \Theta_0$, is approached, as is usual for subcritical instability.

When $\beta < -2$, we write (2.72) as

$$\Delta_n^r = (2+\beta)|\alpha_n|^2 + (1+\beta)\sum_{\substack{n_1\neq 0\\ |n_1|\neq|n|}}|\alpha_{n_1}|^2, \tag{2.74}$$

in which both terms are negative, so nonlinearity is stabilizing. When $\delta < 0$, linear and nonlinear terms act together to render the basic flow stable to all perturbations. When $\delta > 0$, the basic flow is linearly unstable and thus unrealizable, but stabilization by nonlinearity limits the perturbation amplitude (if it becomes too large, nonlinearity pulls it back down). These characteristics imply supercritical instability, in which the basic flow is unconditionally stable in the regime predicted by linear theory and unstable thereafter. The basic flow is replaced by a new one when it is linearly unstable. The transition between the two flows as the linear stability boundary is crossed is continuous: the perturbation amplitude starts at zero when $\delta = 0$ and increase with δ. Thanks to the oscillations of the non-axisymmetric modes, the new flow will be unsteady and non-axisymmetric.

Thus we conclude that the Moore and Greitzer model predicts a subcritical instability if $\beta > -2$ and a supercritical one if $\beta < -2$. Unlike most hydrodynamic stability problems, in which there is a single critical mode, here each n has the same stability threshold, $\Theta = \Theta_0$, which makes it difficult to predict the precise consequence of instability, even in the supercritical case. In the subcritical case, we expect the usual unbounded growth of the perturbation, thus taking the flow beyond the weakly nonlinear regime supposed here. As always, this means that the it is impossible to predict the end result of subcritical instability without resorting to numerical simulation. However, the new flow will quite different from the basic one.

Adopting the usual throttle model

$$\Phi_T = \Theta \,\mathrm{sgn}\,(\Psi)|\Psi|^{1/2}, \tag{2.75}$$

(2.69) gives

$$\beta = \frac{2\Psi_0 \Psi_c'''}{\Phi_0 \Psi_c''^2}, \tag{2.76}$$

whose value depends on the compressor characteristic function, $\Psi_c(\Phi)$, in particular its maximum value, Ψ_0, and that of its second and third derivatives at the maximum, which is attained for $\Phi = \Phi_0$. In the case of the cubic characteristic function, (2.12), we obtain

$$\Phi_0 = 2W, \Psi_0 = \Psi_{c0} + 2H, \Psi_c'' = -\frac{3H}{W^2}, \Psi_c''' = -\frac{3H}{W^3}, \tag{2.77}$$

and hence

$$\beta = -\frac{\Psi_{c0} + 2H}{3H}. \tag{2.78}$$

Thus, the instability is subcritical if $\Psi_{c0} < 4H$ and supercritical if $\Psi_{c0} > 4H$. Another way of putting this is that, for the cubic characteristic function, a ratio of maximum Ψ_c to minimum Ψ_c greater than 3/2 leads to subcritical instability. It is clear from these results that the nature, subcritical or supercritical, of the instability may vary from one compressor to another.

Finally, the above analysis does not include surge instability, since the axisymmetric component of the flow is slaved to the non-axisymmetric one by (2.52) and (2.53) and, in any case, does not contribute to the perturbation at leading order since $\Psi_1 = \Phi_1 = 0$. Giving the axisymmetric component sufficient scope to express its dynamics, and hence include instability, would no doubt require a large value of B, suggesting a possible direction for the future work. The present work suggests that moderate B favors non-axisymmetric instability (rotating stall), at least for small perturbation amplitudes.

2.2 Numerical results of the model

Equations (2.1) and (2.3)-(2.6) are integrated numerically using a fourth-order Runge-Kutta scheme to step forward in time from given initial conditions. The infinite sums in (2.1) and (2.6) are truncated to finite ones, i.e. they are limited to the range $|n| \leq N$. The azimuthal angle, θ, is correspondingly discretised to the values $\theta_m = m\pi/N (0 \leq m < 2N)$. Given Φ and $u^{(n)}(|n| \leq N)$, (2.1) is used to compute $u(\theta_m)$ and $\Psi_c(u)$ determined at θ_m using the prescribed compressor characteristic function. Solving (2.6) for $\Psi_c^{(n)}$, the right-hand sides of (2.4) and (2.5) are known and the numerical integration can proceed. Fast Fourier transforms were used to implement (2.1) and the solution of (2.6). The numerical parameters, namely N and the time step, were varied to check for convergence. Thus, N was increased and the time step decreased until the required precision (we chose a precision of eight decimal places) was attained. In the end, we settled on the value $N = 32$ and a non-dimensional time step of 0.1 as sufficient.

As noted earlier, the model requires specification of the compressor and throttle characteristic functions, Ψ_c and Φ_T. We used (2.11) and (2.12) to obtain the results described here. Rather than directly specifying the throttle parameter, Θ, in (2.11), we chose to define a "nominal" operating point as follows. Given a nominal flow rate Φ_0, we define $\Psi_0 = \Psi_c(\Phi_0)$ and calculate Θ using (2.11). Thus, Φ_0, rather than Θ, is used to describe the throttle position. $\Psi = \Psi_0$, $\Phi = \Phi_0$ represent a steady, axisymmetric solution of the model equations, but it may be unstable, hence the description "nominal".

2.2.1 Parameterization

The cubic compressor characteristic model, (2.12), contains the parameters W, H and Ψ_{c0}. These were obtained by fitting to the measurements. Figure 2.5 shows experimental points and the fitted characteristic (which has $W = H = 0.165$ and $\Psi_{c0} = 0.3$). Note that the experimental point with smallest Φ corresponds to a case for which rotating stall occurs and should thus be ignored. This illustrates the difficulty, noted earlier, of using experimental data to determine Ψ_c: only the stable part of the characteristic is available. The fitting shown in the figure was done by eye, rather than using some more mathematical approach, such as least squares. We believe the result is among the best possible using a model of the form (2.12). Other forms of the characteristic function can, of course, be envisaged and may lead to better fits, but, given the lack of data in the unstable range, one is spoilt for choice.

The model also requires values of the parameters a, l_c and B. Of these, a, which appears via (2.2), is notoriously hard to determine and we, rather arbitrarily, choose a value of 0.5. l_c is defined in [28] in terms of a and the lengths of the compressor inlet and outlet ducts. Using the geometry of the test rig gives $l_c = 65$. Table 2.1 summarises the parameters used. Using the plenum volume of the experiment gives $B \approx 0.4$. However, we prefer to leave the value of B a variable parameter, Thus, the value of B and the nominal flow rate, Φ_0, are varied to study their effects on stability.

Having fixed most of the parameters of the model, it is perhaps interesting to apply the linear and weakly nonlinear stability results of the previous section. Given the compressor and throttle characteristic functions assumed here, $\Phi_T' \Psi_c' < 1$ applies throughout the range,

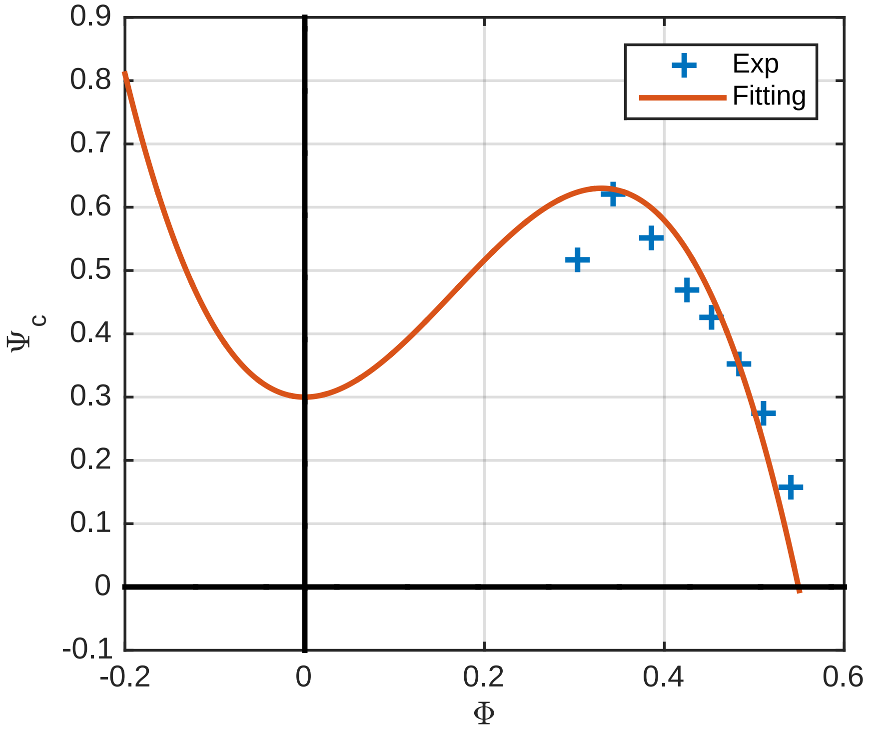

Fig. 2.5 Fitting of the compressor characteristic function, $\Psi_c(\Phi)$, and measured points.

l_c	a	W	H	Ψ_{c0}
65	0.5	0.165	0.165	0.3

Table 2.1 Model parameters.

$\Phi_0 < 2W = 0.33$, in which $\Psi_c(\Phi_0)$ is increasing. Thus, axisymmetric instability is predicted by linear theory above a critical value of B given by equation (2.27) and plotted in figure 2.6. B is fixed for a given compression system, while throttling the system causes the nominal flow rate, Φ_0, to decrease: the point representing the system in the figure moves leftwards along a horizontal line and axisymmetric instability occurs when the curve is crossed. The minimum critical value of B occurs at $\Phi_0 = 0$ and is $(W^2/24H\Psi_{c0})^{1/2} = 0.15$. Below this value, axisymmetric instability does not occur according to linear theory. The dashed line in figure 2.6 is the non-axisymmetric, linear instability threshold. Since $\Psi_{c0} < 4H$, non-axisymmetric instability is subcritical, i.e. it can occur to the right of the dashed line due to nonlinearity. Note that, as B is increased, the critical curve for axisymmetric instability approaches the dashed line.

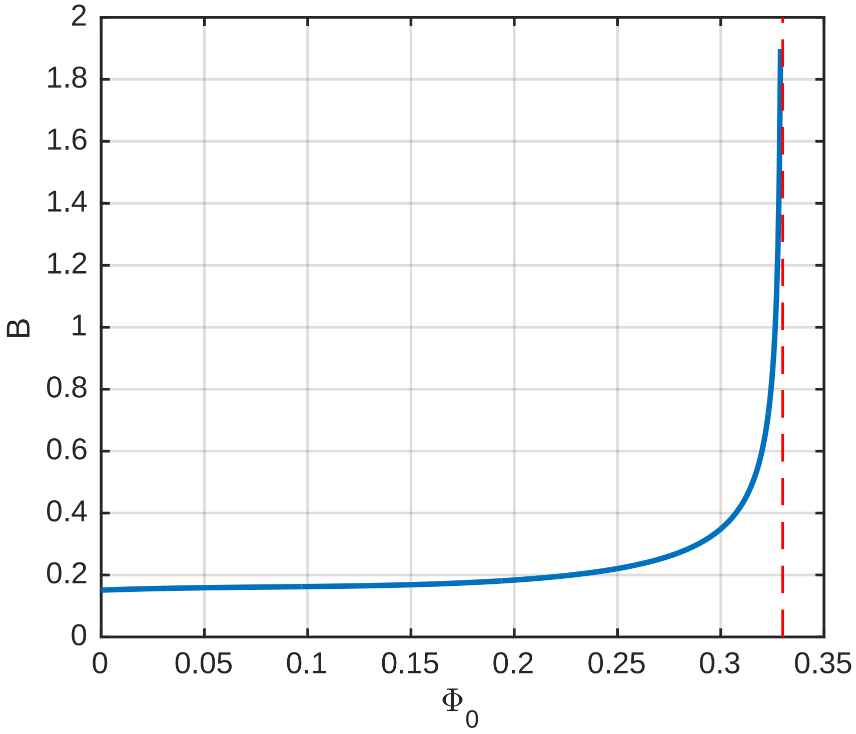

Fig. 2.6 Critical value of B as a function of Φ.

2.2.2 Illustrative results

Figures 2.7 and 2.8 show numerical results at large ($B = 3$) and moderate ($B = 0.3$) values of B for the throttle setting $\Phi_0 = 0.25$. Both cases lie above the critical curve in figure 2.6 and hence are unstable to axisymmetric perturbations. The calculations were initialised using a small axisymmetric perturbation of the nominal steady flow, $\Phi_0 = 0.25$, $\Psi_0 = 0.5812$. Figure 2.7 shows that, for $B = 3$, the system enters directly into a deep surge cycle, which is as indicated by figure 2.3 (see the discussion in the final paragraph of section 2.1.1). By deep surge, we mean that the flow rate, Φ, is negative over part of the cycle. Figure 2.8 shows a milder form of surge. Oscillations grow and reach a periodic limit cycle. Figure 2.9 shows results for $B = 0.2$, $\Phi = 0.25$, which lies below the critical curve in figure 2.6. The flow approaches the nominal steady state via damped oscillations, as predicted by linear theory. Many other calculations were carried out using axisymmetric initial conditions. The results showed stability below the critical curve and unstable growth of surge oscillations above the curve, in agreement with linear theory. This suggests that axisymmetric instability is supercritical.

Things are more complicated if the initial perturbation is non-axisymmetric. Figures 2.10 and 2.11 show results for $\Phi_0 = 0.25$ and the same two values of B as figures 2.8 and 2.9. The difference is that the initial perturbation is to the $n = \pm 1$ Fourier components, rather than the axisymmetric part of the flow (the initial conditions are $\Phi = \Phi_0$, $\Psi = \Psi_0$, $u^{(n)} = 0$ for $n \neq \pm 1$ and a small, nonzero value of $u^{(\pm 1)}$). Rather than surge, the end result is rotating stall. This can be seen in figures 2.10a, 2.10b, 2.11a and 2.11b: Φ and Ψ approach constant values which differ from Φ_0, Ψ_0. In figures 2.10c and 2.11c, it is apparent that the limit point in the Φ-Ψ plane lies below the compressor characteristic curve, representing a loss in performance due to stall. Figures 2.10d and 2.11d show the axial velocity, $u(\theta)$, at the compressor at time $t = 1500$, for which rotating stall is fully developed. The stall cell is apparent and is found to rotate in the same direction as the rotor. These results indicate that a given compressor system may show different types of instability, depending on the perturbations to which it is subjected. Whether the initial perturbation is axisymmetric or non-axisymmetric (or a combination of both) we never found surge below the critical curve of figure 2.6 or to the right of the dashed line. Note that, despite the different values of B in figures 2.10 and 2.11, the flows are essentially the same at large times (only the orientation of the stall cell differs). This because Ψ approaches a constant value, so (2.8) becomes $\Phi = \Phi_T(\Psi)$ and is now independent of B.

Figure 2.12 illustrates the subcritical nature of the rotating-stall instability. A large number of calculations were performed using $B = 0.35$ and the same non-axisymmetric initial perturbation as for figures 2.10 and 2.11. Different values of Φ_0 and initial $u^{(1)}$ were used, corresponding to a rectangular lattice of points in the $\Phi_0 - u^{(1)}$ plane of the figure. For each point, the calculation was carried out to large time and the presence or absence of rotating stall noted. The curve shows the instability boundary. The boundary meets the horizontal axis at the linear stability threshold. The flow is linearly stable to the right of the threshold, and linearly unstable to the left. We see that the instability is subcritical, i.e. it can occur in the range of Φ_0 deemed stable by linear theory if the initial perturbation exceeds a certain amplitude, represented by the curve. This is as predicted by weakly nonlinear theory (see figure 2.4, but bear in mind that the stable zone lies to the left in that figure, whereas it is to the right in figure 2.12). Figure 2.12b is a zoom of 2.12a.

2.3 Acoustic-mode modelling

This section develops a simple, one-dimensional model of the acoustic duct modes which were observed in our experiment. Figure 2.13 shows the geometry we have in mind. Linear

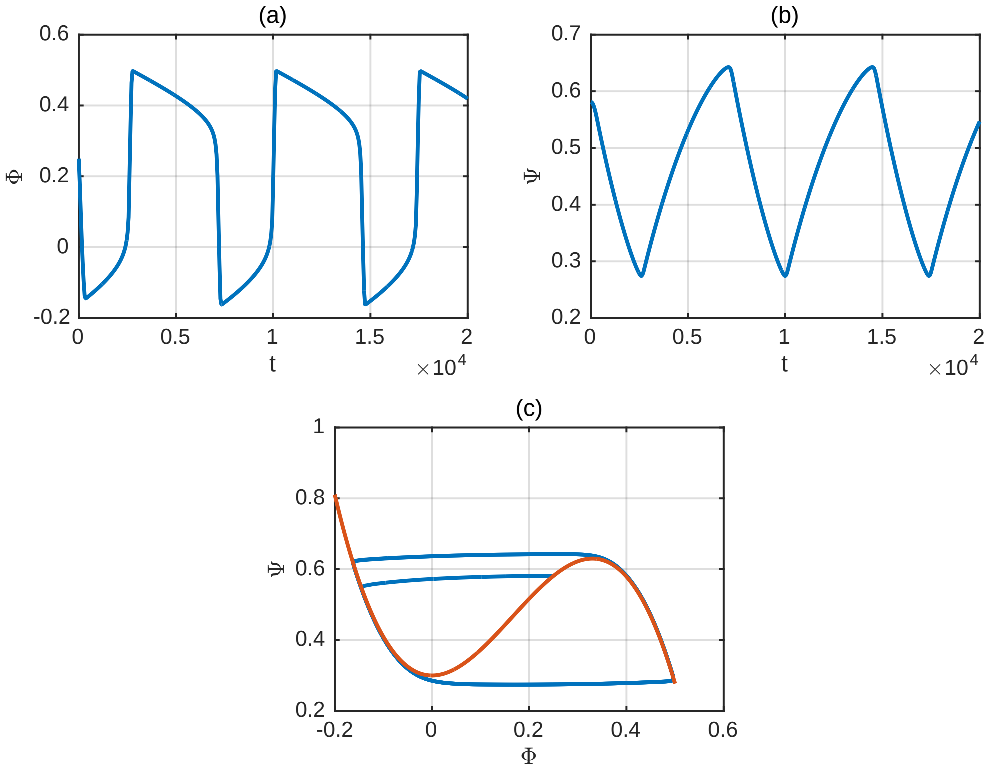

Fig. 2.7 Axisymmetric numerical results for $\Phi_0 = 0.25$ and $B = 3$. Here, and in subsequent figures, the $\Phi - \Psi$ plot also shows the compressor characteristic, $\Psi = \Psi_c(\Phi)$

acoustics is used to model acoustic propagation, which is assumed unaffected by flow in the duct. Thus, we require a small acoustic perturbation and small flow Mach number.

The Moore-Greitzer relation, (2.2), for the pressure difference across the compressor is used to express the pressure at the compressor exit:

$$p = p_{atm} + \rho U^2 \left(\Psi_c \left(\frac{u}{U} \right) - \frac{R}{aU^2} \frac{\partial u}{\partial t} \right) \tag{2.79}$$

where p_{atm} is atmospheric pressure and, here and henceforth, $p(x,t)$ and $u(x,t)$ are dimensional quantities representing pressure and velocity in the duct (the quantities Ψ_c and a are non-dimensional and have the same meanings as before). Axial distance, x, and time, t, are also dimensional. (2.79) forms a boundary condition for acoustic propagation along the duct.

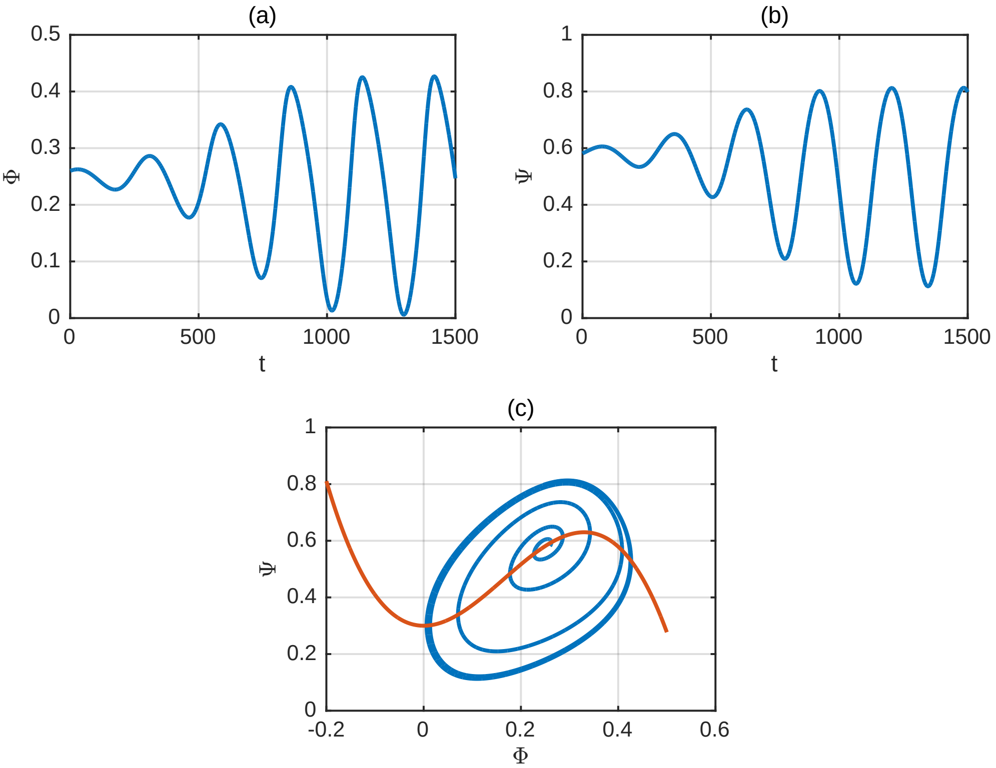

Fig. 2.8 Axisymmetric numerical results for $\Phi_0 = 0.25$ and $B = 0.3$.

The flow variables in the duct, $0 < x < L$ are written as

$$\begin{aligned} u &= u_0 + u', \\ p &= p_0 + p', \\ \rho &= \rho_0 + \rho', \end{aligned} \tag{2.80}$$

Where u_0 , p_0 and ρ_0 are constants representing the steady flow in the absence of acoustic waves, while u', p' and ρ' denotes the acoustic perturbations. Assuming the perturbation to be small, the one-dimensional Euler equations can be linearized, giving the usual acoustic relations:

$$\begin{aligned} &\rho_0 \frac{\partial u'}{\partial t} = -\frac{\partial p'}{\partial x}, \\ &\frac{\partial \rho'}{\partial t} = -\rho_0 \frac{\partial u'}{\partial x}, \\ &p' = c_0^2 \rho', \end{aligned} \tag{2.81}$$

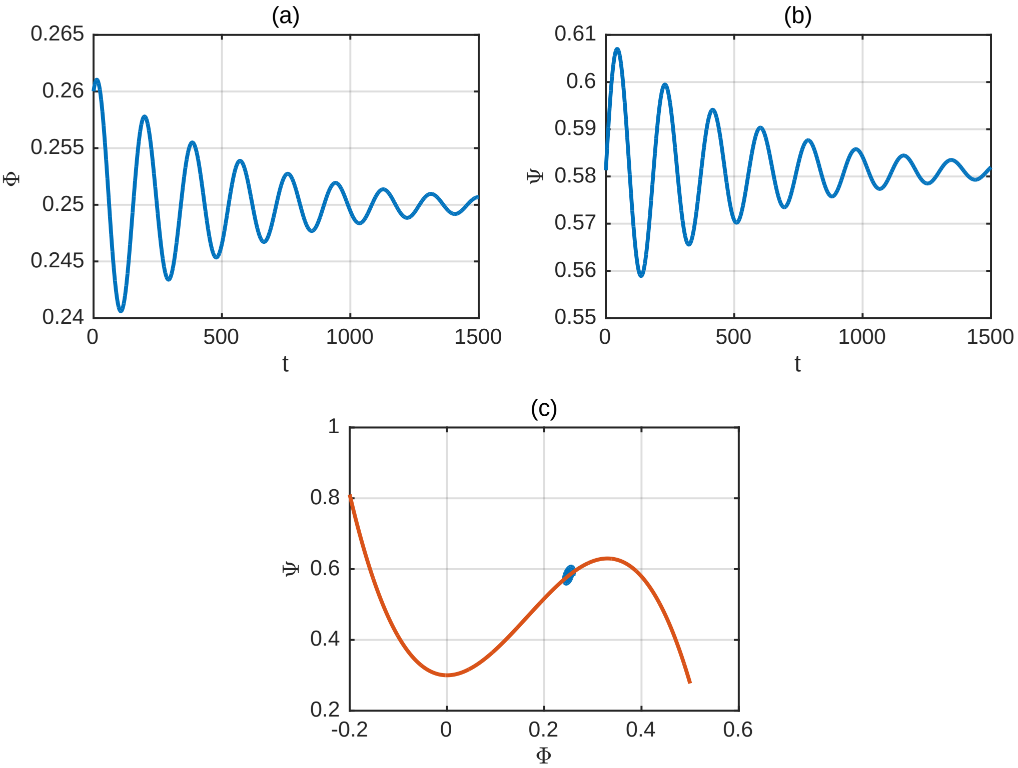

Fig. 2.9 Axisymmetric numerical results for $\Phi_0 = 0.25$ and $B = 0.2$.

Where c_0 is the sound speed and we have neglected the convection effect of the flow on acoustic propagation because the Mach number is small. Linearizing (2.79)

$$p'(x=0) = \rho_0 U \left(\alpha_c u' - \beta_c \frac{\partial u'}{\partial t} \right), \tag{2.82}$$

where

$$\begin{aligned} \alpha_c &= \frac{d\Psi_c}{d\Phi}(\Phi_0), \\ \beta_c &= \frac{R}{aU}. \end{aligned} \tag{2.83}$$

are parameters expressing the effect of the compressor and we have used the non-dimensional steady flow rate $\Phi_0 = u_0/U$.

Eliminating u' and ρ' from (2.81) gives the usual acoustic wave equation

$$\frac{\partial^2 p'}{\partial t^2} = c_0^2 \frac{\partial^2 p'}{\partial x^2}. \tag{2.84}$$

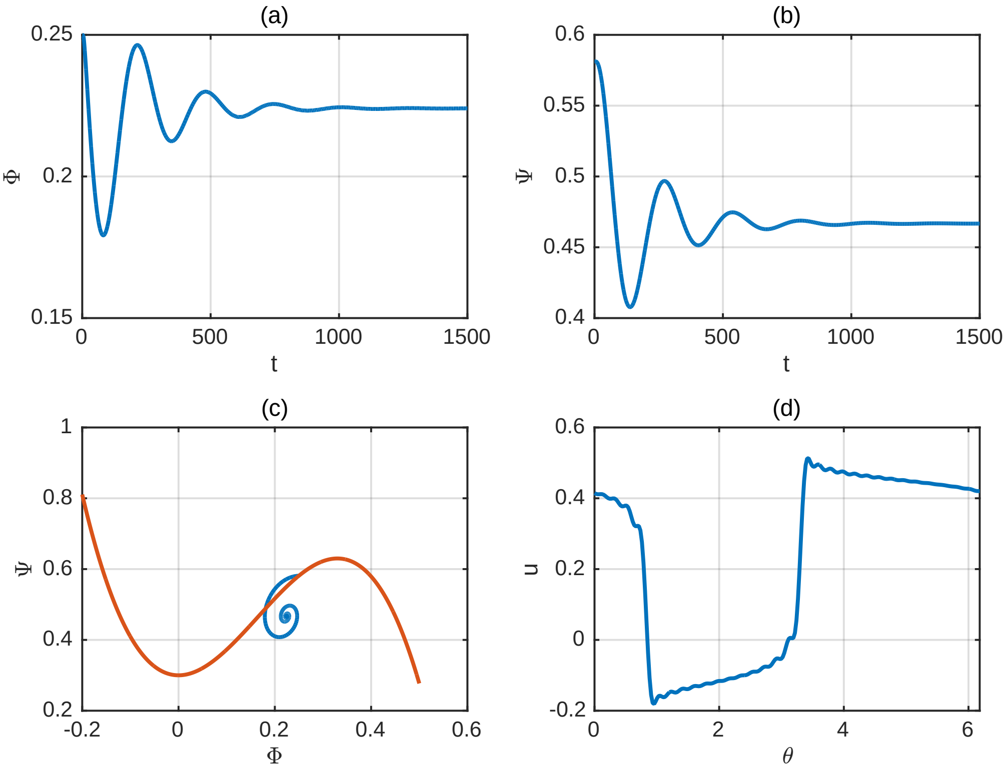

Fig. 2.10 Non-axisymmetric numerical results for $\Phi_0 = 0.25$ and $B = 0.3$.

For normal modes of the form $e^{-i\omega t}$, (2.84) gives

$$p' = Ae^{-i\omega t}\left(e^{ik(x-L)} + re^{-ik(x-L)}\right), \tag{2.85}$$

Where $k = \omega/c_0$. Of the terms in brackets, the first represents the acoustic wave propagating in the direction of increasing x, while the second term is its reflection from $x = L$. The quantity r is the (complex) reflection coefficient. As usual for acoustic reflection from the end of a pipe, we expect the condition $p'(x = L) = 0$ to hold approximately, implying $r \approx -1$. Using the first of equations (2.81), (2.85) and $k = \omega/c$,

$$u' = \frac{A}{\rho_0 c_0} e^{-i\omega t}\left(e^{ik(x-L)} - re^{-ik(x-L)}\right). \tag{2.86}$$

Finally, applying (2.82), (2.85), (2.86) and $k = \omega/c_0$,

$$1 + re^{2ikL} = M(\alpha_c + i\beta_c c_0 k)(1 - re^{2ikL}), \tag{2.87}$$

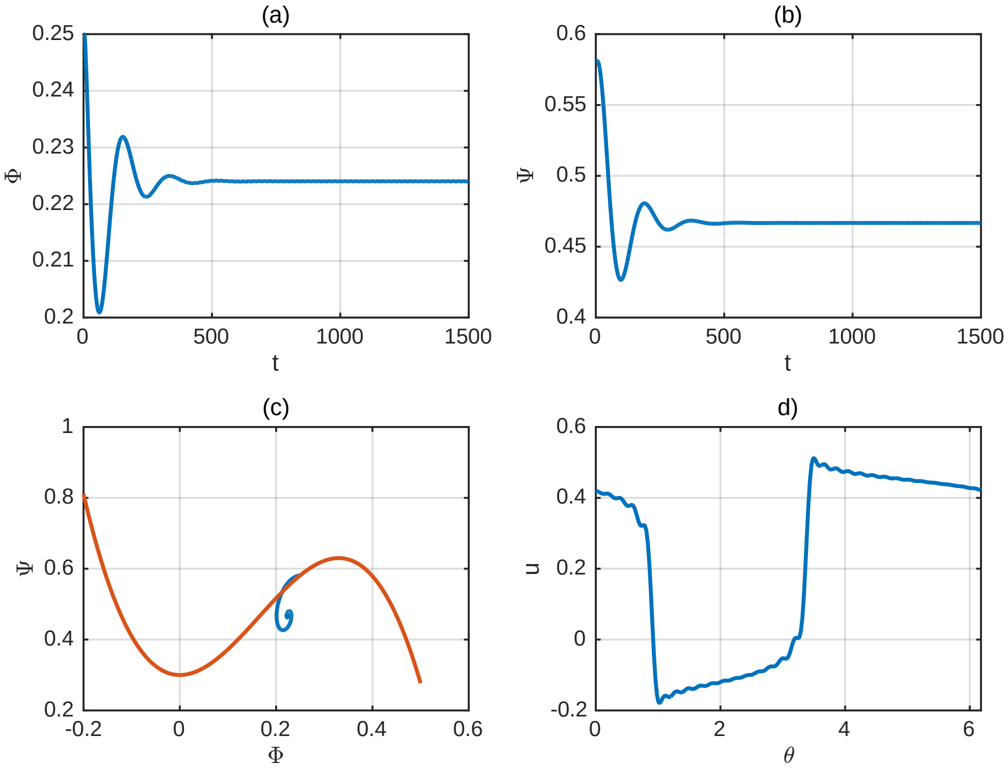

Fig. 2.11 Non-axisymmetric numerical results for $\Phi_0 = 0.25$ and $B = 0.2$.

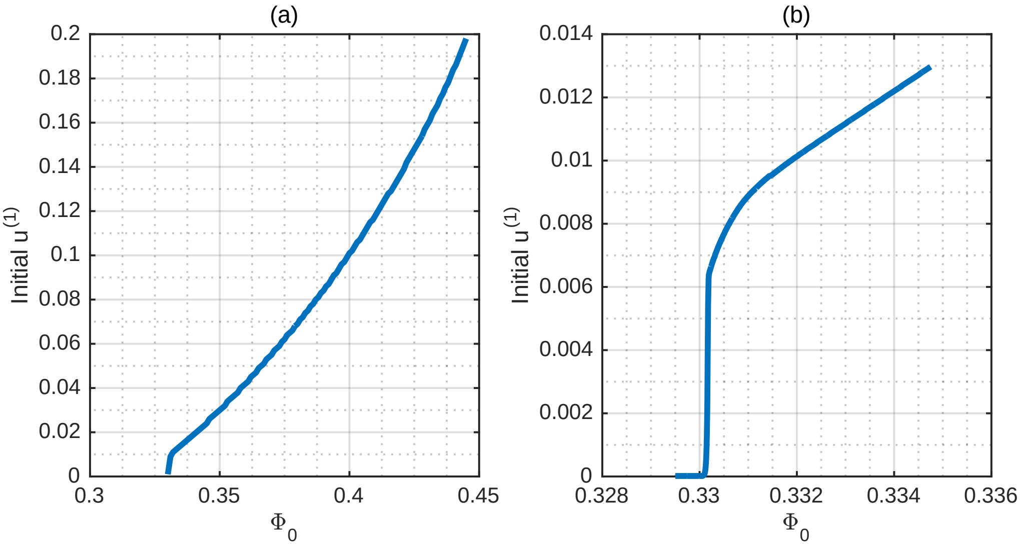

Fig. 2.12 Stability boundary for rotating stall. The horizontal axis gives Φ_0, while the vertical one represents the initial value of $u^{(1)}$. Rotating stall is found for all points to the left of the curve.

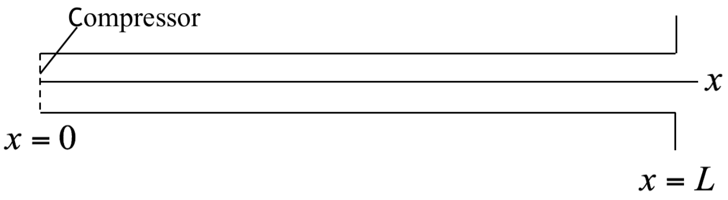

Fig. 2.13 Simplified geometry used to model the acoustic modes.

where $M = U/c_0$ is the compressor Mach number. Equation (2.87) is to be solved for k, leading to the modal frequencies via $\omega = c_0 k$.

The term on the right-hand side of (2.87) represents the effect of the compressor. Since M is small and $r \approx -1$, a first approximation of (2.87) is $e^{2ikL} = 1$, whose solutions are $k = n\pi/L$, hence

$$\omega = \frac{n\pi c_0}{L} \tag{2.88}$$

for the modal frequencies. This corresponds to n half-wavelengths along the length of the duct, a well known result for pipes with open ends. As we shall see, experimental observations are in satisfactory agreement with (2.88), thus confirming the expectation that $r \approx -1$.

The next-order approximation is obtained as follows. Using $e^{2ikL} \approx 1$, $r \approx -1$ and $k \approx n\pi/L$, the right-hand side of (2.87) can be approximated as

$$M(\alpha_c + i\beta_c c_0 k)(1 - re^{2ikL}) \approx 2M\left(\alpha_c + i\beta_c \frac{n\pi c_0}{L}\right). \tag{2.89}$$

The left-hand side of (2.87) can be written

$$1 + re^{2ikL} = 1 - |r|e^{i(2\delta+\phi)} = 1 - e^{i(2\delta+\phi)} + (1 - |r|)e^{i(2\delta+\phi)}, \tag{2.90}$$

where $r = -|r|e^{i\phi}$ expresses the reflection coefficient in terms of an amplitude and phase,

$$kL = n\pi + \delta \tag{2.91}$$

and δ is a (small) correction to the first approximation, $k = n\pi/L$. Since $r \approx -1$, $|r|$ is close to 1 and ϕ is small, hence (2.90) is approximated using Taylor's expansion by

$$1 + re^{2ikL} \approx -i(2\delta + \phi) + 1 - |r|. \tag{2.92}$$

Using (2.89) and (2.92) in (2.87),

$$\delta = iM\left(\alpha_c + i\beta_c \frac{n\pi c_0}{L}\right) - \frac{1}{2}(\phi + i(1-|r|)), \tag{2.93}$$

Using $\omega = c_0 k$, (2.91) gives

$$\omega = \frac{n\pi c_0}{L} + \frac{c_0}{L}\delta \tag{2.94}$$

as the next-order approximation of the modal frequencies. Writing $\omega = \omega_r - i\Delta$, (2.93) and (2.94) imply

$$\omega_r = \frac{n\pi c_0}{L} - \frac{c_0}{L}\left(\frac{1}{2}\phi + M\beta_c \frac{n\pi c_0}{L}\right), \tag{2.95}$$

$$\Delta = \frac{c_0}{L}\left(\frac{1}{2}(1-|r|) - M\alpha_c\right). \tag{2.96}$$

The modal time dependence can be written $e^{-i\omega t} = e^{-i\omega_r t}e^{-\Delta t}$, the first of whose factors has sinusoidal oscillations of frequency ω_r, while the second leads to exponential decay with damping factor Δ. (2.95) shows a small correction to the oscillation frequencies, which is due to phase changes on reflection at $x = L$ and the compressor. (2.94) shows that damping is partly due to loss of energy ($|r| < 1$) at $x = L$, but that there is also a contribution from the compressor, which can be either positive or negative, depending the sign of α_c, which is defined in (2.83) as the derivative of $\Psi_c(\Phi)$. For flow rates above the maximum of Ψ_c, $\alpha_c < 0$, so this contribution to Δ is positive, i.e. the compressor damps the acoustic modes. As the flow rate is decreased, the compressor contribution decreases and the modes become less damped. Once the maximum of Ψ_c is crossed, compressor damping becomes negative, i.e. the compressor gives energy the the modes instead of taking it away. This has the obvious potential for a new type of instability involving coupling both compressor instabilities and acoustic resonances of the duct.

2.4 Discussion

The main topic of this chapter has been the Moore-Greitzer model and its consequences for stability. The model was presented in section 2.1.1. It divides the flow into axisymmetric and non-axisymmetric parts: the former is represented by the flow rate, Φ, and plenum overpressure, Ψ, while the latter is expressed by the Fourier coefficients, $u^{(n)}$, of the axial velocity, $u(\theta)$, at the compressor. These flow variables evolve in time according to a system of differential equations. Characteristic functions, $\Psi_c(u)$ and $\Phi_T(\Psi)$, arise from modelling of the compressor and throttle. These functions need to be specified, as do the parameters a, l_c and B.

The model has steady, axisymmetric solutions, Φ_0, Ψ_0, corresponding to intersection of the curves in the Φ-Ψ plane representing the compressor and throttle characteristics (see figure 2.2). Stability of such flows to infinitesimal perturbations is investigated in section 2.1.2 by linearization of the model equations. The axisymmetric part of the perturbation, and each of the Fourier components of the non-axisymmetric part, are decoupled and hence can be studied separately. For the axisymmetric part, we find that instability can only occur if Φ_0 lies in the range of increasing $\Psi_c(\Phi)$, i.e. $\Psi_c' > 0$, where Ψ_c' is the derivative of $\Psi_c(\Phi)$ at Φ_0. For Φ_0 in this range, instability always occurs if $\Phi_T'\Psi_c' > 1$, where Φ_T' is the derivative of $\Phi_T(\Psi)$ at Ψ_0. On the other hand, when $\Phi_T'\Psi_c' < 1$, there is a critical value of B, below which the flow is stable to axisymmetric perturbations and above which it is unstable. This illustrates the general result that increasing B tends to encourage axisymmetric instability, leading to surge. The large-B surge cycle is discussed in the final paragraph of section 2.1.1 and illustrated by figures 2.3 and 2.7, the latter being the result of numerical integration using a particular choice of characteristic functions and model parameters.

Linear theory shows that non-axisymmetric instability occurs for all n in the range of increasing $\Psi_c(\Phi)$. Outside that range, neither axisymmetric nor non-axisymmetric instability is predicted by that theory. Since non-axisymmetric instability occurs inside the range, a general initial perturbation will lead to unstable growth if $\Psi_c(\Phi)$ is increasing at Φ_0. Thus, taking into account both the axisymmetric and non-axisymmetric parts of the flow, the linear instability criterion is simply $\Psi_c' > 0$.

The problem with linear theory is that, when it predicts instability, the perturbation has unbounded exponential growth, taking it beyond the range of infinitesimal amplitude for which linear analysis holds. Weakly nonlinear theory was developed in section 2.1.3. This approach applies close to the linear instability threshold, i.e. throttle setting which place Φ_0 near the maximum of $\Psi_c(\Phi)$, and for small perturbations. Using asymptotic expansions in powers of a small parameter, ε, and multiple scaling in time, we derived evolution equations for the non-axisymmetric mode amplitudes (the axisymmetric part of the flow passively follows the non-axisymmetric part). As usual in weakly nonlinear theory, there are two cases: supercritical and subcritical instability. The two are distinguished by the parameter β, given by equation (2.69). If $\beta < -2$, the instability is supercritical, while it is subcritical when $\beta > -2$.

In the supercritical case, nonlinearity is stabilizing and the basic flow, Φ_0, Ψ_0, is stable in the range, $\Psi_c' < 0$, predicted by linear theory. Beyond that range, linear instability means that the basic flow is not realized and the flow is replaced by a more complicated unsteady, non-axisymmetric one. The transition from one flow to the other as the linear instability boundary is crossed is continuous: the perturbation starts at zero amplitude.

The subcritical case is quite different. Nonlinearity is destabilizing and instability can occur in the range deemed stable by linear theory. It does so if the perturbation exceeds a certain threshold amplitude, which decreases as the linear stability boundary is approached. When instability occurs, we expect it to lead to a finite-time singularity according to the weakly nonlinear amplitude equations. Thus, the theory predicts the perturbation amplitude to go to infinity at finite time. Of course, this takes it beyond the scope of the theory and into the strongly nonlinear regime. All that can be said about the new flow resulting from the instability is that it is quite different from the basic flow.

Section 2.2 gives some results of numerical integration of the model. Specific compressor and throttle characteristic functions and values of the parameters a, l_c are chosen as representative of the experimental test rig. This leaves B and the throttle setting, represented by a nominal steady flow rate, Φ_0, as parameters which are varied to see their effects on flow stability. The curve in figure 2.6 shows the boundary separating axisymmetric instability and stability in the Φ_0-B plane according to linear theory. Axisymmetric instability occurs to the left of the curve. The dashed line represents the maximum of $\Psi_c(\Phi)$, which is the linear stability threshold for non-axisymmetric modes. Thus, the flow is linearly stable to the right of the dashed line and unstable to the left.

Figures 2.7-2.11 show numerical results for a particular value of Φ_0 and three of B. The calculation was initialised using a small, axisymmetric perturbation of Ψ_0, Φ_0 (since the flow is initially exactly axisymmetric it remains so: this excludes non-axisymmetric instability). Figures 2.7 and 2.8 correspond to points above the critical curve in figure 2.6 and show growth of the perturbation and the development of a surge cycle. The large value of B used in figure 2.7 means that surge cycle resembles figure 2.3. It also means that deep surge (negative flow rates over part of the cycle) occurs. The moderate value of B in figure 2.8 leads to milder surge. In figure 2.9, the point in the Φ_0-B plane lies below the critical curve in figure 2.6 and small damped oscillations occur. The basic steady flow is stable and is approached at large times. These results illustrate a general result: using axisymmetric initialisation, we always obtained stability or instability in accord with linear theory, which suggests that axisymmetric instability is supercritical. On the other hand, $\beta > -2$ for the given choice of characteristic functions, so non-axisymmetric instability is subcritical.

Figures 2.10 and 2.11 show results for $\Phi = 0.25$ and the same values of B as figures 2.8 and 2.9. The difference is that a non-axisymmetric initial perturbation is used. The result is rotating stall: Ψ and Φ approach constant values, but these are not Ψ_0, Φ_0. Furthermore, the limit approached in the Ψ-Φ plane of figures 2.10c and 2.11c lies below the compressor characteristic, representing a loss of performance of the compression system due to rotating stall. Figures 2.10d and 2.11d show the stall cell at a particular instant of time. The flows approached at large time are the same for the two values of B. This is because the model is independent of B when Ψ is time independent.

Figure 2.12 illustrates the subcritical nature of the rotating-stall instability using results of numerical calculations with $B = 0.35$. The horizontal axis gives Φ_0 (representing the throttle setting), while the vertical one is a measure ($u^{(1)}$) of the initial, non-axisymmetric perturbation. The curves represent the instability boundary: rotating stall occurs everywhere to the left of these curves (note that figure 2.12b is just a zoom of 2.12a). The curves start out on the horizontal axis at the stability boundary predicted by linear theory for non-axisymmetric modes (the dashed line in figure 2.6). These results confirm that non-axisymmetric instability is subcritical for the present choice of characteristic functions.

Finally, motivated by the observation of acoustic duct modes in our experiments, section 2.3 develops a simple model of such modes. This model incorporates the Moore-Greitzer modelling of the pressure rise across the compressor. We find that the modal frequencies should be close to those obtained by taking an integral number of half-wavelengths along the length of the duct. As we shall see, this is in satisfactory agreement with observations. Furthermore, the modal damping is found to be affected by the presence of the compressor, making a contribution proportional to $-\Psi_c'(\Phi_0)$. This contribution is positive for Φ_0 above the maximum of $\Psi_c(\Phi)$, hence the compressor extracts energy from the acoustic modes in that range. As Φ_0 is decreased, the compressor contribution to the damping drops, to reach zero at the maximum of $\Psi_c(\Phi)$. It then becomes negative, meaning that the compressor donates to, rather than extracts from, the energy of the acoustic modes.

Chapter 3

Experimental facility

This chapter presents the test rig, control system and sensors used in the experiment.

3.1 Test rig

The test rig consists of four main parts (see figure 3.1): the compressor, ducts, plenum, and flow-regulation valve (or throttle). A TCS (Turbulence Control Structure) is placed in front of the compressor to reduce the level of turbulence in the inlet airflow.

3.1.1 Compressor

We use an LP3 axial electric fan (see figure 3.2), constructed by the Technofan group for the Airbus A380 project. It is a mono-stage compressor with a 17-blade rotor followed by a 23-blade stator. The compressor came equipped with a control system which allows the rotor rotational speed to be varied between 2000 and 10300 rpm. The maximum static-pressure difference across the compressor is about 2500 Pa. The Mach number is low: less than 0.3.

3.1.2 Ducts

The main duct runs between the compressor and plenum and is composed of three identical cylindrical aluminium sections (see figure 3.3) each 994 mm long, with an inside diameter of 170 mm, followed by a Venturi and a divergent section.

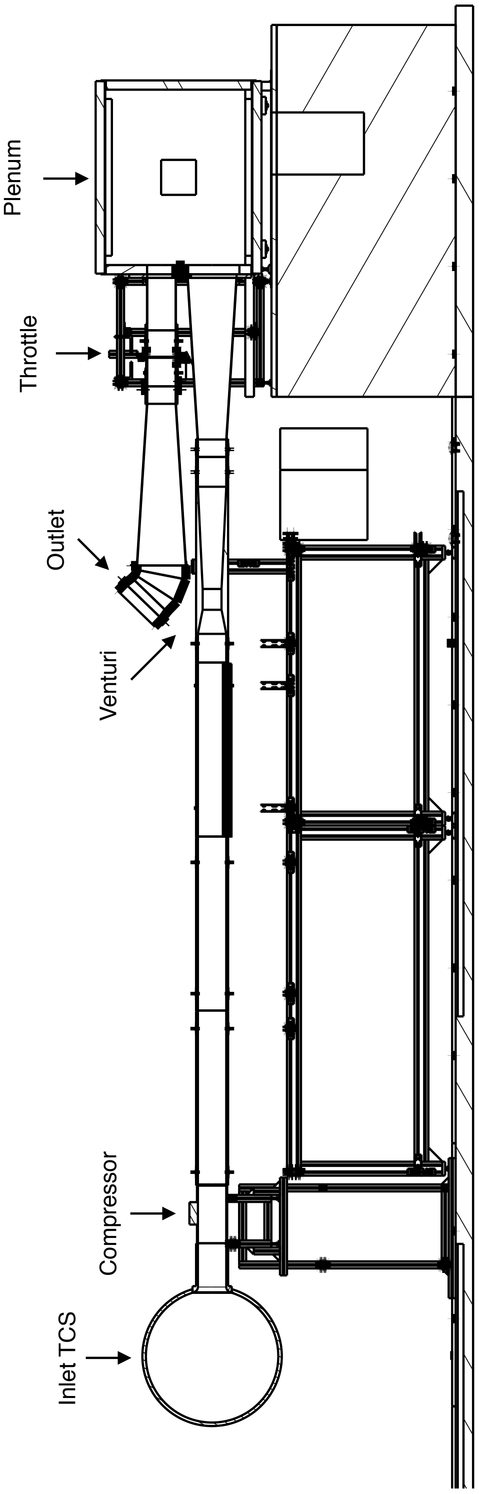

Fig. 3.1 Plan of the entire test rig.

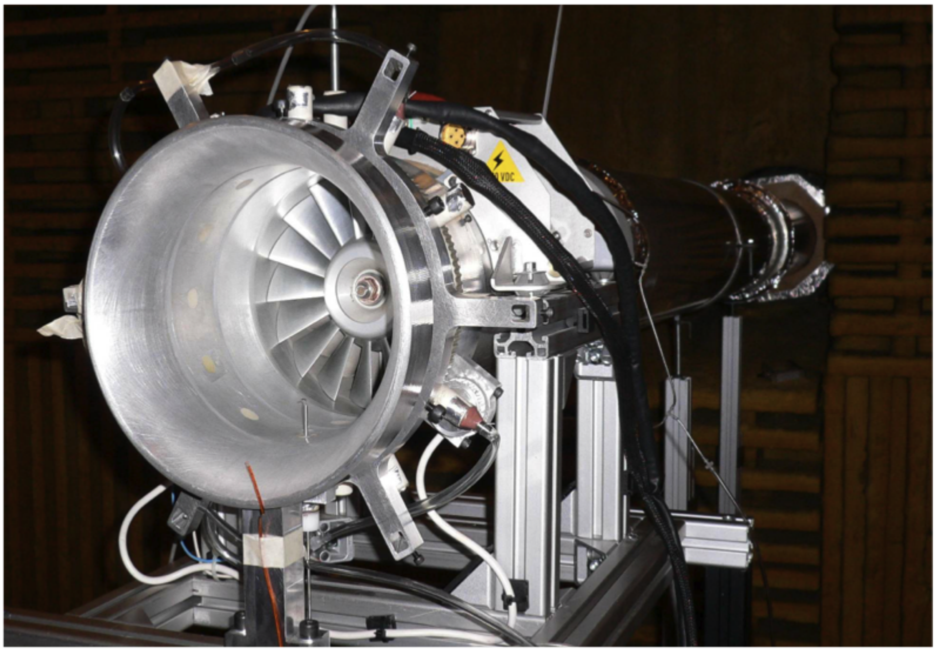

Fig. 3.2 The Technofan LP3 axial electric compressor (the TCS has not been installed).

The divergent section (see figure 3.4) is placed between the Venturi and the plenum to reduce head loss of the airflow entering the plenum. The inside diameter varies from 170 mm at the inlet to 283 mm at the entrance to the plenum. Because the Mach number is low, the flow is nearly incompressible, leading to a reduction in velocity by a factor of about $(170/283)^2 = 0.36$. Since the head loss on entry to the plenum is proportional to the square of the velocity, it is reduced by a factor of about 8, compared to the case without a divergent section. A divergent section with the same geometry is also used at the exit of the whole system, right after the regulation valve.

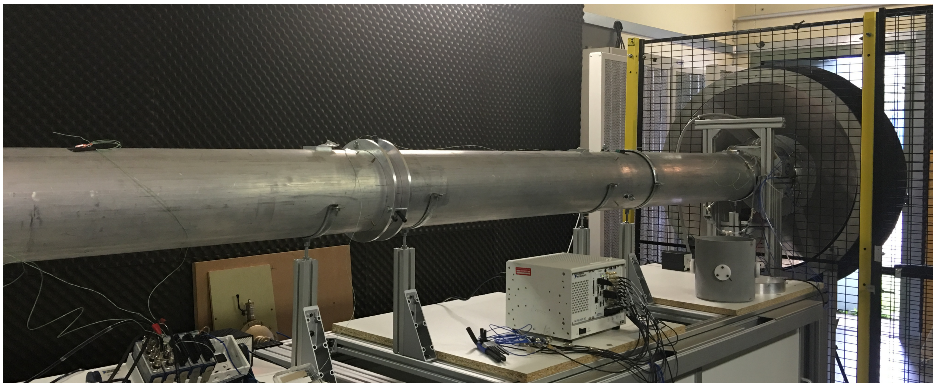

Fig. 3.3 The main duct downstream of the compressor.

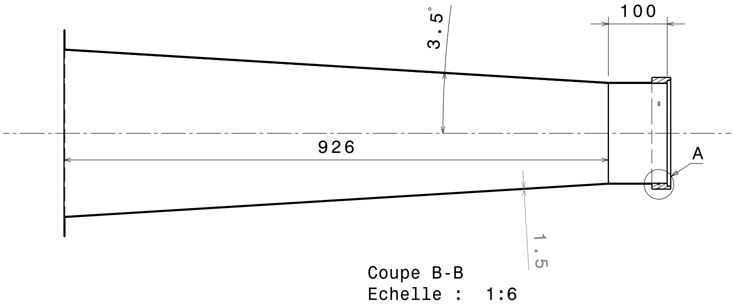

Fig. 3.4 Geometry of the divergent section.

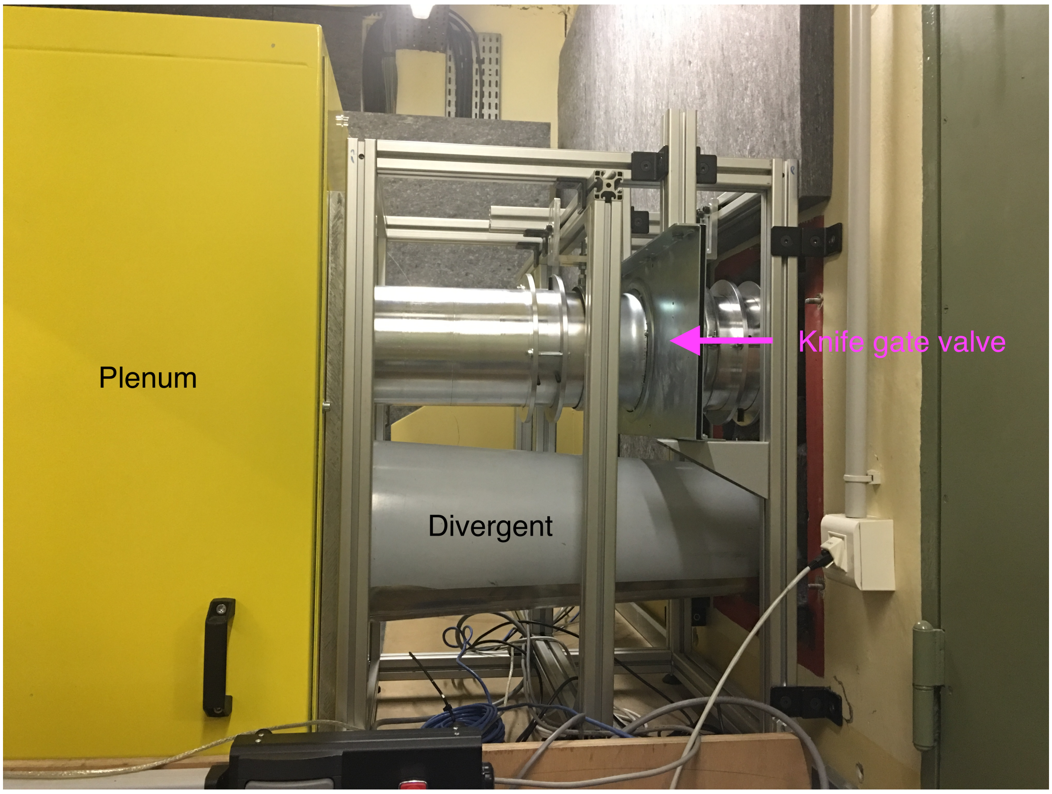

Fig. 3.5 Inlet and outlet of the plenum, with the inlet divergent section and the knife gate regulation valve.

3.1.3 Plenum

The plenum is a 1 m×1 m×1.5 m rectangular box, whose volume corresponds a moderate Greitzer B-parameter: about 0.5. As a precaution in the case of strong surge, a rapidly opening valve was placed on one of the walls of the plenum. This valve was set to trigger if the plenum pressure exceeded a certain threshold. However, surge was, in fact, never observed, and this valve was not triggered. Figure 3.5 shows the plenum, as well as its inlet ducts. It also shows the flow-regulation valve.

3.1.4 Regulation valve

The regulation valve consists of a knife-gate valve and a linear actuator consisting of a stepper motor and a threaded shaft. The system has a precision of 0.1 mm. The controller/driver module TMCM-1110 stepRocker is used to control the motor, with high smoothness and precision.

3.1.5 Active forcing using a compressed-air jet

One of the original motivations of the experiment was to study the properties of the modes predicted by linear theory in the stable regime near the stability threshold. The idea is to apply small impulsive forcing to the system and observe the response. According to linear theory, the modes should appear as damped oscillations, which become less and less damped as the threshold is approached. This approach is similar to tapping an elastic structure and measuring the result to determine the frequencies, damping rates and spatial distribution of the normal modes, a technique often used in studies of structural vibration. In such studies, temporal Fourier spectra show peaks at the modal frequencies, whose widths are a measure of the damping rates of the modes. Although, as will appear in the next chapter and for reasons which are not entirely clear, the expected modes of instability were not observed, a forcing device was developed and employed. For this reason, and because it may help others to find a way towards the original goal, we describe the forcing system here.

An impulsive jet of compressed air is injected through a small hole in the duct wall. Two locations were tried: one at mid-distance between the rotor and the stator, the other 3 cm upstream of the rotor. Compressed air is supplied at constant pressure to a valve, which opens and closes to produce the impulsive jet. We expect non-axisymmetric instability modes at frequencies which are some fraction of the rotor rotation frequency. The latter depends on the rotation rate, which lies between 2000 and 10300 r.p.m., giving a frequency between 30 and 170 Hz. To excite the modes requires that the valve be sufficiently rapid-acting that

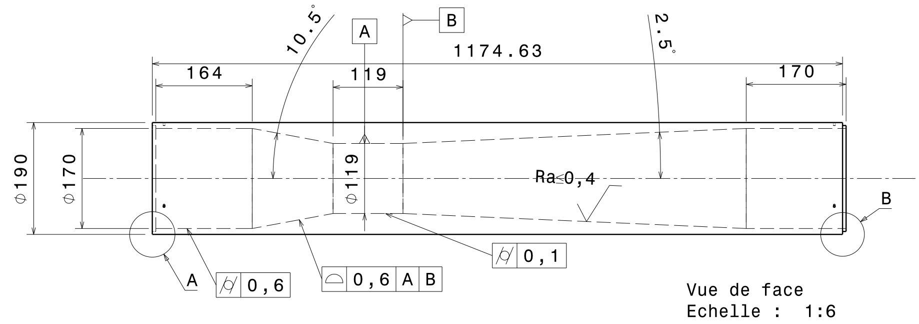

Fig. 3.6 Geometry of the Venturi flow meter.

the system can deliver energy in their frequency range, say up to 200 Hz. This implies a valve capable of opening and closing in a few milliseconds. We chose a high-speed Matrix solenoid valve, driven by a speed-up board. The valve opens and closes in response to an electrical pulse, whose duration determines that of the jet. The pressure delivered to the valve can be varied, hence controlling the intensity of the jet. Thus, both the duration and amplitude of the impulsive perturbation are controllable.

3.2 Measurement devices

3.2.1 Flow rate measurement

The steady volumetric flow rate is determined using a Venturi located as indicated in figure 3.1. The Venturi geometry is shown in figure 3.6 and follows the NF EN ISO 5167-4 standard. The difference of static pressure between the inlet and the section of minimum cross-sectional area was measured using a UNIK 5000 silicon pressure sensor. Because the design of the Venturi is standard, formulae giving the flow rate are available [24] and were used to compute the flow rate.

3.2.2 Steady pressure measurements

In addition to those of the Venturi, static pressure measurements were performed at three other locations, summarised by table 3.1. A barometer outside the flow measured the atmospheric pressure, while a UNIK 5000 sensor was used to determine the static-pressure difference across the compressor and another gave the plenum pressure. Temperature was also measured at the three locations.

	Environment	Compressor	Plenum
Use	Atmospheric pressure	Upstream-downstream pressure difference	Static pressure in plenum
Device	Barometer	UNIK 5000 sensor	UNIK 5000 sensor

Table 3.1 List of the pressure measure points, their uses and measuring devices.

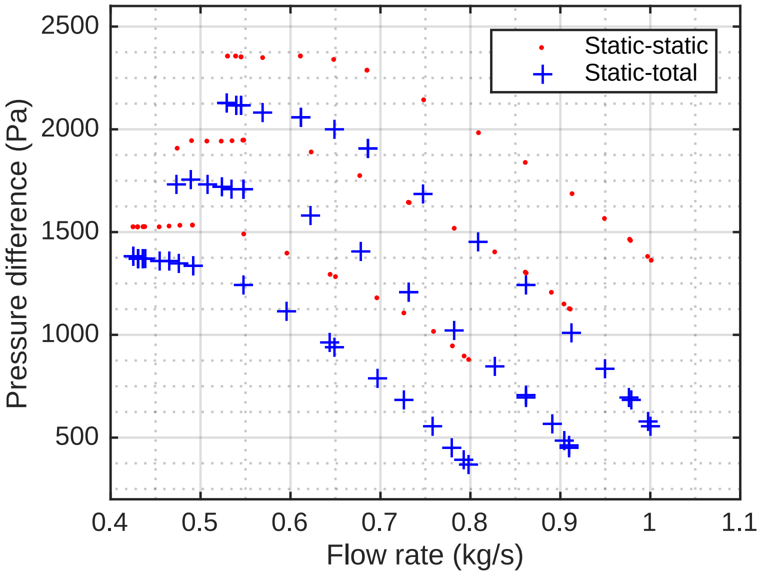

Fig. 3.7 Measured compressor characteristics (static-total as blue plus signs, static-static as red points) for rotor speeds of 8000 rpm, 9000 rpm and 9870 rpm.

Pressure taps are installed upstream and downstream of the compressor. At the upstream location, four holes in the casing are equally spaced around the circumference and joined together by PVC tubes, thus averaging the pressure over the holes. A similar setup is used at the downstream location. A UNIK 5000 sensor is used to measure the difference between the downstream and upstream pressures. As we saw in our discussion of the Moore-Greitzer model in the previous chapter, it is the difference between the static pressure downstream and the total pressure upstream (rather than the static-static difference) which is more pertinent to instability. Thus, we subtract the upstream dynamic pressure, $\rho v^2/2$, from the static-static measured value, where the velocity v is determined from the flow rate measured by the Venturi. Figure 3.7 shows both static-static and static-total differences as a function of flow rate for three rotor speeds.

A pressure sensor is mounted on the plenum wall and serves not only to measure the pressure in the plenum, but also as a trigger for the anti-surge system discussed in section 3.1.3.

Fig. 3.8 PCB377B01 microphone.

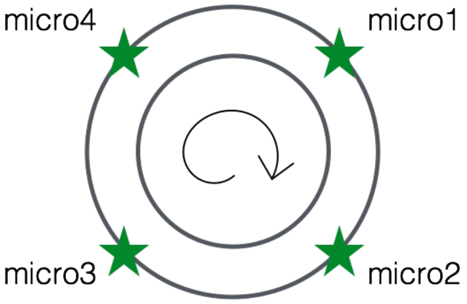

Fig. 3.9 Circumferential positions of the 4 microphones.

3.2.3 Unsteady pressure measurements

Four microphones (PCB 377B01, see figure 3.8) were used to measure the unsteady pressure. These microphones are mounted flush with the casing at a location just upstream of the compressor and are equally spaced around the circumference (see figure 3.9). The location of the microphones was chosen as follows. As discussed in section 2.1.1, we expect the non-axisymmetric component of the flow to decay exponentially away from the compressor at distances comparable with the duct radius, $\sim$10 cm. In the presence of rotating stall, we want to be able to measure this component, which means the microphones should not be too far upstream. On the other hand, the rotor consists of individual blades which will generate a disturbance at the blade-passing frequency and its harmonics, with or without instability. We want to minimise the effects of this disturbance on the measured pressures, to more clearly see any stall cell. As for the axisymmetric component arising from rotating stall, we expect the blade-induced disturbance to decay exponentially upstream, this time at distances of the order of the duct radius divided by the number of rotor blades, $\sim$10/17 cm. Thus, the microphones should not be too close to the compressor. We chose a location 3 cm upstream of the rotor.

Finally, in those cases where impulsive forcing upstream of the compressor was used, one of the microphones was replaced by the impulsive jet injector.

Chapter 4

Experimental results

This chapter gives results obtained using the test rig and sensors described in the previous chapter. The main results concern the pressure fluctuations observed at the microphones, which are located just upstream of the compressor, as described in section 3.2.3. Depending on the aspect of the results under discussion, different signal processing techniques (e.g. frequency spectra and wavelet analysis (see e.g. Stoica and Moses [36])) are used. As noted earlier, surge was never observed, perhaps because the Greitzer B-parameter ($B \approx 0.4$) is too low. Thus, only results concerning rotating stall are available.

The term "rotating stall" is perhaps inappropriate to describe our results. As we shall see, although a rotating stall cell can be identified just after stall inception, the end result of the instability is not a well-defined stall cell which rotates at constant angular velocity around the compressor. Instead it appears to consist of a strong and apparently random element, combined with a rotating one. These observations are quantified in section 4.4 using spectra, as well as auto- and cross-correlations between the different microphones. We nonetheless keep the traditional nomenclature, rotating stall, as a description of the observed instability.

4.1 Compressor characteristics

Figure 4.1 shows the static-static and static-total compressor characteristics for the three rotational speeds, 8000, 9000 and 9870 r.p.m., on which we focus in this chapter. As the flow is throttled for a given rotational speed, the flow rate decreases and the pressure difference rises. This is the stable regime. However, beyond a certain throttle position, both flow rate and pressure difference undergo a discontinuous jump to lower values. This is symptomatic of rotating stall and occurs at a well-defined throttle position. The right-hand figure shows that instability occurs before the maximum of the static-total pressure difference is reached. According to the Moore-Greitzer model, the maximum defines the linear instability threshold.

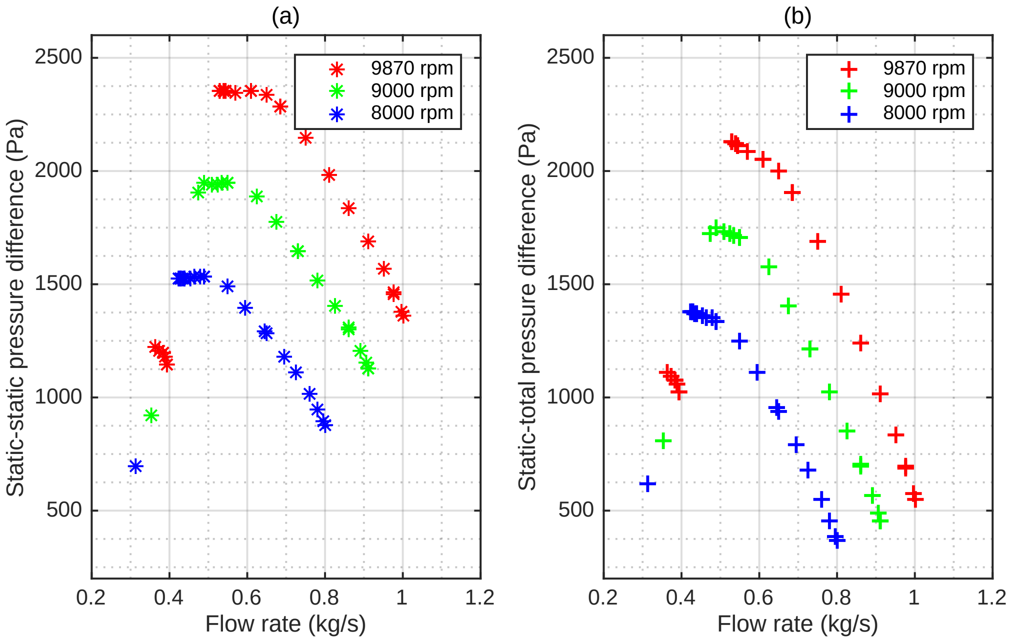

Fig. 4.1 Characteristics at three rotational speeds.

This, together with the discontinuous jump, suggests that the instability is subcritical, in keeping with the conclusion reached at the end of section 2.1.3 using a cubic fit to the experimental compressor characteristic.

The throttle setting can be represented by the displacement (in millimetres) of the gate valve from the fully open position. Thus, 0 mm corresponds to the fully open position, while 180 mm represents a fully closed valve. The threshold for instability was found to be 97 mm, 98 mm and 99 mm for the rotational speeds 8000, 9000 and 9870 r.p.m.. Below the threshold, the basic flow is stable, whereas rotating stall arises once the threshold is crossed.

4.2 The stable regime

4.2.1 Acoustic modes

Figure 4.2 gives frequency spectra obtained using the Welch method with 50% overlap. Peaks are observed at frequencies close to the expected locations of the acoustic duct modes. As discussed in section 2.3, we expect such acoustic resonances at frequencies for which there are an integral number of half-wavelengths along the duct between the compressor and plenum. Given a duct length $\sim$5 m and a sound speed $\sim$300m/s, this gives resonances at multiples of about 30 Hz, in reasonable agreement with the observations. Thus, we interpret the peaks as due to acoustic modes. An additional, and sharper, peak corresponds to the rotational frequency of the machine. Whereas the acoustic modes have the same frequencies at different rotational speeds, the frequency of this peak is speed dependent. Figure 4.3 shows results of Morlet-wavelet analysis (see Tse and Lai [39] for details). The lowest acoustic mode appears as a horizontal band at about 30 Hz. Observe that the intensity of the mode in intermittent, suggesting that it is being driven by a random source. Time series are shown in figure 4.4a. It is apparent that there is significant high-frequency content. To make the acoustic modes evident, we low-passed the data (with an equiripple finite-impulse response filter with passband frequency 120 Hz and stopband frequency 150 Hz). The result is shown in figure 4.4b. The oscillations reflect the acoustic modes. Note that all four microphones oscillate in phase, suggesting that, as expected, the acoustic modes are axisymmetric.

In figure 4.2, it is seen that the acoustic peaks become higher and narrower when the machine is throttled to near the stall threshold. This is in accord with the analysis of section 2.3, in which it was shown that the compressor contributes to damping of acoustic modes. As the machine is throttled, the slope of the compressor characteristic decreases, hence its contribution to the damping factor (predicted to be proportional to the derivative of $-\Psi_c(\Phi)$) also decreases. The result is that the acoustic intensity increases significantly as the stability threshold is approached. This increase in intensity is quite large, suggesting that the compressor contribution dominates more traditional sources of acoustic damping (e.g. losses on reflection at the ends of the duct).

4.2.2 Forcing

As discussed in section 3.1.5, one of the original motivations of the experiment was to study the properties of the modes predicted by linear theory in the stable regime near the stability threshold using forcing by an impulsive air jet. We hoped to see peaks in the frequency spectrum representing the instability modes just prior to their becoming unstable. The idea was that, since, according to linear theory, the instability modes have damping factors which decrease as the instability threshold is approached, they should become more intense near the threshold. This is similar to the mechanism of intensification of the acoustic modes described above. However, the observed spectra were always dominated by the acoustic peaks and we could not identify additional peaks. Despite this disappointing result, we briefly describe the work.

As described in section 3.1.5, compressed air is supplied at constant pressure to a solenoidal valve, which opens, then closes. The pressure and duration of valve opening can be varied, thus controlling the intensity and duration of the resulting jet. A variety of pressures, up to 70000 Pa above the atmospheric pressure, and durations (5 ms, 8 ms, 10

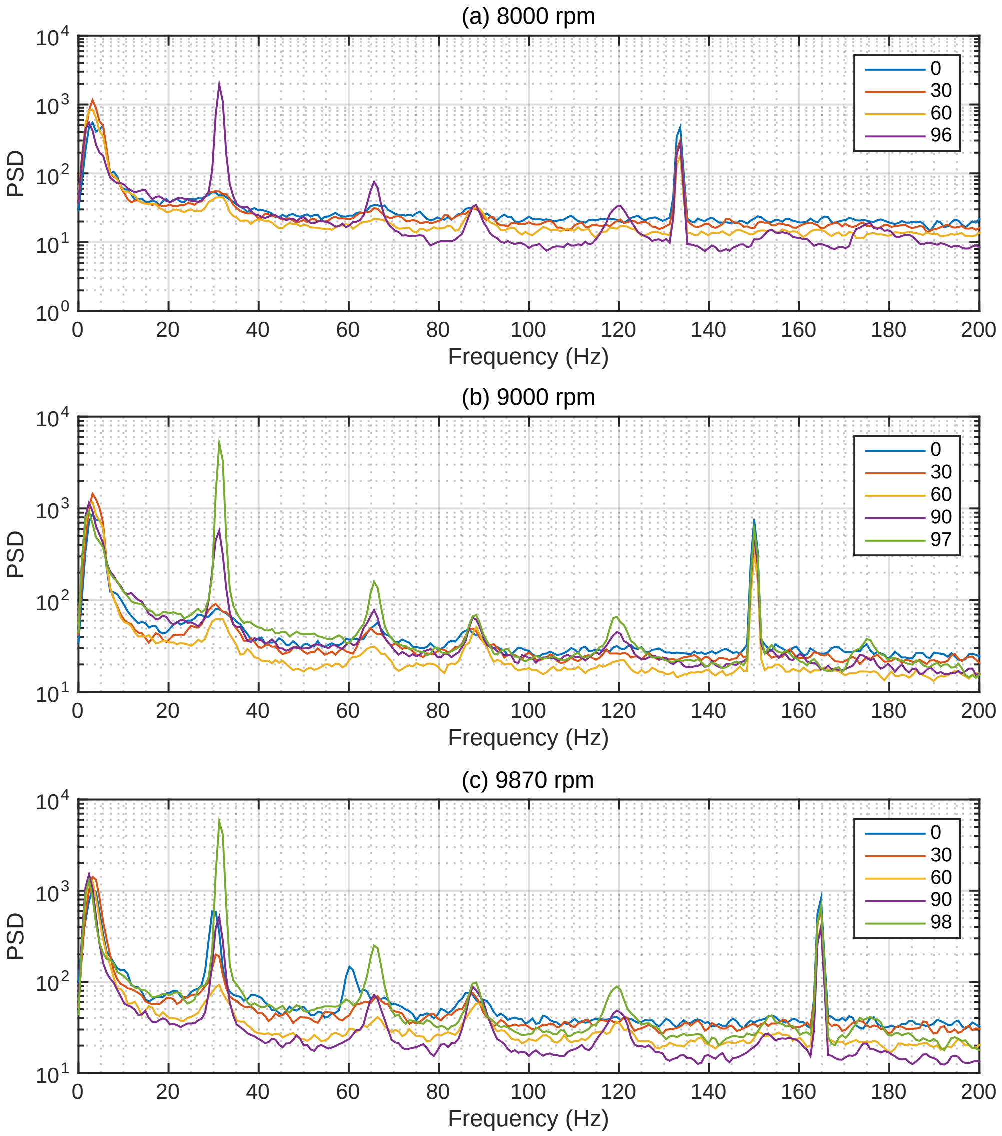

Fig. 4.2 Frequency spectra in the stable regime for microphone 1. The gate-valve positions (in mm) are indicated in the boxes, which provide keys to the various coloured curves.

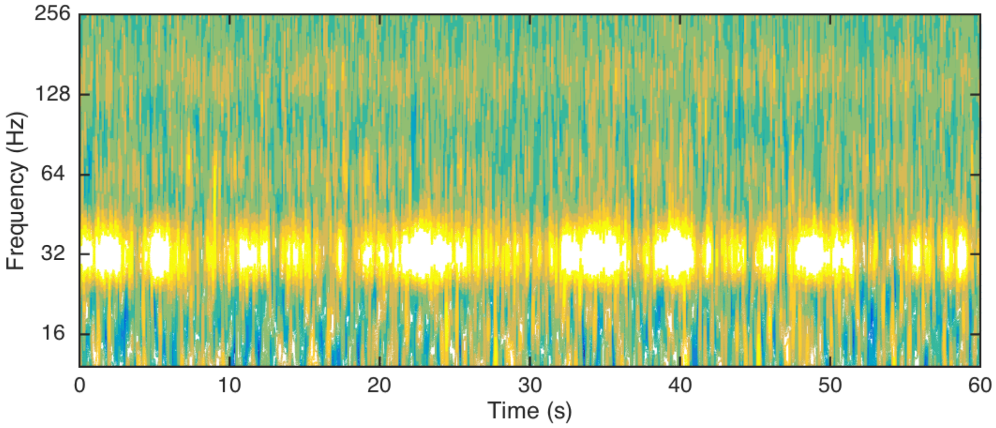

Fig. 4.3 Wavelet power spectrum (microphone 1, 9000 rpm, throttle setting 97 mm).

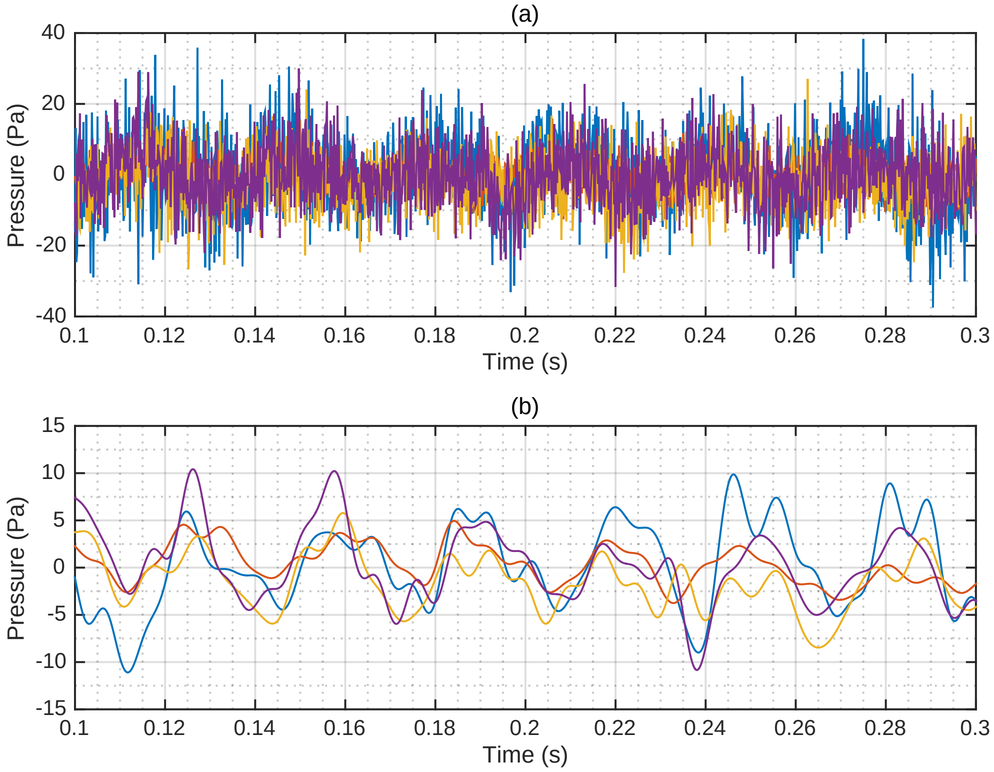

Fig. 4.4 a) Measured pressure fluctuations at all 4 microphones (9000 rpm, throttle setting 97 mm); b) Low-pass filtered version of a).

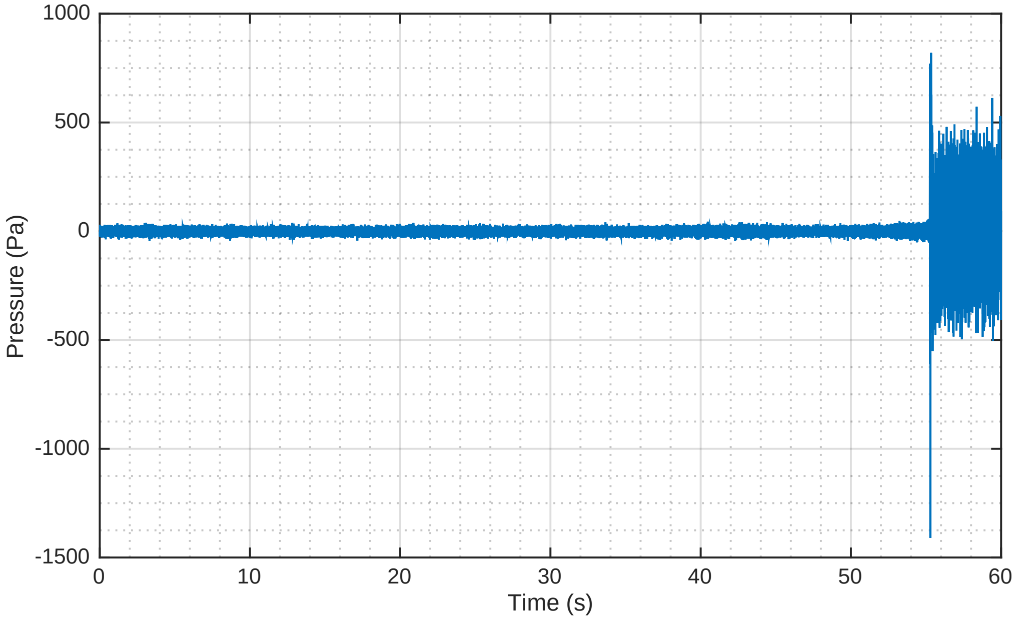

Fig. 4.5 Pressure fluctuations at microphone 3 (9000 rpm, throttle setting 98 mm).

ms and 15 ms) of the electrical pulse that triggers valve opening and closing were tried. As discussed in section 3.1.5, two locations of the injector were used, one at mid-distance between the rotor and the stator, the other 3 cm upstream of the rotor. As noted above, in no cases did we see spectral peaks representing instability modes.

4.3 Stall onset and development

Once the instability threshold is crossed, rotating stall occurs. Figure 4.5 illustrates stall inception for a throttle setting close to the threshold: the sudden increase in the pressure fluctuations reflects stall onset. Prior to this time, there are acoustic fluctuations, as in the stable case. We found that, once it began, stall continued indefinitely.

The time of onset of stall appears to be randomly varying: keeping the same nominal parameters (rotation rate and throttle setting) it may occur after a few seconds, but for other runs one must wait for several minutes. This is what might be expected for a subcritical instability of a flow subject to random perturbations: the perturbation amplitude must exceed a certain threshold. There is a certain probability of this occurring in a given time interval, but the precise time of instability inception is unpredictable. Weakly nonlinear theory predicts that the threshold amplitude decreases as the linear stability boundary is approached. Thus, it becomes more and more likely that the instability will occur, until it becomes a certainty when the flow is linearly unstable. As a result, we expect to have to wait less and less time for stall to arise as the machine is throttled, until immediate stall occurs. This is in agreement with our observations. The large increase in pressure fluctuations when stall occurs is also symptomatic of a subcritical instability: as we saw in section 2.1.3, weakly nonlinear theory predicts that the result of such an instability is growth of the perturbation to infinite amplitude. Of course, the result is always finite in reality.

Figure 4.6 shows a wavelet power spectrum including stall onset. Prior to stall, acoustic modes are apparent at about 30 and 60 Hz. As for the stable regime represented in figure 4.3, the acoustic intensity fluctuates randomly on a time scale of the order of seconds. The figure shows that the acoustic modes are intermittent and disappear following stall onset. The $\sim$30 Hz mode is seen to increase in intensity a few seconds before stall inception. This was clearly audible when performing the experiment. For security and ear-protection reasons, the compressor was separated by a wall from the room in which the operators worked. The ducts pass through this wall to the plenum, which is on the operators' side (see figure 3.5 for a view from that side). The acoustic modes could be heard as an hum intermittent. The hum grew progressively louder a few seconds before stall onset (thus providing a qualitative instability predictor), before disappearing abruptly at onset. This made it easy to know if stall was occurring or not. Although it is difficult to distinguish cause and effect, one might speculate on acoustic modes as a subcritical trigger for stall. The cessation of noise when stall sets in suggests that pressure fluctuations due to stall are confined near the compressor, which may bring to mind the discussion of the local nature of non-axisymmetric modes in chapter 2. From figure 4.6, it is apparent that the spectral content of the pressure fluctuations becomes broad-band when stall is present. Figure 4.7 shows results from another experimental run; the time interval being much smaller than in figure 4.6, acoustic intermittency is no longer apparent, but the increasing intensity of the $\sim$30 Hz acoustic mode is evident.

Figure 4.8a shows the pressure fluctuations at all four microphones for a short interval of time centred on stall onset. It shows acoustic oscillations prior to stall. Following stall onset, the pressure fluctuations grow to a maximum, then decrease to a roughly constant intensity. As noted in the introduction to this chapter, the end result (developed stall) is not a well-defined stall cell which rotates at constant angular velocity around the compressor (this would give time-periodic oscillations). Instead it has a strong, apparently random element. Figure 4.8a also illustrates the much higher amplitude and frequencies of the pressure oscillations (compared to the acoustic ones) resulting from stall.

Figure 4.8b shows a zoom of the acoustic oscillations(no filtering employed, which are more evident than those in the stable regime(figure 4.4)), while figure 4.8c shows stall onset. One can identify a growing disturbance which passes from one microphone to the next

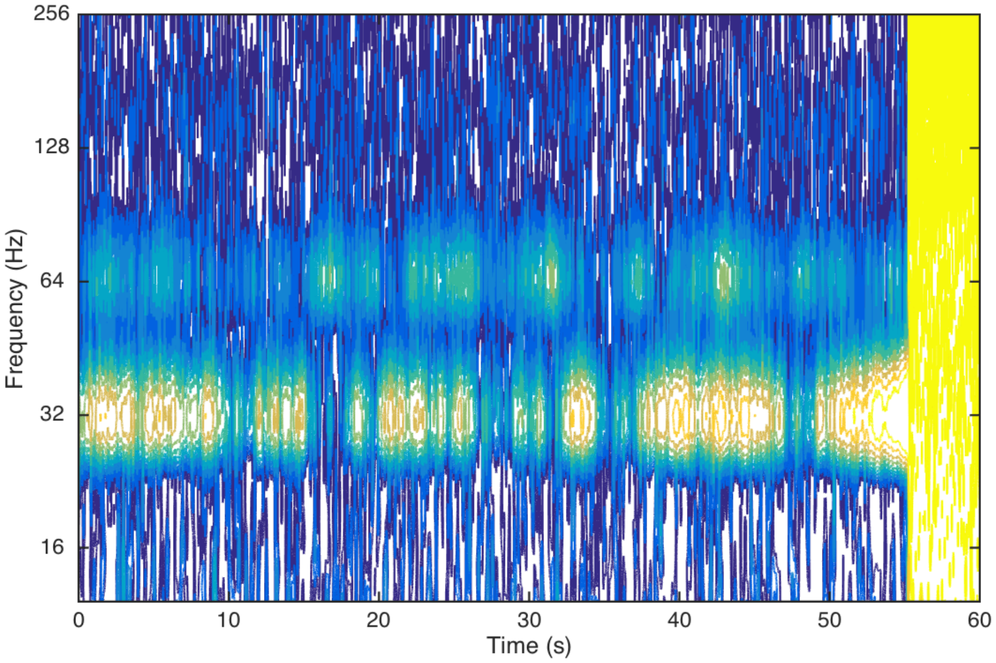

Fig. 4.6 Wavelet power spectrum (microphone 3, 9000 rpm, throttle setting 98 mm, figure 4.5a).

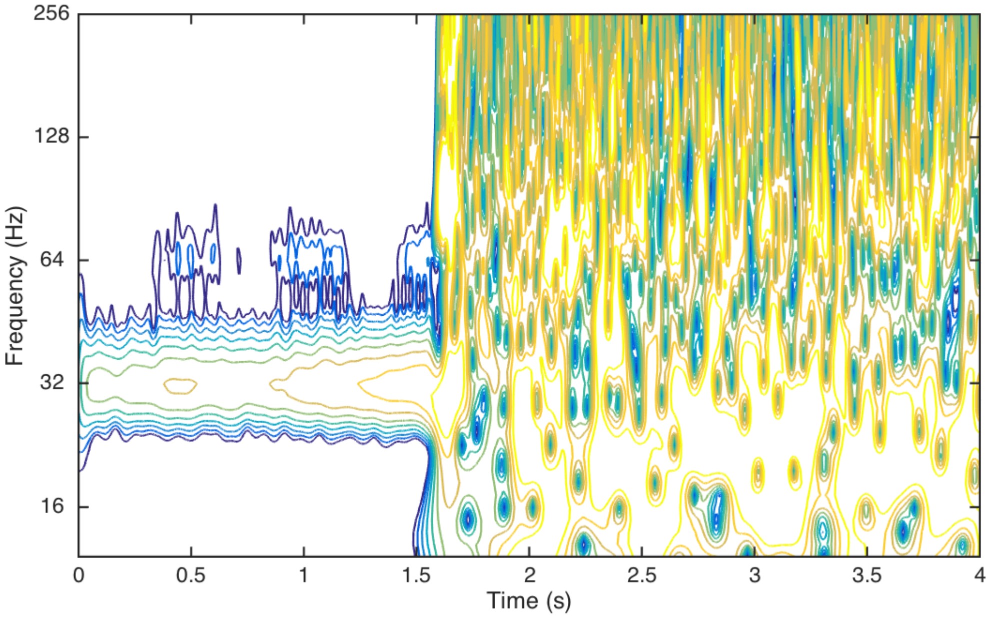

Fig. 4.7 Wavelet power spectrum (microphone 3, 9000 rpm, throttle setting 98 mm, figure 4.5b).

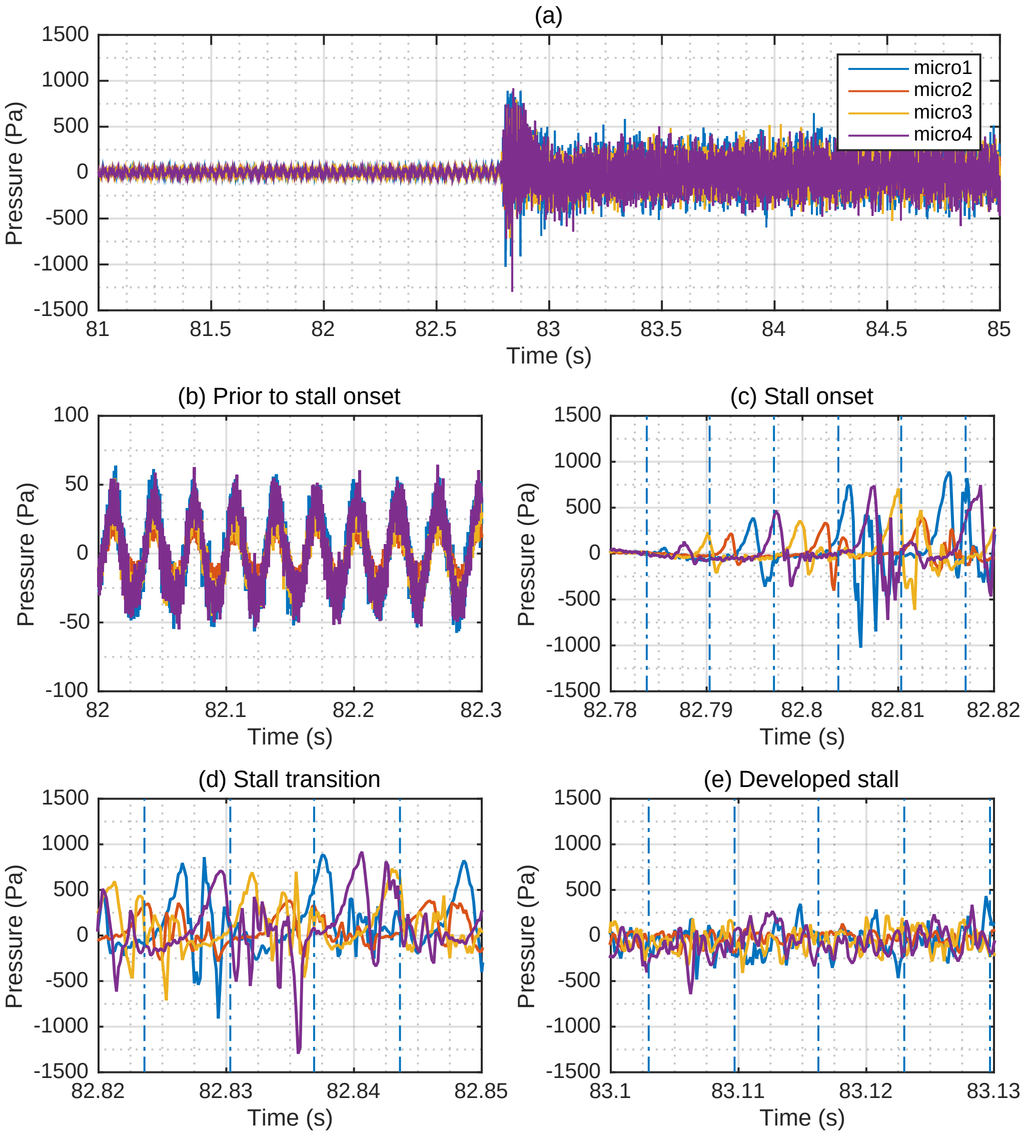

Fig. 4.8 Stall inception (9000 rpm, throttle setting 98 mm). The blue dash-doted lines in figures c-e are separated by a machine rotation period.

around the compressor circumference. This disturbance can be interpreted as a stall cell which rotates in the same sense as the machine at about 70% of its speed. However, as noted above, a classical rotating stall cell is not attained: the rotating disturbance breaks down after about two machine-rotation periods and the pressure fluctuations have apparently random oscillations thereafter. We refer to the phase following breakdown of the rotating cell and prior to reaching developed stall as stall transition (this phase is illustrated by figure 4.8d). Finally, figure 4.8e shows the random oscillations of developed stall. Although both 4.8d and 4.8e have random oscillations, they differ markedly in amplitude. The mechanisms driving stall to randomness, its subsequent statistical relaxation to developed stall, and random stall in general, remain to be elucidated.

4.4 Developed stall

We expect developed stall to be statistically stationary, thus making it appropriate to use techniques such as Fourier spectral analysis and correlations. The objective of this section is to use such techniques to try to better understand the random type of stall we have observed.

4.4.1 Pressure fluctuations and spectra

Figures 4.9 and 4.10 illustrate the random, relatively high-frequency, character of pressure fluctuations at the four microphones for three different rotation rates, while figures 4.11-4.13 show the corresponding frequency spectra. These figures show a peak at about 20 Hz, followed by a range, extending up to about 1 kHz, in which the spectrum appears to follow an approximative power law (the straight lines correspond to $f^{-0.9}$ dependency), before dropping off rapidly at higher frequencies. Clearly the spectrum is broadband. These results may remind the reader of turbulence spectra, but this is probably misleading. They represent the results of random stall, the mechanisms driving which remain to be elucidated.

Figure 4.14-4.16 show cumulative spectra, which are the integral of the power spectral density from 0 Hz to f Hz, divided by the integral up to the maximum frequency (which is 3200 Hz), plotted as a function of f. Thus, the figures give the fraction of the energy below a given frequency. It will be seen that about 80% of the energy lies below 1 kHz.

4.4.2 Correlations

Figures 4.17-4.19 show auto- and cross-correlation functions. By definition, cross-correlations lie in the range -1 to +1, where +1 represents the case where the microphone signals are the same to within a multiplicative factor and a time shift. The smaller the correlation, the

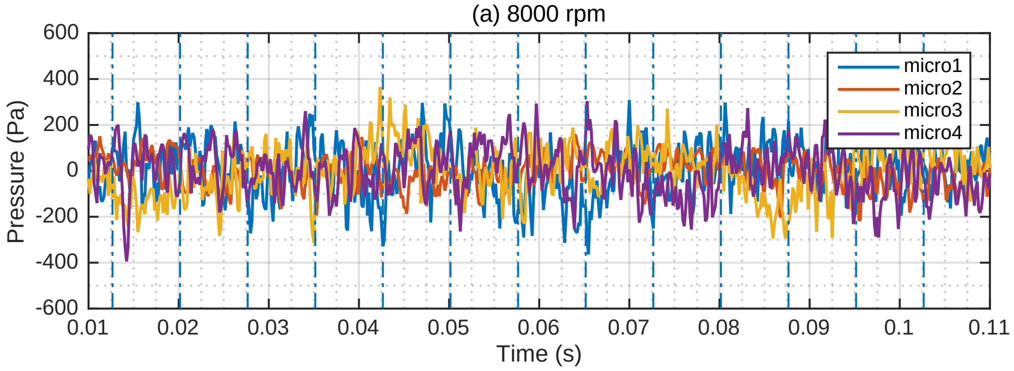
(a) 8000 rpm

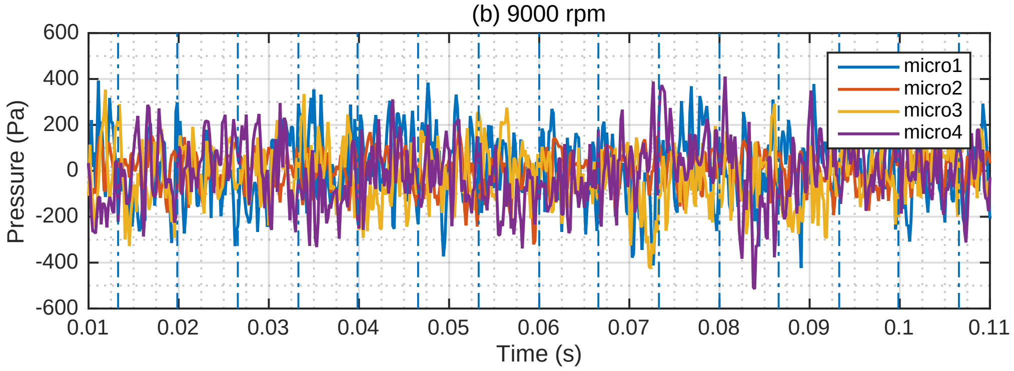
(b) 9000 rpm

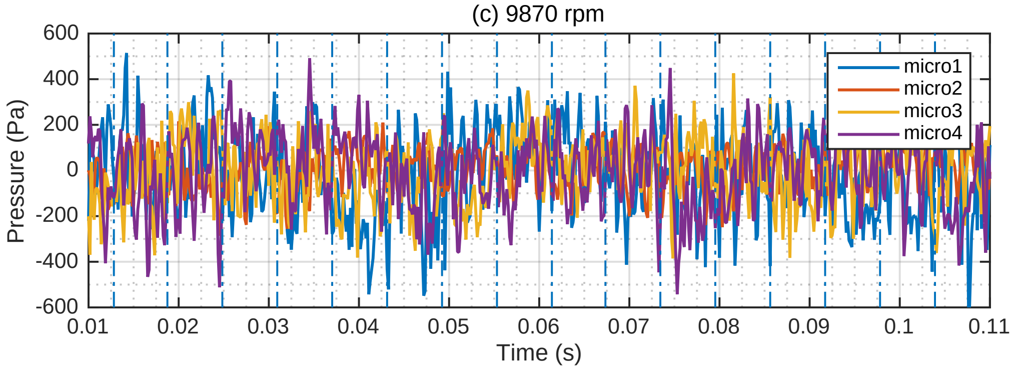
(c) 9870 rpm

Fig. 4.9 Pressure fluctuations at all four microphones for developed stall and three different rotation rates. The throttle settings are: a) 97 mm, b) 98 mm and c) 99 mm. The blue dash-dot lines in each figure are separated by a machine rotation period.

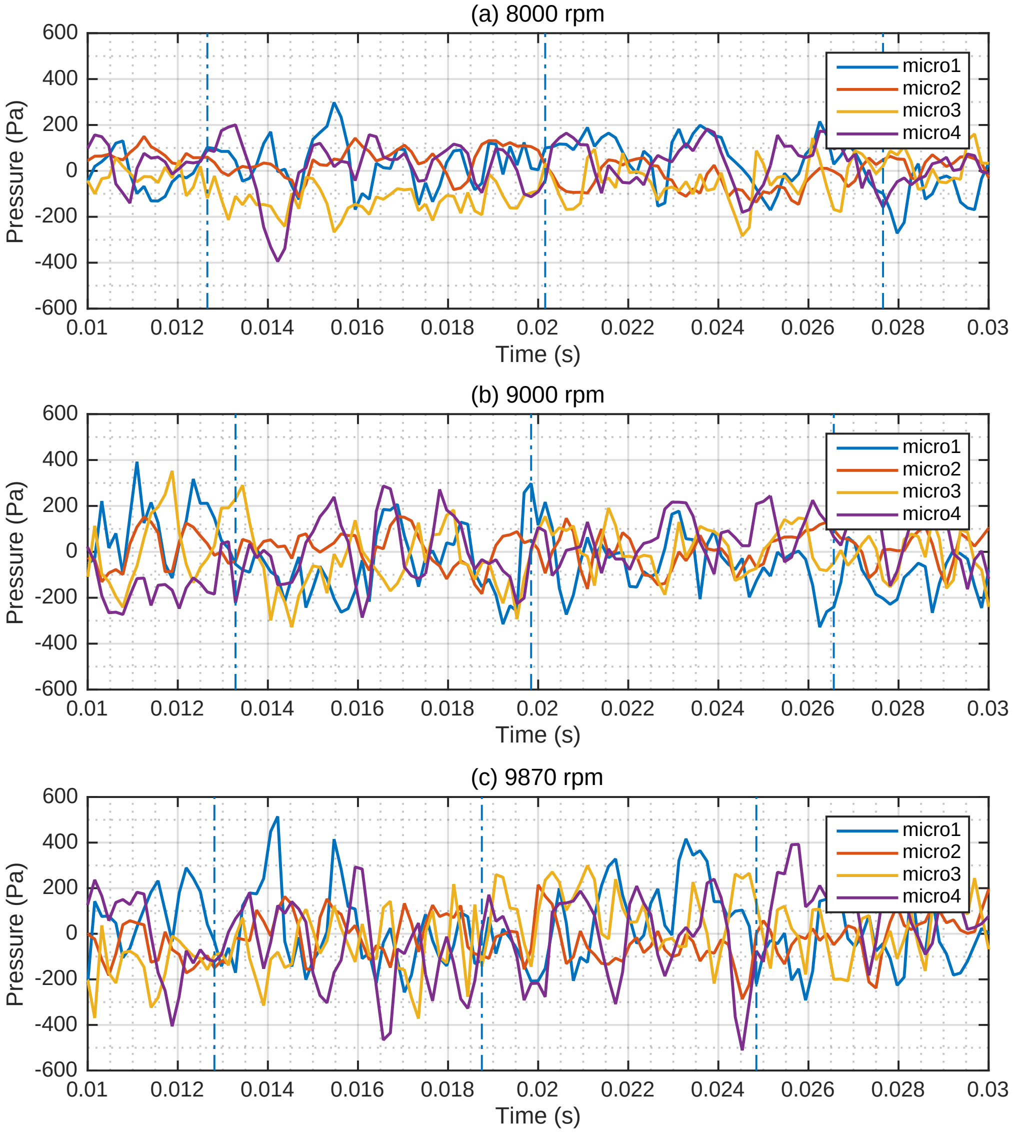

Fig. 4.10 As for figure 4.9, but with a different time scale.

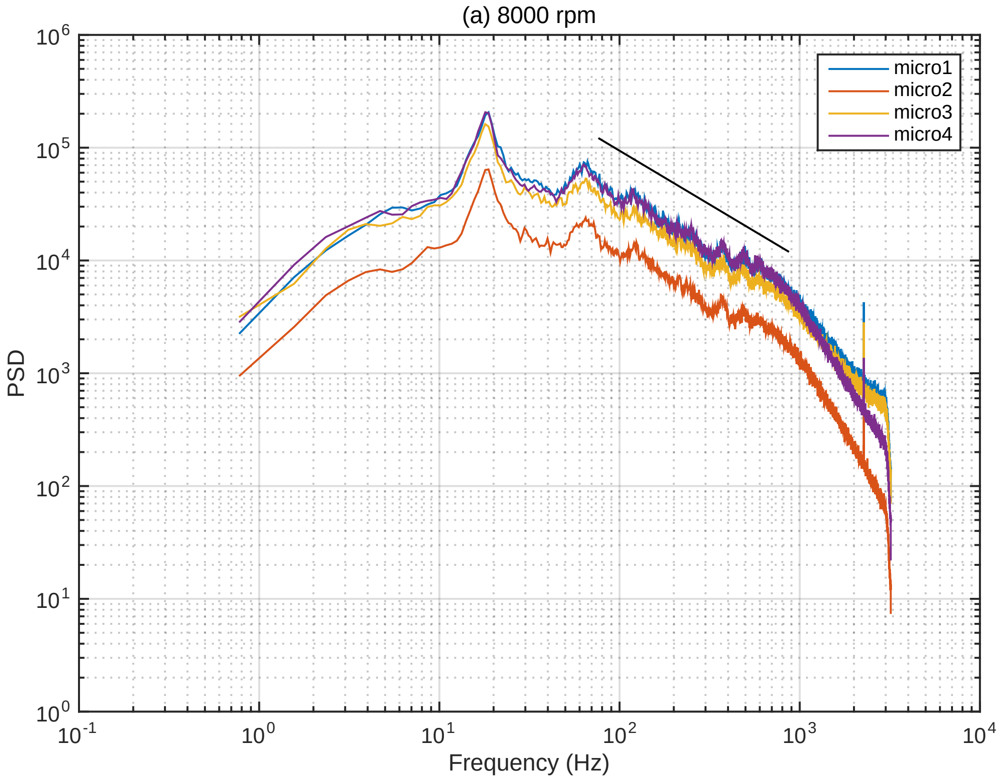

Fig. 4.11 Frequency spectra corresponding to figure 4.9a.

less the signals are related. Figure 4.17a shows a sharp peak at time difference 0 (where the auto-correlation is, of course, 1) and decaying oscillations of frequency ∼20 Hz. The spectrum is the Fourier transform of the auto-correlation function: the sharp peak in figure 4.17a corresponds to the high frequencies in 4.11, while the oscillations are reflected in the 20 Hz peak of the spectrum. Figures 4.17b and 4.17c also have oscillations of frequency ∼20 Hz. Similar remarks apply to figures 4.18 and 4.19, though the oscillations are less marked. The decay of both auto- and cross-correlation functions at large time-shifts indicates that the pressure fluctuations at sufficiently large temporal separation are uncorrelated. Note that adjacent microphones are more correlated than microphones which are oppositely located.

To gain a better understanding of the ∼20 Hz peak of the spectra and the oscillations of the correlations, the pressure fluctuations were low-pass filtered (an equiripple finite-impulse-response filter with passband frequency 40 Hz and stopband frequency 50 Hz) and cross-correlation functions of the filtered signals calculated. Figure 4.20 shows some results. It will be seen that microphone 1 is quite strongly correlated with microphone 2 at a time difference of about 0.013 s, and with microphone 3 for a time shift double this. A possible interpretation is that there is a rotating cell which takes about 0.05 s to complete a full rotation.

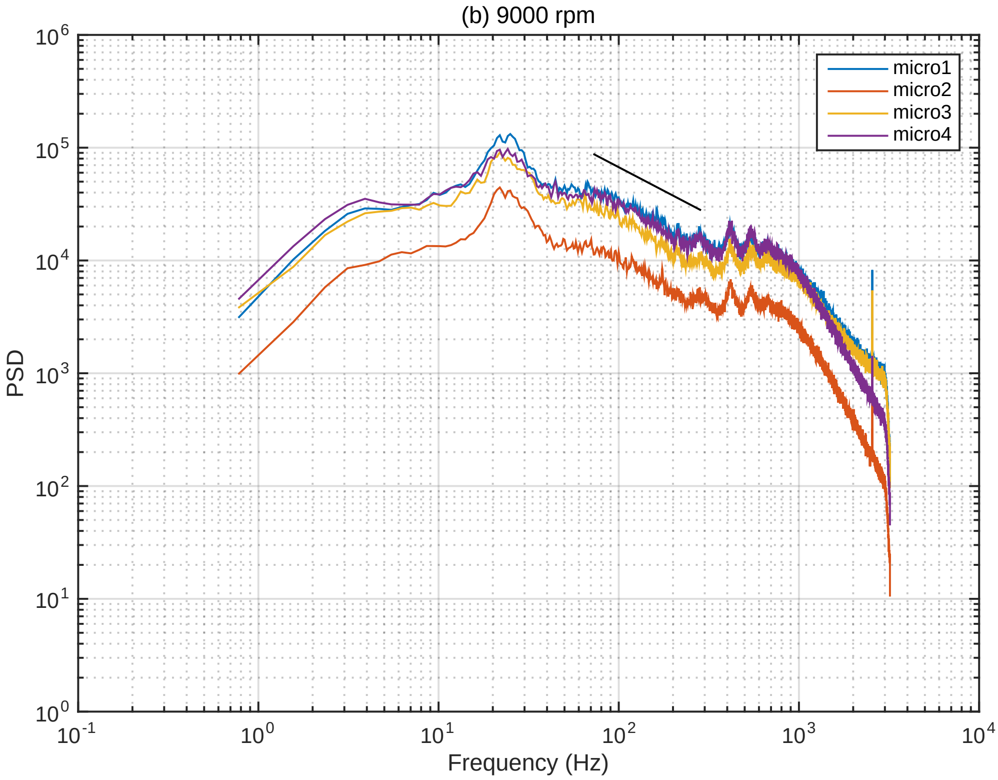

Fig. 4.12 Frequency spectra corresponding to figure 4.9b.

This would explain the 20 Hz spectral peak and oscillations of the correlations. The decay of the correlation functions in figure 4.20 implies that the cell is not just a simple rotating flow structure, like classical rotating stall, but undergoes random fluctuations as it rotates.

4.5 Discussion

In this chapter we have described and discussed our experimental results on instability. On the one hand, surge was never observed, while, on the other, random stall was found to occur when the machine was sufficiently throttled. This is apparent from the compressor characteristics (figure 4.1), which show a decrease in flow rate and pressure rise across the compressor when stall occurs. Stall occurs before the maximum of the static-total compressor characteristic is reached. The maximum is the linear stability threshold according to the Moore-Greitzer model. This, together with the discontinuous decrease in flow rate and pressure rise, suggests that the instability is subcritical, in accord with the conclusion at the end of section 2.1.3.

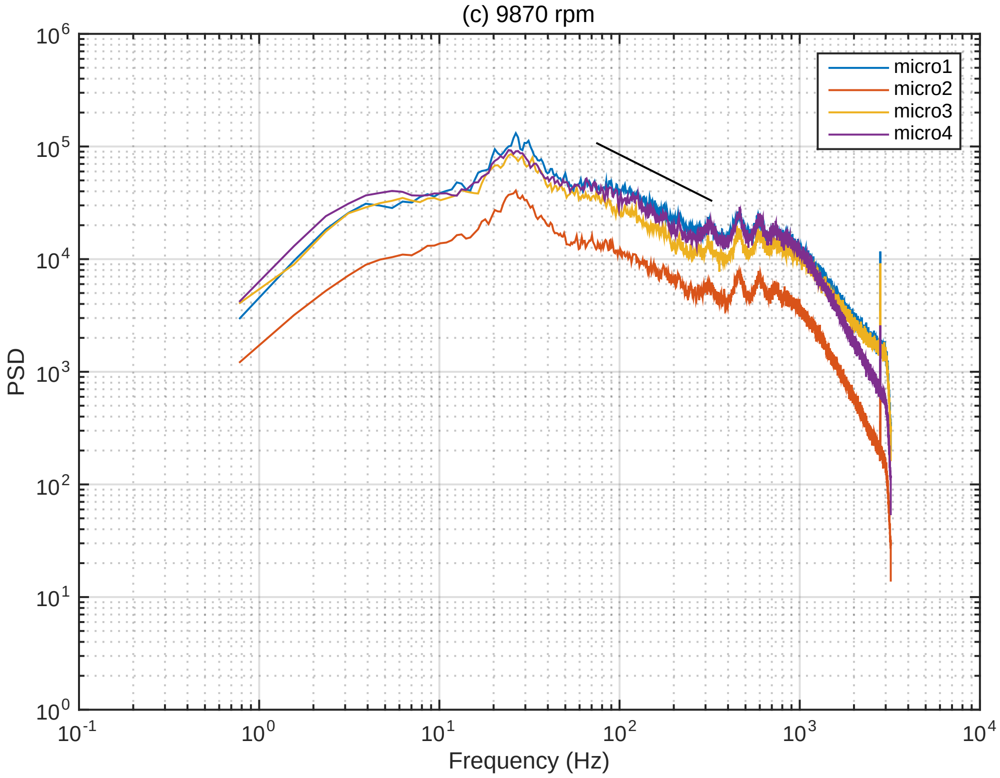

Fig. 4.13 Frequency spectra corresponding to figure 4.9c.

In the stable regime, we observed acoustic duct modes with frequencies close to the expected ones (an integral number of wavelengths along the duct between the compressor and plenum). The damping factor of the modes decreases as the stability threshold is approached, in keeping with the discussion of section 2.3. In consequence, the acoustic intensity increases as the machine is throttled.

Acoustic modes are also observed in the unstable regime, prior to stall inception. Once stall occurs, it persists indefinitely and the acoustic modes disappear. The time at which stall arises is apparently random, which is what one might expect for subcritical instability of a flow subject to random perturbations. As the flow is further throttled, stall onset becomes more probable and the average time taken for stall to appear decreases, until it arises immediately. Stall induces much larger pressure fluctuations than prior to its appearance, which is also symptomatic of a subcritical instability.

Figure 4.8 shows stall onset and development. Acoustic oscillations of growing amplitude are present prior to stall onset and one might speculate on acoustic modes as a subcritical trigger for stall. At onset (figure 4.8b), a rotating cell of growing amplitude can be identified, but rapidly breaks down into apparently random, high-frequency oscillations. They grow and

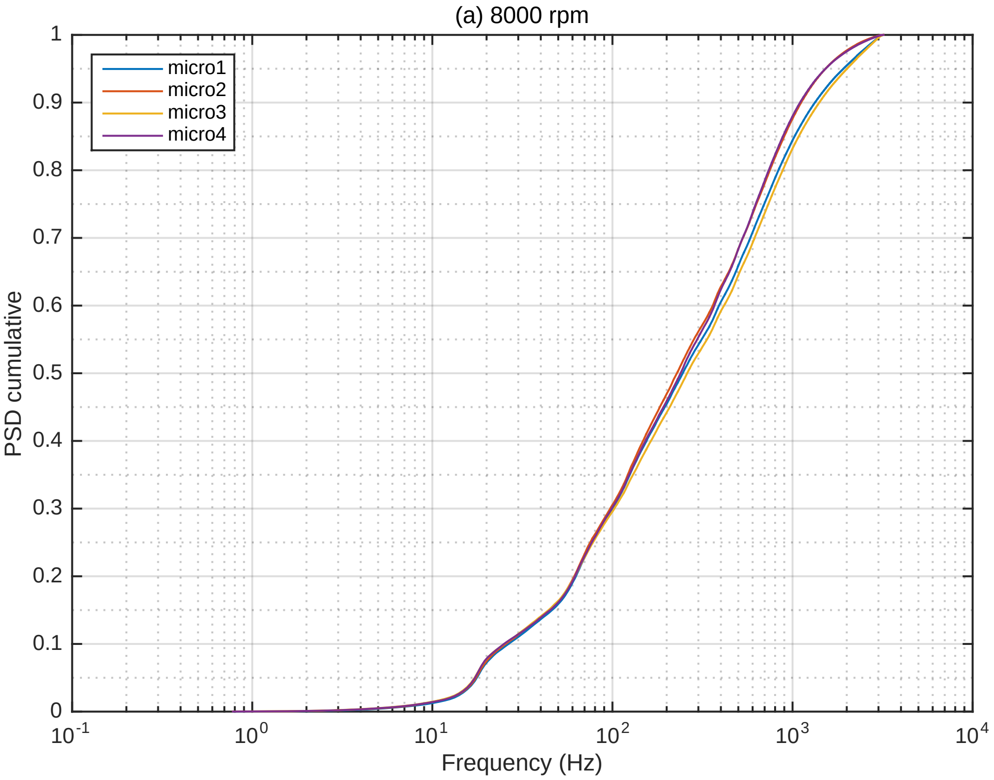

Fig. 4.14 Cumulative spectrum of developed stall corresponding to figure 4.9a.

then decay in intensity until approaching a roughly constant amplitude. Random pressure fluctuations continue indefinitely. These oscillations are of much higher frequency than the acoustic ones that precede stall. Note that such random stall represents a much more complex flow than classical rotating stall in which one or more stall cells rotate around the machine, creating time-periodic fluctuations.

Section 4.4 gave results on developed stall. The frequency spectra are broadband, with a peak at ∼20 Hz followed by a tail extending up to much higher frequencies. The tail appears to follows a power law with an exponent of about -0.9, before dropping off more rapidly above about 1 kHz. Most of the energy lies below 1 kHz.

In section 4.4.2, auto- and cross-correlation functions were used to investigate the pressure fluctuations seen by different microphones. The correlation functions have oscillations corresponding to the ∼20 Hz spectral peak. They decay to zero at large time separations, indicating that pressure fluctuations at sufficiently large temporal separations are uncorrelated. We also found that adjacent microphones are more correlated than microphones which are placed opposite each other.

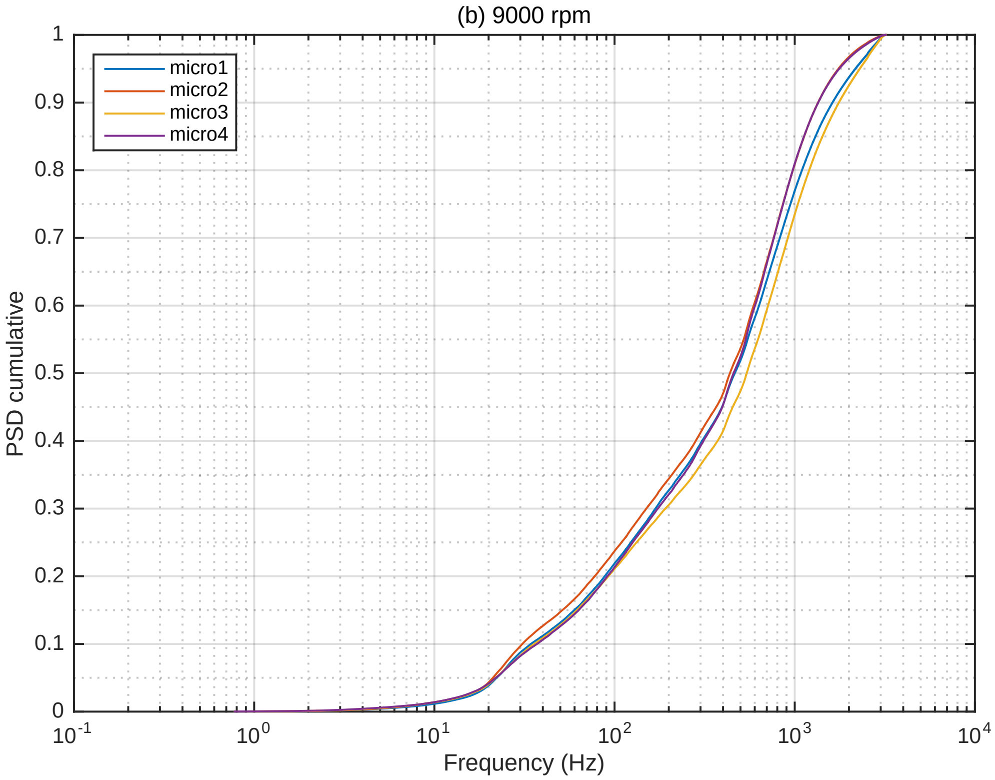

Fig. 4.15 Cumulative spectrum of developed stall corresponding to figure 4.9b.

Finally, we applied low-pass filtering to extract the part of the signal responsible for the ∼20 Hz oscillations. The resulting cross-correlation functions are consistent with a rotating cell which does a single rotation every 0.05 s. This would also explain the ∼20 Hz spectral peak and the oscillations of the correlation functions. However, the decay of the cross-correlation functions at large time differences implies that the cell is not just a simple rotating flow structure, like classical rotating stall, but undergoes random fluctuations as it rotates.

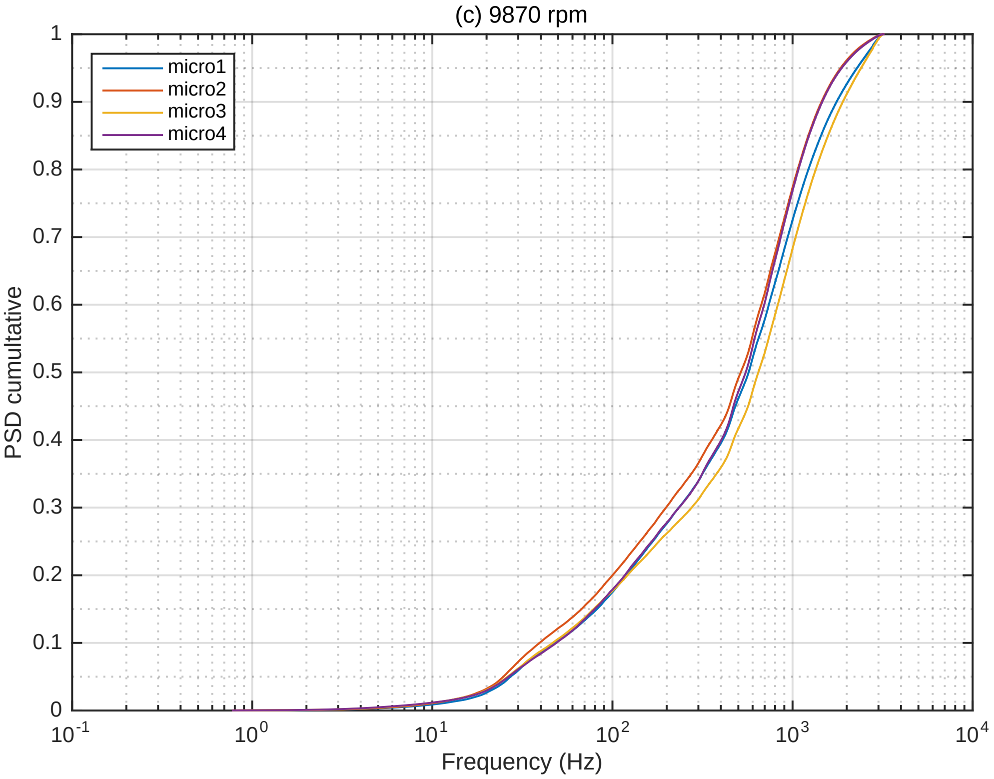

Fig. 4.16 Cumulative spectrum of developed stall corresponding to figure 4.9c.

(a) Auto-correlation of each microphone

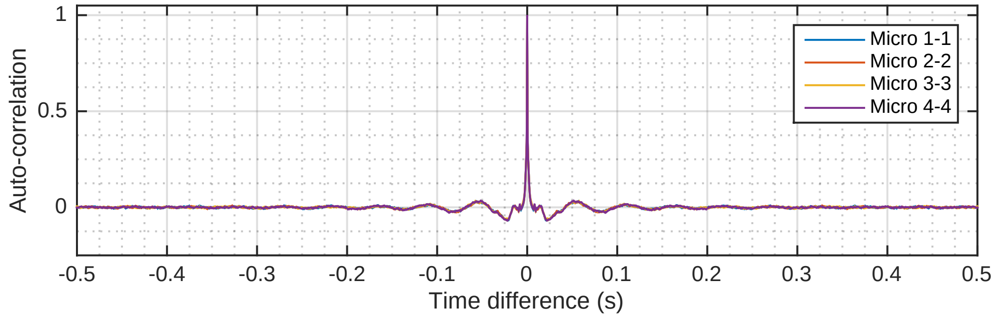

(b) Cross-correlation between adjoining microphones

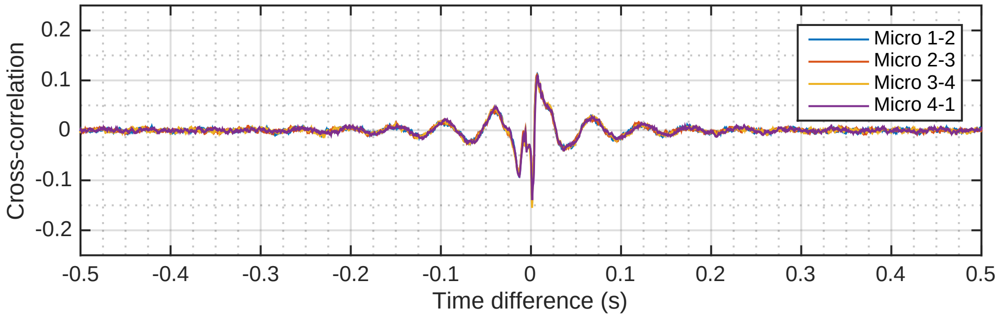

(c) Cross-correlation between oppositely located microphones

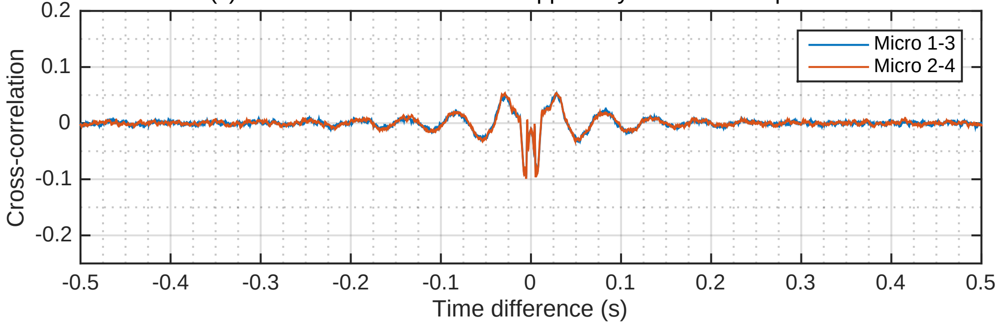

Fig. 4.17 Auto-correlation and cross-correlations at 8000 rpm (throttle setting 97 mm).

(a) Auto-correlation of each microphone

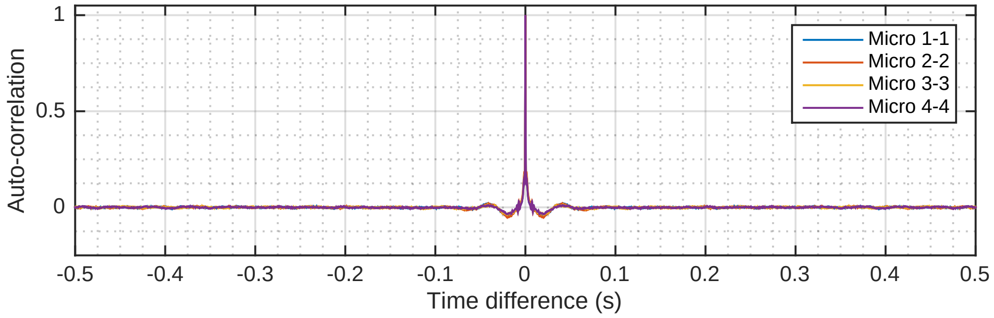

(b) Cross-correlation between adjoining microphones

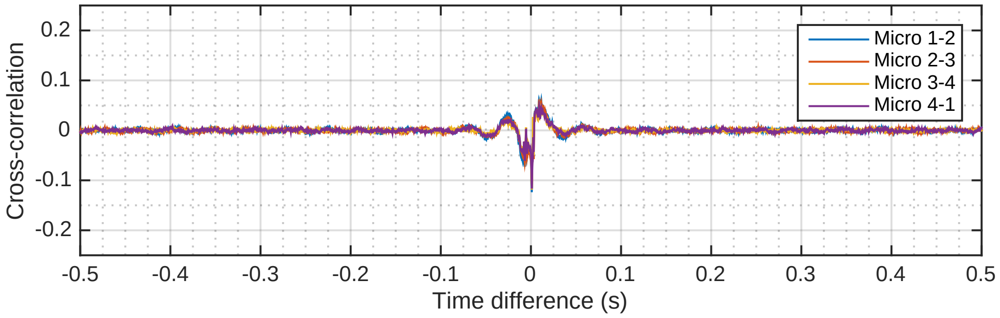

(c) Cross-correlation between oppositely located microphones

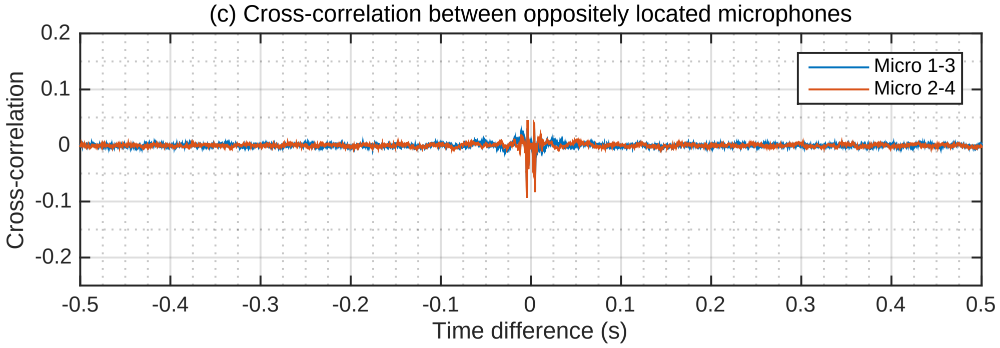

Fig. 4.18 Auto-correlation and cross-correlations at 9000 rpm (throttle setting 98 mm).

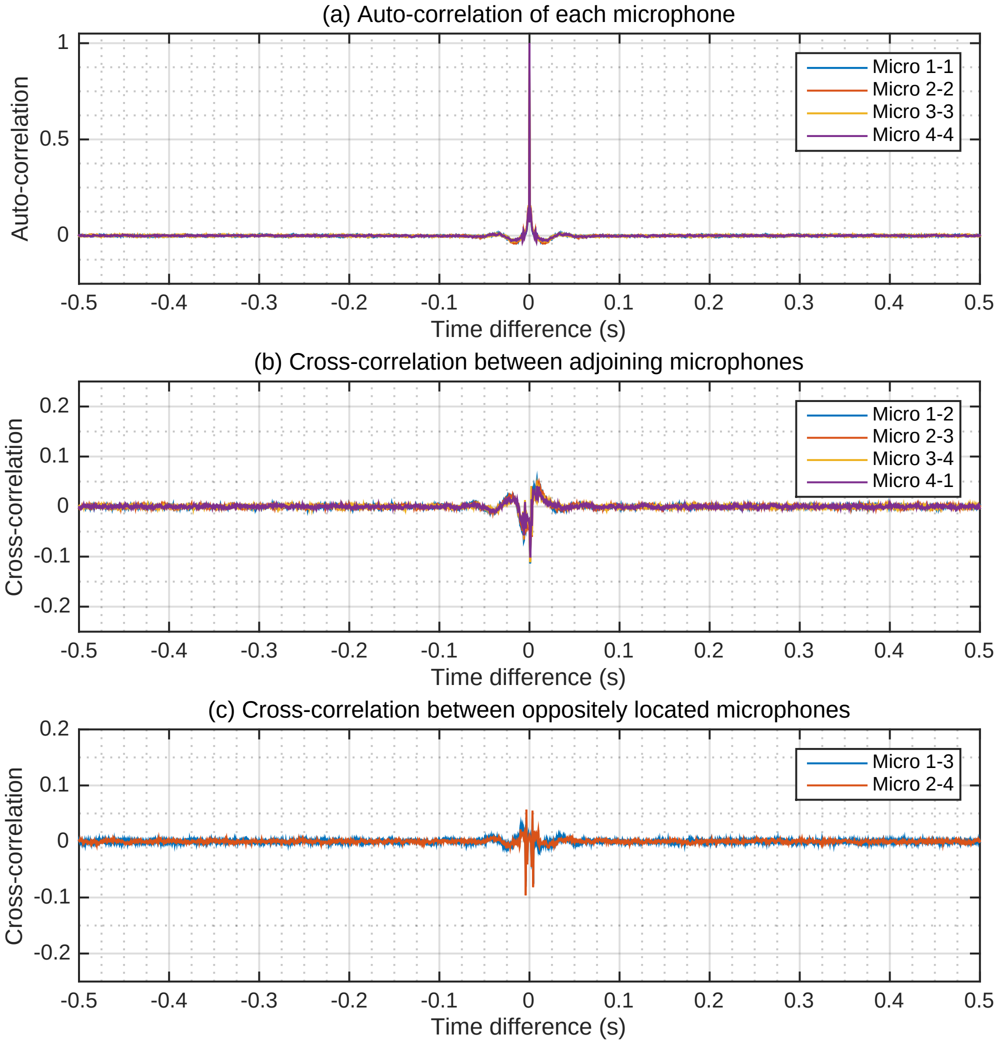

Fig. 4.19 Auto-correlation and cross-correlations at 9870 rpm (throttle setting 99 mm).

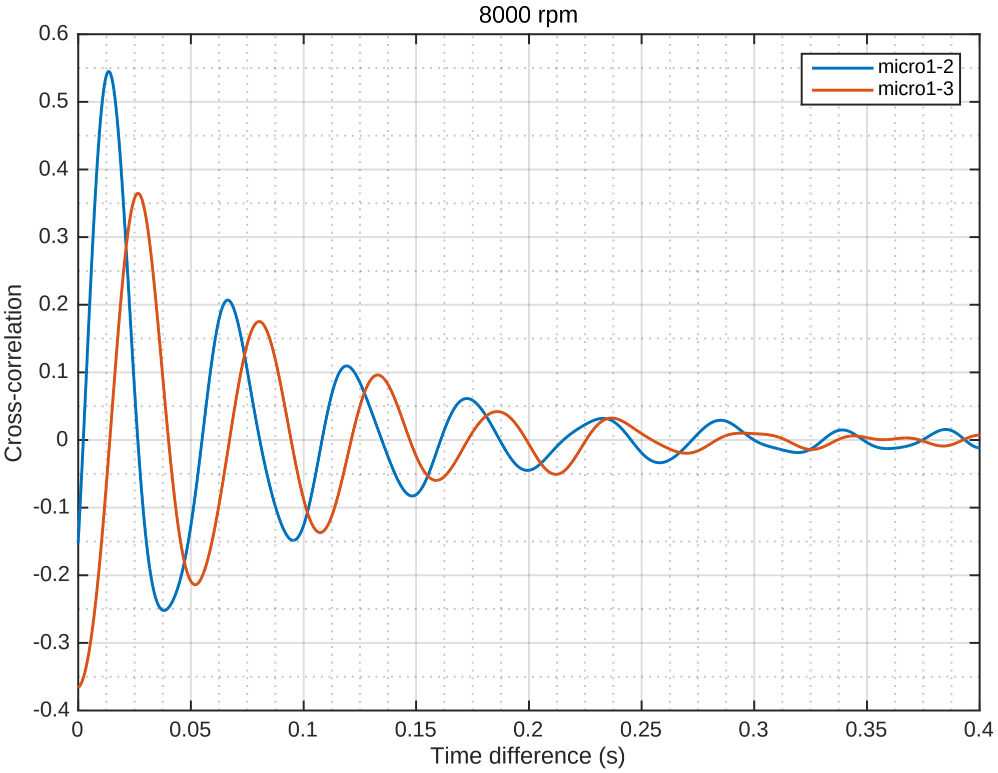

Fig. 4.20 Cross-correlations of the filtered signals (8000 rpm, throttle setting 97 mm).

Chapter 5

Conclusion

Chapter 2 presented the analytical part of the work. The Moore-Greitzer model was described and its consequences for compression system instabilities, both surge and rotating stall, analysed and discussed. The model describes a compression system consisting of an inlet duct, a compressor, an outlet duct, a plenum and a throttle. The compressor is modelled as an actuator disk using equation (2.2) for the difference across the compressor between downstream static pressure and upstream total pressure. In (2.2), u is the axial velocity at the compressor, $\Psi_c(u)$ is the compressor characteristic function and a is a parameter representing inertia. Another characteristic function, $\Phi_T(\Psi)$, appears in the throttle model, where Φ_T is the flow rate at the throttle exit and Ψ is the difference between the plenum and atmospheric pressures. Finally, models of the ducts and plenum introduce additional parameters l_c and B. Large values of B are often associated with surge, whereas small values tend to favour rotating stall.

Figure 2.2 shows the compressor and throttle characteristics in the Φ-Ψ plane, where Φ is the flow rate through the compressor. The intersection of the curves represents a steady, axisymmetric solution, Φ_0, Ψ_0. This is the basic flow whose stability is the subject of this study. The intersection point depends on the throttle setting, moving towards lower Φ_0 as the system is throttled. Thus, the throttle setting can be represented by Φ_0. If the basic flow is stable, it will be realised at large times. On the other hand, instability means that small perturbations to this flow grow and a different flow is realised. One can nonetheless use Φ_0 to represent the throttle setting.

Linearisation of the model about the basic flow was used in section 2.1.2 to study its stability in the presence of infinitesimal perturbations. Normal modes consist of a single Fourier component, $e^{in\theta}$, where θ is the azimuthal angle. The conclusion was that the flow is unstable over the rising part of the compressor characteristic and stable elsewhere. Thus, the maximum of $\Psi_c(\Phi_0)$ is the instability threshold according to the linearised model. As the system is throttled, linear theory predicts instability once the threshold is crossed. The threshold is controlled by non-axisymmetric modes ($n \neq 0$), rather than the symmetric one ($n = 0$), for whose instability is predicted to require lower values of Φ_0. This might suggest that rotating stall is favoured over surge near the threshold. However, this suggestion should be taken with a pinch of salt because linear theory supposes infinitesimal perturbations and thus is incapable of determining the final outcome of instability. Also, the upper bound in Φ_0 for linear instability of the axisymmetric mode approaches the threshold at large B. Thus, it becomes less clear which type of mode will be selected, even for infinitesimal perturbations.

The problem with linear theory is that the growth of the perturbation when instability occurs takes it outside the range of infinitesimal perturbations supposed by the theory. Weakly nonlinear analysis, which assumes small, but finite, perturbations and Φ_0 close to the threshold, was described in section 2.1.3. Instability can take one of two forms: supercritical or subcritical. In the supercritical case, instability does not occur in the linearly stable regime. The basic flow is replaced by a new, non-axisymmetric and unsteady one as the threshold is crossed. The basic flow applies for Φ_0 above the maximum of $\Psi_c(\Phi_0)$ and the new flow appears below this value of Φ_0. The transition between the two flows is continuous: the difference between them is zero at the threshold and increases as Φ_0 is reduced. Subcritical instability is quite different. Instability occurs in the range of linear stability provided the perturbation exceeds a certain amplitude. This amplitude decreases as the threshold is approached, making it harder and harder to maintain stability. Once instability occurs, the theory predicts that the perturbation amplitude goes to infinity in a finite time. Of course, in reality, the perturbation remains finite: the flow leaves the regime of small perturbations supposed by the theory, which means that it no longer applies and is incapable of predicting the new flow resulting from instability. However, it is clear that the result of subcritical instability is a flow quite different from the basic one. There is thus a jump in flow properties when instability arises. This jump, and the occurrence of instability in the linearly stable regime, is symptomatic of subcritical instability. The nature, supercritical or subcritical, of the instability is dependent on a parameter, β, given by equation (2.76). The instability is supercritical if $\beta < -2$ and subcritical when $\beta > -2$.

Some results of numerical integration of the equations of the Moore-Greitzer model were given in section 2.2. The compressor characteristic function was determined by a cubic fit to experimental results for our test rig in the stable range. The throttle characteristic function was chosen to have the usual form, (2.11). Rather than truncating the model to just a single non-axisymmetric Fourier component, as do many authors, including Moore and Greitzer [28], the full model was used. For numerical purposes, it is nonetheless necessary to truncate the model to a finite number of components and to discretise time. We varied the number of components and time step to study convergence and chose values which gave satisfactory accuracy.

If the initial flow is axisymmetric it remains so according to the model. Thus, axisymmetric initialisation disallows rotating stall. Initialising using a small axisymmetric perturbation of the basic flow and varying Φ_0 and B, we found that surge occurred throughout the range of axisymmetric instability predicted by linear theory, but not outside that range. This suggests that axisymmetric instability is supercritical.

Non-axisymmetric initialisation can lead to rotating stall. This can occur within the range of axisymmetric instability. Thus, the outcome, surge or rotating stall, can depend on the type of perturbation to which the flow is subjected. Using a small non-axisymmetric initial perturbation and integrating the equations to large times, we found that non-axisymmetric instability has all the characteristics of the subcritical case: it can appear in the linearly stable range and produces a jump in the developed flow from the steady, axisymmetric one to an unsteady, non-axisymmetric rotating stall. This is in accord with $\beta > -2$ for the compressor and throttle characteristic functions used.

The final section of chapter 2 presented a simple model of the observed acoustic duct modes. This model predicts modal frequencies close to the values obtained by requiring an integral number of half-wavelengths along the duct. It also predicts that the modal damping factor is affected by the compressor and should decrease as the instability threshold is approached.

Chapter 3 described the experimental test rig, while chapter 4 gave results. Surge was never observed, while random stall was found to occur when the system was sufficiently throttled. This is apparent from the compressor characteristics (figure 4.1), which show a decrease in flow rate and pressure rise across the compressor when stall occurs. Stall occurs before the maximum of the static-total compressor characteristic is reached. The maximum is the linear stability threshold according to the Moore-Greitzer model. This, together with the discontinuous decrease in flow rate and pressure rise, suggests that the instability is subcritical, in accord with the results of chapter 2.

In the stable regime, we observed acoustic duct modes having frequencies close to the expected ones. The damping factor of the modes decreases as the stability threshold is approached, in keeping with the discussion of section 2.3. In consequence, the acoustic intensity increases as the machine is throttled.

Acoustic modes are also observed in the unstable regime, prior to stall inception. Once stall occurs, it persists indefinitely and the acoustic modes disappear. The time at which stall arises is apparently random, which is what one might expect for subcritical instability of a flow subject to random perturbations. As the flow is further throttled, stall onset becomes more probable and the average time taken for stall to appear decreases, until it arises immediately. Stall induces much larger pressure fluctuations than prior to its appearance, which is also symptomatic of a subcritical instability.

Figure 4.8 shows stall onset and development. Acoustic oscillations of growing amplitude are present just prior to stall onset and one might speculate on acoustic modes as a subcritical trigger for stall. At onset (figure 4.8c), a rotating cell of growing amplitude can be identified, but rapidly breaks down into apparently random, high-frequency oscillations. They grow and then decay in intensity until approaching a roughly constant amplitude. Random pressure fluctuations continue indefinitely. These oscillations are of much higher frequency than the acoustic ones that precede stall. Note that such random stall represents a much more complex flow than classical rotating stall in which one or more stall cells rotate around the machine, creating time-periodic fluctuations.

Section 4.4 gives results for developed stall. The frequency spectra are broadband, with a peak at $\sim$20 Hz followed by a tail extending up to much higher frequencies. The tail appears to follows a power law with an exponent of about -0.9, before dropping off more rapidly above about 1 kHz. Most of the energy lies below 1 kHz.

We applied low-pass filtering to extract the part of the signal responsible for the $\sim$20 Hz spectral peak. The resulting cross-correlation functions are consistent with a rotating cell which does a single rotation every 0.05 s. This would also explain the $\sim$20 Hz spectral peak and the oscillations of the correlation functions. However, the decay of the cross-correlation functions at large time differences implies that the cell is not just a simple rotating flow structure, like classical rotating stall, but undergoes random fluctuations as it rotates.

Finally, despite the current limitations (discussed in the introduction) of detailed numerical simulations of flow in compression systems, it would be interesting to carry out such simulations of the present system. This might allow identification of the mechanisms leading to random stall and a deeper understanding of the spectra and correlation functions of developed stall.

References

[1] Camp, T. R. and Day, I. J. (1997). A study of spike and modal stall phenomena in a low-speed axial compressor. In *International Gas Turbine and Aeroengine Congress and Exhibition*. The American Society of Mechanical Engineers.

[2] Chen, Y. N., Haupt, U., and Rautenberg, M. (1991). Discussion: “rotating waves as a stall inception indication in axial compressors”. *Journal of Turbomachinery*, 113(2):301–302.

[3] Choi, M., Baek, J. H., Oh, S., and Ki, D. (2008). Role of hub-corner-separation on rotating stall in an axial compressor. *Transactions of the Japan Society for Aeronautical and Space Sciences*, 51(172):93–100.

[4] Crevel, F., Gourdain, N., and Moreau, S. (2014a). Numerical simulation of aerodynamic instabilities in a multistage high-speed high-pressure compressor on its test-rig—part i: Rotating stall. *Journal of Turbomachinery*, 136(10):101003.

[5] Crevel, F., Gourdain, N., and Ottavy, X. (2014b). Numerical simulation of aerodynamic instabilities in a multistage high-speed high-pressure compressor on its test rig—part ii: Deep surge. *Journal of Turbomachinery*, 136(10):101004.

[6] D’Andrea, R., Behnken, R. L., and Murray, R. M. (1997). Rotating stall control of an axial flow compressor using pulsed air injection. *Journal of Turbomachinery*, 119(4):742–752.

[7] Day, I. J. (1993). Stall inception in axial flow compressors. *Journal of Turbomachinery*, 115(1):1–9.

[8] Day, I. J. (2016). Stall, surge, and 75 years of research. *Journal of Turbomachinery*, 138(1):011001.

[9] Drazin, P. and Reid, W. (1981). *Hydrodynamic stability*. Cambridge University Press.

[10] Feulner, M., Hendricks, G., and Paduano, J. (1996). Modeling for control of rotating stall in high-speed multistage axialcompressors. *Journal of Turbomachinery*, 118(1-10).

[11] Freeman, C., Wilson, A. G., Day, I. J., and Swinbanks, M. A. (1998). Experiments in active control of stall on an aeroengine gas turbine. *Journal of Turbomachinery*, 120(4):637–647.

[12] Gao, F., Ma, W., Zambonini, G., Boudet, J., Ottavy, X., Lu, L., and Shao, L. (2015). Large-eddy simulation of 3-d corner separation in a linear compressor cascade. *Physics of Fluids (1994-present)*, 27(8):085105.

[13] Garnier, V. H., Epstein, A. H., and Greitzer, E. M. (1991). Rotating waves as a stall inception indication in axial compressors. *Journal of Turbomachinery*, 113(2):290–301.

[14] Gbadebo, S., Cumpsty, N. A., and Hynes, T. (2005). Three-dimensional separations in axial compressors. *Journal of Turbomachinery*, 127(2):331–339.

[15] Gong, Y., Tan, C., Gordon, K., and Greitzer, E. (1999). A computational model for short wave-length stall inception and development in multistage compressors. In *ASME 1998 International Gas Turbine and Aeroengine Congress and Exhibition*, pages V001T01A114–V001T01A114. American Society of Mechanical Engineers.

[16] Gravdahl, J. T. and Egeland, O. (2012). *Compressor Surge and Rotating Stall: Modeling and Control*. Springer Science and Business Media.

[17] Greitzer, E. M. (1976). Surge and rotating stall in axial flow compressors—part i: Theoretical compression system model. *Journal of Engineering for Power*, 98(2):190–198.

[18] Gysling, D. and Greitzer, E. (1994). Dynamic control of rotating stall in axial flow conpressors using aeromechanical feedback. In *ASME 1994 International Gas Turbine and Aeroengine Congress and Exposition*, pages V001T01A100–V001T01A100. American Society of Mechanical Engineers.

[19] Haynes, J., Henderick, G., and Epstein, A. (1994). Active stabilization of rotating stall in a three stage axial compressor. *Journal of Turbomachinery*, 116(2):226–239.

[20] He, L. (1997). Computational study of rotating-stall inception in axial compressors. *Journal of Propulsion and Power*, 13(1):31–38.

[21] Hendricks, G., Sabnis, J., and Feulner, M. (1996). Analysis of instability inception in high-speed multi-stage axial-flow compressors. In *ASME 1996 International Gas Turbine and Aeroengine Congress and Exhibition*, pages V001T01A092–V001T01A092. American Society of Mechanical Engineers.

[22] Hoying, D., Tan, C., Vo, H., and Greitzer, E. (1999). Role of blade passage flow structures in axial compressor rotating stall inception. In *ASME 1998 International Gas Turbine and Aeroengine Congress and Exhibition*, pages V001T01A138–V001T01A138.

[23] Inoue, M., Kuroumaru, M., Tanino, T., Yoshida, S., and Furukawa, M. (2001). Comparative studies on short and long length-scale stall cell propagating in an axial compressor rotor. *Journal of Turbomachinery*, 123(1):24–30.

[24] ISO (2003). *5167-4 2003 Mesure de débit des fluides au moyen d'appareils déprimogènes insérés dans des conduites en charge de section circulaire - Partie 4: Tubes de Venturi*.

[25] Ju, P. and Ning, F. (2014). Numerical investigation of the prestall inception behaviour in a transonic axial fan. *ASME*.

[26] Landau, L. D. (1944). On the problem of turbulence. *Dokl. Akad. Nauk SSSR*, 44(8):339–349.

[27] Moore, F. K. (1983). A theory of rotating stall of multistage axial compressors. Technical report, NASA, http://ntrs.nasa.gov/archive/nasa/casi.ntrs.nasa.gov/19830020904.pdf.

[28] Moore, F. K. and Greitzer, E. M. (1986). A theory of post-stall transients in axial compression systems: Part i - development of equations. *Journal of Engineering for Gas Turbines and Power*, 108(1):68–76.

[29] Paduano, J., Epstein, A., Valavani, L., Longley, J., Greitzer, E., and Guenette, G. (1991). Active control of rotating stall in a low speed axial compressor. In *ASME 1991 International Gas Turbine and Aeroengine Congress and Exposition*, pages V001T01A036–V001T01A036. American Society of Mechanical Engineers.

[30] Paduano, J., Valavani, L., Epstein, A., Greitzer, E., and Guenette, G. (1994). Modeling for control of rotating stall. *Automatica*, 30(9):1357–1373.

[31] Paduano, J. D., Greitzer, E. M., and Epstein, A. H. (2001). Compression system stability and active control. *Fluid Mechanics*, 33:491–517.

[32] Pullan, G., Young, A., Day, I., Greitzer, E., and Spakovszky, Z. (2015). Origins and structure of spike-type rotating stall. *Journal of Turbomachinery*, 137(5):051007.

[33] Saxer-Felici, H., Saxer, A., Inderbitzin, A., and Gyarmathy, G. (1998). Prediction and measurement of rotating stall cells in an axial compressor. In *ASME 1998 International Gas Turbine and Aeroengine Congress and Exhibition*. American Society of Mechanical Engineers.

[34] Schalkwyk, C., Paduano, J., Greitzer, E., and Epstein, A. (1998). Active stabilization of axial compressors with circumferential inlet distortion. *Journal of Turbomachinery*, 120(3):431–439.

[35] Schmid, P. and Henningson, D. (2012). *Stability and transition in shear flows*, volume 142. Springer Science and Business Media.

[36] Stoica, P. and Moses, R. (2005). *Spectral Analysis of Signals*, volume 452. Pearson Prentice Hall Upper Saddle River, NJ.

[37] Stuart, J. (1960). On the non-linear mechanics of wave disturbances in stable and unstable parallel flows part 1. the basic behaviour in plane poiseuille flow. *Journal of Fluid Mechanics*, 9(03):353–370.

[38] Sun, X. (1996). Three-dimensional compressible flow stability theory of rotating stall. Technical Report BH-B4765, Beihang University.

[39] Tse, N. and Lai, L. (2007). Wavelet-based algorithm for signal analysis. *EURASIP Journal on Applied Signal Processing*, 2007(1):169–169.

[40] Vo, H. (2001). *Role of Tip Clearance Flow on Axial Compressor Stability*. PhD thesis, Massachusetts Institute of Technology.

[41] Vo, H., Tan, C., and Greitzer, E. (2008). Criteria for spike initiated rotating stall. *Journal of Turbomachinery*, 130(1):011023.

[42] Wang, H.-H., Yeung, S., and Krstic, M. (2000). Experimental application of extremum seeking on an axial-flow compressor. *IEEE Transactions on Control Systems Technology*, 8(2):300–309.

[43] Yamada, K., Kikuta, H., Iwakiri, K., Furukawa, M., and Gunjishima, S. (2013). An explanation for flow features of spike-type stall inception in an axial flow compressor rotor. *Journal of Turbomachinery*, 135(2):021023.

[44] Zhang, L., Scott, J., and Boum, G. N. (2015). Méthode de paramétrage du modèle moore-greitzer à partir d'un cycle de pompage fourni. In *S16 Aérodynamique des turbomachines*. AFM, Association Française de Mécanique.